University of Stuttgart
Institute of Nuclear Technology
and Energy Systems

Advanced modelling of the high-temperature oxidation of zirconium in steam exploiting self-consistent thermodynamic data

Corbinian Nigbur

November 2020 IKE 2-163

University of Stuttgart
Institute of Nuclear Technology
and Energy Systems

Advanced modelling of the high-temperature oxidation of zirconium in steam exploiting self-consistent thermodynamic data

von der Fakultät Energie-, Verfahrens- und
Biotechnik der Universität Stuttgart zur Erlangung
der Würde eines Doktor-Ingenieurs (Dr.-Ing.)
genehmigte Abhandlung

vorgelegt von

Corbinian Nigbur
geboren in Würselen

Hauptberichter: Prof. Dr.-Ing. Jörg Starflinger
Mitberichter: apl. Prof. Dr.-Ing. Michael Seidenfuß

Tag der Einreichung: 14.07.2020
Tag der mündlichen Prüfung: 30.11.2020

ISSN-0173-6892

November 2020 IKE 2-163

IKE

Eigenständigkeitserklärung

Ich versichere hiermit, dass ich die vorliegende Arbeit mit dem Titel

„Advanced modelling of the high-temperature oxidation of zirconium in steam exploiting self-consistent thermodynamic data”

selbständig und ohne unzulässige fremde Hilfe erbracht habe und keine anderen als die angegebenen Hilfsmittel und Quellen benutzt habe. Fremde Quellen und Gedanken, welche ich übernommen habe, sind als solche kenntlich gemacht. Die Arbeit hat in gleicher oder ähnlicher Form noch keinem Prüfungsausschuss vorgelegen.

C. Nigbur

Albbruck, den 30.06.2020 Corbinian Nigbur

Acknowledgment

At this point, I would like to thank all the people who supported me in writing this thesis.

First and foremost, I would like to thank my doctoral supervisor, Prof. Dr.-Ing. Jörg Starflinger, who welcomed me to his institute and gave me the opportunity to write this thesis. I thank him for his motivation and many hours of professional support throughout the years. Furthermore, I would like to thank him for his extraordinary efforts to support me in the best possible way beyond my thesis; in particular, for investing so much effort in my professional training at the Siemens training reactor.

I would also like to thank my co-examiner apl. Prof. Dr.-Ing. Michael Seidenfuß, whose great interest in the subject of my thesis contributed significantly to its success. My thanks also go to Prof. Dr. rer. nat. Dr. h. c. Siegfried Schmauder, who chaired the examination. I would like to thank both of them for their commitment and friendly manner.

Moreover, I would like to thank Dr.-Ing. Michael Buck for his professional support and many valuable pieces of advice. My work has benefited substantially from his profound expertise, his ideas, and especially his constructive criticism. Hence, I would like to thank him for the many evenings of professional discussion.

Further thanks are owed to the Institut de Radioprotection et de Sûreté Nucléaire (IRSN) for the kind provision of the software Nucleatoolbox, the NUCLEA database, and the valuable support. In this context, I would like to thank Marc Barrachin and Bruno Piar, whose selfless aid with their outstanding expertise was of inestimable value.

A very special thank you goes to all the staff of the Institute of Nuclear Technology and Energy Systems and my fellow doctoral students. This work would not have been possible without their help, so I would like to thank them all very much.

Albbruck, January 2021 Corbinian Nigbur

Contents

Abstract iii

Kurzfassung v

List of Figures vii

List of Tables xi

Nomenclature xiii

1. Motivation 1

1.1. High-temperature zirconium oxidation 1
1.2. Loss-of-coolant accidents 1
1.3. Severe accident analysis codes 3
1.4. Outline of the present work 5

2. Phenomena of zirconium oxidation 7

2.1. Zr-O material system 7
2.2. Mass transport 11
2.3. Heat effects and heat transport 14

3. State of the art 17

3.1. Parabolic rate equations 17
3.2. Integral diffusion models 23
3.3. Experimental data basis 31
3.4. Aim of the work 34

4. Thermodynamic lookup table 37

4.1. CALPHAD method, NUCLEA database, and NucleaToolbox 38
4.2. Development of the lookup table 41

5. Material and transport properties library 51

5.1. Parabolic rate constants 51
5.2. Oxygen diffusion coefficients 54
5.3. Thermal conductivities 58

5.4. Densities 59

6. Advanced integral model **61**
6.1. Heat transport 61
6.2. System of equations 65
6.3. Coupling to the lookup table 67

7. Spatially discretized model **73**
7.1. Mass transport 74
7.2. Heat transport 77
7.3. System of equations 78
7.4. Coupling to the lookup table 79

8. Verification **81**
8.1. Analytical solutions for two-phase Stefan problems 81
8.2. Mass transport models 84
8.3. Heat transport models 85
8.4. Cell number dependency 88

9. Model comparisons **91**
9.1. Comparison to models from the literature 91
9.2. Comparison to models implemented into ATHLET-CD 98
9.2.1. Case 1: Oxidation 102
9.2.2. Case 2: Steam starvation 104

10. Model tests including thermally-induced phase changes **109**
10.1. Positive temporal temperature transients 112
10.2. Negative temporal temperature transients 118
10.3. Assessment of results 124

11. Summary and outlook **127**

Bibliography **133**

Appendices **139**
A. Oxidation model based on parabolic rate equations 139
B. Modeling heat effects without thermodynamic computer codes 141
C. Elaborate concentration profiles for integral models 145
D. Programming flowcharts 149
E. Supplementary figures 155

Abstract

In a loss-of-coolant accident, deteriorated cooling conditions facilitate the high-temperature oxidation of zirconium in steam. This exothermic reaction entails the acceleration of core degradation and causes the generation of hydrogen. Due to the significance of oxidation reaction modeling for accident progression, it is an essential part of severe accident simulation codes. However, due to high computation cost, integral codes commonly rely on simple parabolic rate laws as their oxidation models. These models are subject to assumptions such as isothermal conditions, semi-infinite media, and unlimited steam supply, which are infrequently met under accident conditions. Integral models, as considered here, relax these restrictive assumptions and have the potential to provide significant improvement, and they share the advantage of being relatively computationally inexpensive. Nonetheless, a satisfactory solution is yet to be found for their extension to cover zirconium oxidation with its various phase transitions and accompanying heat effects.

The obstacles inhibiting further advances in oxidation reaction modeling using the integral approach are twofold. The first challenge arises from the high complexity of a thermodynamic system that can undergo phase transitions due to changes in both composition and temperature and that is complicated by chemical reactions, which cause a variety of heat effects. Therefore, a suitable numerical model must be both physically precise regarding the heat and mass transport mechanisms and must incorporate detailed thermodynamic data. The second challenge consists in the lack of experimental data providing insight into the oxidation reaction, especially under transient conditions, which, however, is much needed for the validation of new modeling approaches.

In this light, this thesis presents the development of a fast-running advanced integral model and its novel coupling to a lookup table that comprises physically self-consistent thermodynamic data. It addresses the challenge of missing experimental data, which is suitable for its validation, using model tests in comparison to a spatially discretized model, which has also been developed in this thesis for this very purpose. Furthermore, this work draws comparisons with models proposed in the literature and models that are implemented in severe accident analysis codes today. It demonstrates the capabilities of the advanced

integral model to describe complex heat effects and phase changes, which surpass the abilities of state-of-the-art modeling approaches.

In terms of structure, this thesis can be divided into three parts. The first part is dedicated to a detailed physical description of the oxidation reaction and an investigation of the state of the art regarding its mathematical modeling in today's severe accident analysis codes. On that basis, limitations of existing modeling approaches are identified and requirements are defined that an advanced model must satisfy. In the second part, a description is given of the development of the thermodynamic lookup table, a material and transport property library, the advanced integral model, and the spatially discretized model. Following this, the third part presents a series of model tests, starting with verification measures, continuing with comparisons to models from the literature and the model used in ATHLET-CD, and finally addressing a test case, whose complexity regarding the occurring phase changes exceeds the range of applicability of today's modeling approaches.

The result of this systematic development is an advanced integral model that captures both chemically- and thermally-induced phase transitions, and which describes heat sinks and sources with precise thermodynamic data. Hence, it overcomes the limitations of the commonly used parabolic rate approaches and surpasses the capabilities of existing integral models. Thus, in a single model, it achieves the urgently required capability of following the oxidation reaction through different phases of core degradation, starting from the classic oxidation of cladding tube surfaces, through the phases of steam starvation, over the melting and chemical dissolution processes, and ending with the solidification and oxidation of crusts. Consequently, the advanced integral model's improved prediction of heat and hydrogen generation has the potential to reduce the uncertainty associated with today's severe accident analysis codes.

Kurzfassung

Bei Kühlmittelverluststörfällen begünstigen verschlechterte Wärmeabfuhrbedingungen die Hochtemperaturoxidation von Zirkonium in Dampf. Die Wärmefreisetzung dieser exothermen Reaktion beschleunigt die Kernzerstörung und ist Ursache für die Bildung explosiven Wasserstoffs. Wegen ihrer essentiellen Bedeutung für den Störfallverlauf ist die Modellierung dieser Reaktion ein wichtiger Bestandteil heutiger Störfallanalysecodes. Aufgrund strenger Anforderungen an die Rechenzeit dieser Computerprogramme wird die Oxidationsreaktion in der Regel mit Hilfe einfacher parabolischer Ratenansätze abgebildet. Die Annahmen dieser Modelle, wie isotherme Bedingungen, halbunendliche Medien oder eine unbegrenzte Dampfzufuhr, werden jedoch unter realen Störfallbedingungen kaum erfüllt. Integralmodelle kommen ohne diese restriktiven Annahmen aus und sind zwar numerisch anspruchsvoller, jedoch nach wie vor kostengünstig, sodass sie das Potenzial zu einer signifikanten Verbesserung bieten. Trotz intensiver Entwicklungsbemühungen ist es jedoch bislang nicht gelungen, diese Modelle so zu erweitern, dass sie die Oxidationsreaktion im Zirkonum-Sauerstoff-System mit all seinen Phasenwechseln abbilden können.

Die Weiterentwicklung der Integralmodelle wird durch zwei Herausforderungen behindert. Die Erste resultiert aus der Betrachtung eines thermodynamischen Systems, welches aufgrund einer stetigen Veränderungen seiner Zusammensetzung und Temperatur verschiedene Phasen ausbilden kann und gleichzeitig durch Wärmeeffekte chemischer Reaktionen gestört wird. Folglich muss ein geeignetes numerisches Modell nicht nur die Wärme- und Stofftransportmechanismen abbilden können, sondern auch die komplexen thermodynamischen Zusammenhänge erfassen. Die zweite Herausforderung entsteht aus dem Mangel an experimentellen Daten, welche die Oxidationsreaktion unter instationären und insbesondere temperaturtransienten Bedingungen beschreiben, und der eine Validierung neuer Modellansätze erheblich erschwert.

Vor diesem Hintergrund präsentiert diese Abhandlung die Entwicklung eines schnell laufenden, fortschrittlichen Integralmodells und dessen neuartige Kopplung an eine Lookup-Tabelle, welche thermodynamische Zustände physikalisch konsistent beschreibt. Das Problem fehlender experimenteller Daten, welche zu einer Validierung geeignet wären, löst sie durch Vergleiche zu den Lösungen eines räumlich diskretisierten Modells, welches ebenfalls im Rahmen dieser Arbeit entwickelt wurde. Das fortschrittliche Integralmodell wird somit nicht nur den bestehenden Modellen aus der Literatur und aus Störfallanalysecodes gegenübergestellt, sondern auch seine Fähigkeit demonstriert, komplexe Phasenwechsel und Wärmeeffekte zu erfassen, an denen bestehende Modellansätzen scheitern.

Bezüglich ihres Aufbaus lässt sich die Arbeit in drei Teile gliedern. Der erste Teil widmet sich der phänomenologischen Beschreibung der Oxidationsreaktion und einer Reflektion des Standes von Wissenschaft und Technik hinsichtlich der mathematisch-physikalischen Modelle, welche heute in Störfallanalysecodes Verwendung finden. Im zweiten Teil wird die Entwicklung der thermodynamischen Lookup-Tabelle, einer Bibliothek von Material- und Transporteigenschaften, des fortgeschrittlichen Integralmodells und schließlich des räumlich diskretisierten Modells beschrieben. Der dritte Teil stellt sodann eine Reihe von Tests vor, welche mit der Verifikation der Modelle beginnt, über Vergleiche zu Modellen aus der Literatur und aus dem Störfallanalysecode ATHLET-CD reicht und zu einem Testfall führt, dessen Komplexität hinsichtlich der auftretenden Phasenwechsel den Anwendungsbereich heutiger Modellierungsansätze deutlich übersteigt.

Als Ergebnis dieser Arbeit steht ein fortschrittliches Integralmodell zur Verfügung, welches sowohl chemisch als auch thermisch induzierte Phasenwechsel erfassen kann und Wärmequellen und -senken auf Grundlage präziser thermodynamischer Daten beschreibt. Damit überwindet es die Einschränkungen der üblichen Modelle, die auf parabolischen Ratenansätzen basieren, und übertrifft die Fähigkeiten aktueller Integralmodelle. Durch seinen neuartigen Ansatz ist es mit nur einem einzigen Modell möglich, die Oxidationsreaktion durch die verschiedenen Phasen der Kernzerstörung von der klassischen Oxidation von Hüllrohroberflächen, durch Phasen des Dampfmangels, über Schmelz- und chemische Auflösungsprozesse, bis hin zur Erstarrung von Krusten zu verfolgen. Durch Verbesserungen bezüglich der Vorhersage der Wärme- und Wasserstofferzeugung leistet es somit einen nachhaltigen Beitrag dazu, die gegenwärtige Unsicherheit der Codes zur Analyse schwerer Störfälle weiter zu verringern.

List of Figures

1.1. Sketch of a reactor pressure vessel of a pressurized water reactor with sufficient cooling and at the beginning of core uncovery. 2
1.2. Sketch of a reactor pressure vessel in a pressurized water reactor at an advanced stage of core degradation. 3

2.1. Zr-O binary phase diagram 8
2.2. Oxygen concentration distribution during the oxidation of zirconium alloys in steam 10
2.3. Example of heat effects accompanying the oxidation reaction in the Zr-O phase diagram. 15

3.1. Assumption of composed concentration profiles underlying parabolic rate equations. 18
3.2. Determination of phase boundary concentrations using the binary Zr-O phase diagram for an exemplary isothermal system. 20
3.3. Composed oxygen concentration profile of an exemplary integral model. . . 25
3.4. Schematic illustration of a volume Ω confined by two surfaces Γ_+ and Γ_-. . 26
3.5. Schematic illustration of a surface Γ dividing two volumes Ω_I and Ω_{II}. . . . 27

4.1. Illustration of the grid points of the lookup table (Zr-O system). 42
4.2. Zr-O binary phase diagram as reconstructed from data from the thermodynamic lookup table. 43
4.3. Zr-O binary phase diagrams from the literature in direct comparison. 45
4.4. Zr-O binary phase diagram developed in this work compared to the diagram of Abriata et al. [1]. 46
4.5. Lookup table illustrated as x_O-T-h_m-diagram. 47
4.6. x_O-T-h_m-diagram plotted in analogy to the logic of binary phase diagrams. 49

5.1. Correlations for the estimation of the parabolic rate constant k_τ by different authors. 53
5.2. Correlations for the estimation of the parabolic rate constant k_{ox} by different authors. 53
5.3. Correlations for the estimation of diffusion coefficients of oxygen in metallic zirconium by different authors: solid lines α-Zr, dashed line β-Zr. 55

5.4. Correlations for the estimation of diffusion coefficients of oxygen in β-ZrO$_2$ by different authors. 56
5.5. Correlations for the estimation of diffusion coefficients of oxygen in dublex oxide (β-ZrO$_2$ and γ-ZrO$_2$) by different authors. 57

6.1. Leaps in the concentration profile (isothermal system) and enthalpy profile (unary system) at the position of a phase interface. 62
6.2. Effect of two-phase transition zones on concentration, enthalpy, and temperature profiles in an integral model. 63
6.3. Illustration of the composed concentration and enthalpy profiles of an exemplary model system comprising an oxidic and a metallic phase underlying the advanced integral model (arbitrary boundary conditions). . . 66
6.4. Illustration of the concept used for the interpolation of temperature T with the aid of the oxygen molar fraction x_O and molar enthalpy h_m. 69
6.5. Illustration of the concept used to derive molar oxygen fractions of phases in phase equilibrium x_O^*. 70
6.6. Interpretations of changing phase fractions f^j in the advanced integral model. 71

7.1. Sketch of the discretization scheme using a finite volume approach. 74
7.2. Concept of virtual partial oxygen densities in neighboring cells. 77

8.1. Temporal evolution of oxygen concentration profiles and movement of the phase interface (oxide-metal) as calculated with the help of an analytical solution, the advanced integral model and the spatially discretized model. . 86
8.2. Temporal evolution of temperature profiles and movement of the phase interface (solid-liquid), as calculated with the help of the analytical solution and the spatially discretized model. 87
8.3. Comparison of simulation results for calculations with the spatially discretized model using different cell numbers. 88

9.1. Unscaled sketch of the model system with initial and boundary conditions at $t = 0$. 93
9.2. Temporal evolution of the concentration profile (expressed via the oxygen molar fraction x_O), as calculated using the spatially discretized model. . . . 94
9.3. Temporal evolution of the temperature profile as calculated using the spatially discretized model. 94
9.4. Comparison of the progression of phase interfaces, as calculated by means of different models from the literature. 95
9.5. Comparison of the temperatures (sample-averaged), as calculated by means of different models from the literature for the time between $0\,s$ and $100\,s$. . 96
9.6. Comparison of the temperatures (sample-averaged), as calculated by means of different models from the literature for the time between $600\,s$ and $700\,s$. 96

9.7. Comparison of the simulation results regarding the total oxygen uptake expressed via the generated hydrogen mass. 97
9.8. Comparison of cladding temperatures, as calculated by means of different models (case 1). 102
9.9. Comparison of the progression of phase interfaces, as calculated by means of different models (case 1). 103
9.10. Comparison of cladding temperatures, as calculated by means of different models (case 2). 105
9.11. Comparison of the progression of phase interfaces, as calculated by means of different models (case 2). 105
9.12. Comparison of the simulation results regarding the total oxygen uptake expressed via the generated hydrogen mass. 107

10.1. Histogram of temporal temperature changes in the cladding tube material in the base case. 110
10.2. Temporal evolution of the expansion of phases with an imprinted transient of $+5\,K/s$. 112
10.3. Phase fractions of the initially three distinct zones in the integral model (case: $+5\,K/s$). 113
10.4. Integral of hydrogen generation for the model case with an imprinted transient of $+5\,K/s$. 114
10.5. Temporal evolution of the expansion of phases with an imprinted transient of $+30\,K/s$. 116
10.6. Phase fractions of the initially three distinct zones in the integral model (case: $+30\,K/s$). 117
10.7. Integral of hydrogen generation for the model case with an imprinted transient of $+30\,K/s$. 118
10.8. Temporal evolution of the expansion of phases with an imprinted transient of $-5\,K/s$. 119
10.9. Phase fractions of the two distinct zones in the integral model (case: $-5\,K/s$).119
10.10Integral of hydrogen generation for the model case with an imprinted transient of $-5\,K/s$. 121
10.11Temporal evolution of the expansion of phases with an imprinted transient of $-30\,K/s$. 122
10.12Phase fractions of the two distinct zones in the integral model (case: $-30\,K/s$).122
10.13Path of the phase change processes, as calculated using the advanced integral model illustrated in the Zr-O phase diagram. 123
10.14Integral of hydrogen generation for the model case with an imprinted transient of $-30\,K/s$. 124

D.1. Programming flowchart of the script for the initialization of the advanced integral model. 150
D.2. Programming flowchart of the oxidation model of the advanced integral model. 151
D.3. Programming flowchart of the script for the initialization of the spatially discretized model. 152
D.4. Programming flowchart of the oxidation model of the spatially discretized model. 153

E.1. Temporal evolution of the expansion of phases with an imprinted transient of $+10\,K/s$. 156
E.2. Integral of hydrogen generation for the model case with an imprinted transient of $+10\,K/s$. 156
E.3. Phase fractions of the initially three distinct zones in the integral model (case: $+10\,K/s$). 157
E.4. Temporal evolution of the expansion of phases with an imprinted transient of $+60\,K/s$. 158
E.5. Integral of hydrogen generation for the model case with an imprinted transient of $+60\,K/s$. 158
E.6. Phase fractions of the initially three distinct zones in the integral model (case: $+60\,K/s$). 159
E.7. Temporal evolution of the expansion of phases with an imprinted transient of $-10\,K/s$. 160
E.8. Integral of hydrogen generation for the model case with an imprinted transient of $-10\,K/s$. 160
E.9. Phase fractions of the two distinct zones in the integral model (case: $-10\,K/s$). 161

List of Tables

2.1. Composition of commercial zirconium-based cladding alloys. 8
2.2. Values for oxygen diffusion coefficients in zirconium and stoichiometric zirconia between 1273 K and 2128 K. 13

4.1. Comparison of invariant points in the Zr-O binary system as they are indicated by the lookup table and the phase diagram of Abriata et al. [1]. . 46

5.1. Correlations for the estimation of parabolic rate constants by different authors. 52
5.2. Correlations for the estimation of diffusion coefficients of oxygen in α-Zr by different authors. 55
5.3. Correlation for the estimation of diffusion coefficients of oxygen in β-Zr. . . 55
5.4. Correlations for the estimation of diffusion coefficients of oxygen in β-ZrO$_2$ by different authors. 56
5.5. Correlations for the estimation of diffusion coefficients of oxygen in dublex oxide (β-ZrO$_2$ and γ-ZrO$_2$) by different authors. 57

8.1. Auxiliary input used to verify the mass transfer models. 85
8.2. Auxiliary input used to verify the heat transfer models. 87

Nomenclature

Latin symbols:

A	$[m^2]$	area
$\hat{A}$		constant
$\tilde{A}$		pre-exponential factor (Arrhenius equation)
a	$[m^2/s]$	thermal diffusivity
$\hat{B}$		constant
C		constant
c		chemical component index
c_p	$[J/kgK]$	isobaric heat capacity
D_O	$[m^2/s]$	oxygen diffusion coefficient
E	$[J/mol]$	activation energy (Arrhenius equation)
f	$[-]$	phase fraction
G	$[J]$	Gibbs free energy (free enthalpy)
H	$[J]$	enthalpy
h	$[J/kg]$	specific enthalpy
$\overline{h}$	$[J/kg]$	volume-averaged specific enthalpy
h_m	$[J/mol]$	molar enthalpy
i		cell index (spatially discretized model)
j		phase index
j_O	$[kg/m^2s]$	oxygen mass flux
k		parabolic rate constant
k_B	$[J/K]$	Boltzmann constant
k_{ox}	$[m/\sqrt{s}]$	parabolic rate constant (growth of the oxide scale)
k_τ	$[kg/m^2\sqrt{s}]$	parabolic rate constant (total mass gain)
M	$[kg/mol]$	molar mass
m	$[kg]$	mass
N	$[mol]$	amount of substance
$\dot{N}$	$[mol/s]$	flux of an amount of substance
n	$[-]$	index
$\vec{n}$	$[-]$	normal vector
p	$[Pa]$	pressure
Q	$[J]$	heat
q	$[W/m^2]$	heat flux

R	$[J/molK]$	universal gas constant
r	$[m]$	ionic radius
S	$[J/K]$	entropy
s	$[m]$	oxide layer thickness
T	$[K]$	temperature
$\overline{T}$	$[K]$	volume-averaged temperature
t	$[s]$	time
u	$[s]$	time variable
V	$[m^3]$	volume
v	$[m/s]$	velocity
$\vec{v}$	$[m/s]$	velocity vector
x	$[m]$	length
x_O	$[-]$	molar oxygen fraction
z		zone index (integral model)

Greek symbols:

$\alpha_{env.}$	$[W/m^2K]$	heat transfer coefficient
α		allotropic modification
β		allotropic modification
Γ	$[m^2]$	area
γ		allotropic modification
Δ	$[-]$	absolute difference
ϵ	$[-]$	interpolation factor
η	$[Pas]$	dynamic viscosity
λ	$[J/mK]$	thermal conductivity
μ		chemical potential
ρ	$[kg/m^3]$	density
ρ_O	$[kg/m^3]$	mass concentration (oxygen partial density)
$\overline{\rho}_O$	$[kg/m^3]$	volume-averaged mass concentration (oxygen partial density)
ϕ	$[-]$	phase volume fraction
Ψ		constant of proportionality
Ω	$[m^3]$	volume
ω	$[-]$	weighting factor

Subscripts:

$_{c}$	chemical component index
$_{chem.-trans.}$	chemically-induced phase transition
$_{diss.}$	dissociation of steam
$_{el.}$	electrical

$fusion$	fusion
H_2	hydrogen
i	cell index (spatially discretized model)
$int.$	at the phase interface
O	oxygen
R	reaction
SER	Standard Element Reference
$sol.$	solution
$surf.$	surface
$th.$	thermal
$therm.-trans.$	thermally-induced phase transition
$virt.$	virtual
Zr	zirconium
z	zone index (integral model)
0	system's inner perimeter
$-$	left-hand side boundary of a zone, cell, or control volume
$+$	right-hand side boundary of a zone, cell, or control volume

Superscripts:

j	phase index (spatially discretized model)
$*$	phase equilibrium, at phase interface

Abbreviations:

AECL	Atomic Energy of Canada Limited
CALPHAD	Calculation of Phase Diagrams (method)
EPR	European Pressurized Water Reactor
FZKA	Forschungszentrum Karlsruhe
IRSN	Institut de Radioprotection et de Sûreté Nucléaire
IAEA	International Atomic Energy Agency
TEPCO	Tokyo Electric Power Company

1. Motivation

1.1. High-temperature zirconium oxidation

Due to their favorable neutron physical properties, zirconium alloys are used as materials for the fuel rod claddings and core structures of modern light water reactors. As a result of intense development efforts, modern alloys show good corrosion resistance under normal operating conditions. However, when heated to temperatures above 1000 °C to 1200 °C, zirconium enters an exothermic chemical reaction with steam. In consequence of this high-temperature oxidation, ductile metallic material is transformed into brittle oxidic zirconium dioxide, combustible hydrogen gas is formed, and vast amounts of heat are released, which can cause a further self-acceleration of the process.

$$Zr_{(s)} + 2H_2O_{(g)} \rightarrow ZrO_{2(s)} + 2H_{2(g)} + \Delta H_R \tag{1.1}$$

$$\Delta H_R = \Delta H^0_{f,ZrO_2,s} - 2\Delta H^0_{f,H_2O,g} = -596\frac{kJ}{mol} \tag{1.2}$$

The significance of this reaction for reactor safety was vividly demonstrated by the severe accidents at the Three Mile Island Nuclear Generating Station (1979) and the Fukushima Daiichi Nuclear Power Plant (2011). In both incidents, the high thermal output of the high-temperature oxidation reaction facilitated partial core meltdowns and led to hydrogen explosions of a greater or lesser extent.

1.2. Loss-of-coolant accidents

A commercial pressurized water reactor of the European Pressurized Water Reactor (EPR) design, such as the nuclear power station Thaishan-1, generates a thermal power of up to 4590 $MW_{th.}$ and an electrical power output of 1750 $MW_{el.}$ [2]. Under stable operating conditions, 93 % of this power results from nuclear fission reactions, while 7 % (321 $MW_{th.}$) results from the decay of radioactive fission products. Even after the controlled termination of the fission reaction via the insertion of control rods into the reactor core, radioactive decay continues. As a result, heat removal systems must remain in operation until the decay is further advanced (see Fig. 1.1 (a)).

If the means of heat removal fail and cannot be restored, water in the nuclear core and cooling circuits will start to heat up. At some point, the water within the reactor pressure vessel will start to boil off, causing the water level to drop and, eventually, the upper tips of the fuel rods to fall dry. Under these deteriorated cooling conditions, the cladding material will heat up until the high-temperature oxidation reaction of zirconium in steam sets in (see Fig. 1.1 (b)).

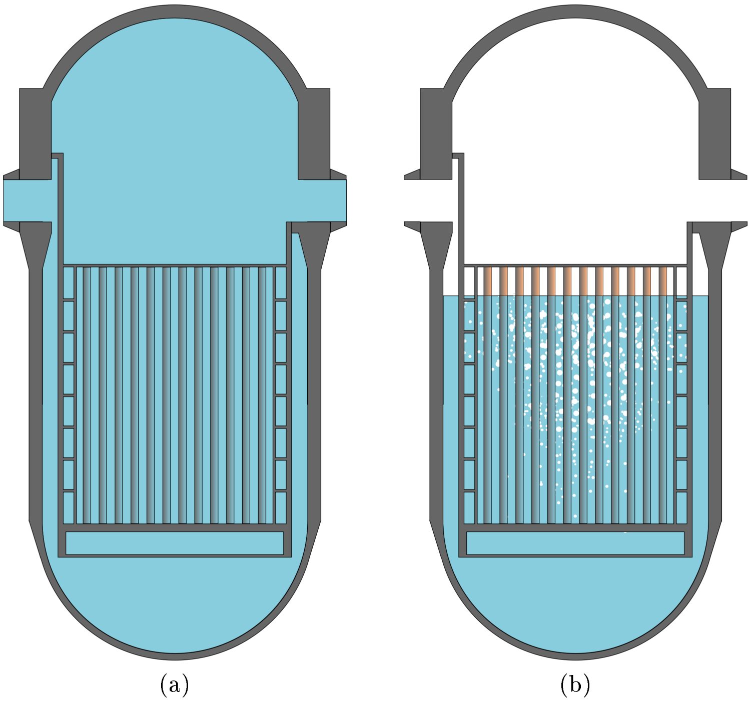

Figure 1.1.: Sketch of a reactor pressure vessel of a pressurized water reactor with sufficient cooling (a) and at the beginning of core uncovery (b).

Once the exothermic reaction starts, its heat release leads to a temperature escalation that rapidly accelerates the core degradation processes. Consequently, the fuel rods start to swell (ballooning) and burst before melting and melt relocation set in (candling). The motion of the melt thereby facilitates the oxidation reaction as it continually forms new surfaces consisting of unoxidized material. As long as steam is available, the generation of hydrogen and heat continues, even if the zirconium is mixed with fuel and structure materials or becomes part of melts or crusts (see Fig. 1.2). Water injections, which are primarily aimed at quenching the core and restoring permanent cooling measures, increase the availability of steam and, in this way, potentially amplify or even reignite the oxidation.

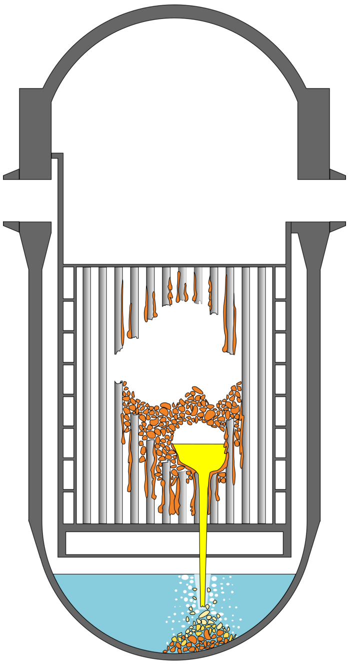

Figure 1.2.: Sketch of a reactor pressure vessel in a pressurized water reactor at an advanced stage of core degradation.

Ultimately, both the hot core melt and the combustible hydrogen gas endanger the integrity of the safety barriers that protect the environment from the release of dangerous radioactive substances.

In the case of unit 2 of the Fukushima Daiichi Nuclear Power Plant (boiling water reactor, Mark I type), the dryout of the core began approximately two and a half days after the facility had been affected by the Tōhoku earthquake and tsunami. Complete meltdown occurred about 12 hours later. Japanese researchers at TEPCO [3], the operator of the Fukushima facility, assumed that the core damage and melting were facilitated by the water injections with fire pumps. They estimated that the related thermal power peak caused by the zirconium-steam reaction was approximately $85\,MW_{th.}$ at a time at which the power from the radioactive decay had already decreased to less than $9\,MW_{th.}$. The total hydrogen mass that was generated in unit 2 was determined to be around $1\,t_{H_2}$. Therefore, it can be concluded that approximately 50 % of the zirconium inventory was oxidized ($m_{Zr} \approx 47\,t$).

1.3. Severe accident analysis codes

In the nuclear industry, the potential of numerical simulations to increase safety was recognized at an early stage. Today, several severe accident analysis codes are used to assess the safety of current and future plant designs, and to develop and optimize existing and new accident management strategies. Most prominent in this context are the integral codes ASTEC, MAAP, MELCOR, and SOCRAT, as well as the mechanistic thermal hydraulics system codes ATHLET, ICARE, and SCDAP-RELAP, which are specialized for the analysis of core degradation processes [4]. The development of these computer tools is a complex task since it requires a compromise between physical precision and computational effort. Each of these codes comprises a large variety of models that, together, aim at a holistic resolution of the diverse physical processes. Due to requirements with respect to computation time, these models must be as efficient as possible and, thus, be compatible with the nodal structures of the codes.

Regarding the reproduction of in-vessel core degradation phenomena, especially thermo-hydraulic models, structure-mechanic models and oxidation models are of major importance. Since each set of models is specialized on one physical sub-process, they share many interfaces as they equally require input and provide output for the others. In this context, the task of the oxidation models is to generate information about the heat and hydrogen generation and the phases present. Again, it completely relies on the thermo-hydraulic and structure-mechanic models in order to resolve (e.g., heat removal or melt relocation processes). In this context, it has been revealed that the low detail and precision of the present oxidation models hinders the ability of severe accident analysis codes to show their full potential [5].

Today's integral codes commonly rely on parabolic rate equations to model the high-temperature oxidation of zirconium in steam. Rate equations are based on an analytical solution of Fick's second law of diffusion, which is derived under certain restrictive assumptions. Examples of these assumptions include isothermal conditions, fixed boundary conditions (ideal steam availability), and semi-infinite space consisting of virgin zirconium (no retardation of the chemical reaction due to saturation effects). However, these assumptions conflict with the real conditions present in severe accidents and even most experimental setups [5, 6]. Therefore, these models give reasonable results if applied to the early phase of core degradation, when geometry and material are largely unaffected, which enables the models to be comparably simple. However, they are associated with serious drawbacks if applied to the late phase of core degradation, include the failure to reproduce saturation effects, the oxidation under steam-starved conditions, and the oxidation of zirconium melts. In this context, their inability to reproduce peaks in hydrogen and heat generation as a consequence of late quenching of degraded structures is a particular disadvantage.

Integral models, which rely on a numerical solution of Fick's second law, relax those restrictive assumptions, and they show the potential to provide significant improvement [5, 6]. Although they require more complex modeling and input, they share the advantage of being relatively computationally inexpensive. However, today's integral models are essentially isothermal models or obtain only a limited applicability to temperature transient processes (see, for example, Veshchunov et al. [7]). Hence, there is a need for advanced models that regard the high-temperature oxidation of zirconium in steam as a coupled heat and mass transfer problem.

The development of an advanced oxidation model is impeded by several factors. The challenge arises from the complexity of modeling the kinetics of a chemical reaction in a thermodynamic system that simultaneously undergoes phase transitions due to changes in both composition and temperature. Hence, a suitable model must combine an accurate depiction of the heat and the mass transport with detailed thermodynamic data, which provides for the chemical interrelations. Furthermore, the lack of single-effect oxidation experiments conducted under temperature transient conditions complicates the development – and especially the validation – of new oxidation models. Hence, the validation of new modeling approaches has to be built on the comparison to other numerical models that are again scarce.

In this light, this work presents the development of an advanced integral model for the description of the high-temperature oxidation of zirconium in steam that is coupled to a novel lookup table comprising physically self-consistent thermodynamic data. It further presents the development of a spatially discretized model that compensates for the lack of experimental data, and which is used as a point of reference in various model tests. However, due to the high numerical cost of its execution, the application of the second model to severe accident analysis codes is not feasible.

1.4. Outline of the present work

To convey a general understanding of the physics, the second chapter of this thesis offers a brief summary of the phenomenology of the high-temperature oxidation of zirconium in steam. Subsequently, the third chapter presents state-of-the-art oxidation models that are currently used in severe accident analysis codes. In this context, their mathematical-physical background is thoroughly analyzed and their limitations are outlined. Based on this information and the assessed availability of the experimental database, requirements for the development of an advanced oxidation model are derived and set as objectives, which substantiate the aim of this work.

The fourth chapter sketches the provision of self-consistent thermodynamic data of the zirconium-oxygen material system with the help of the Institut de Radioprotection et de Sûreté Nucléaire's (IRSN) NucleaToolbox and describes the conversion of such data into a fast-accessible lookup table. The fifth chapter continues from this point with a summary of information regarding material and transport properties that are available from the literature and that are used to form a material library.

The sixth chapter introduces an approach to modify and extend an isothermal integral model in order to cover the various phase changes and heat effects of the chemical reaction. For the later analysis of its capabilities and applicability, the seventh chapter describes the development of an additional spatially discretized model, which compensates for the lack of experimental references. Since both chapters aim at a high replication potential, difficulties regarding the modeling are explicitly outlined and workable solutions presented.

In chapter eight, both models are verified with the help of analytical solutions for simplified heat and mass transfer problems. The ninth chapter is dedicated to model tests, which aim for a comparison of the advanced integral model with state-of-the-art modeling approaches that are used in today's severe accident analysis codes. The chapter begins with the simulation of a plain model case and leads to a test involving complex boundary conditions, which emulate an implementation into a severe accident analysis code. The tenth chapter culminates in a demonstration of the model's capabilities to reproduce complex, thermally-induced phase changes, which lie beyond the range of applicability of the models used today.

The eleventh chapter summarizes the advances made against the background of the work's significance for the modeling of the high-temperature zirconium oxidation in severe accident analysis codes. An additional outlook sketches possibilities for the further development and broader application of advanced integral models that exploit self-consistent thermodynamic data in the context of reactor safety.

2. Phenomena of zirconium oxidation

Different from the impression given by the chemical equation shown in Eq. 1.1, the high-temperature oxidation of zirconium in steam is not a single-step process but a multi-step process. Therefore, this chapter aims to untangle the different facets of the oxidation reaction, which is realized in three parts. The first part is dedicated to the material system. It introduces the alloys that are used in the context of nuclear engineering, presents a binary zirconium-oxygen phase diagram, and describes the gradual conversion of metallic zirconium into oxidic zirconium dioxide. Continuing from this point, the second part offers an insight into oxygen transport kinetics, their dependency on steam availability, and the means for their mathematical-physical description. Finally, the third part introduces and summarizes the relevant heat effects that accompany this chemical reaction and gives a mathematical-physical description for the heat transport.

2.1. Zr-O material system

Zirconium alloys, which are used as the material for fuel rod claddings and reactor core structures, contain more than 95 % of nuclear-grade zirconium. Regarding the further constituents, two families of zirconium alloys can be distinguished. The use of the alloys containing tin (Sn) such as Zircaloy-2 (often: Zr-2 or Zry-2) in boiling water reactors and Zircaloy-4 (often Zr-4 or Zry-4) in pressurized water reactors relates to Western reactor designs. The alloy E 110, which has been frequently used for light water reactors of Eastern design, contains niobium (Nb) as the alloying constituent instead of tin. Exemplary compositions of those alloys, as described in Billone et al. [8], are given in Table 2.1.

Although the aforementioned alloys are widely used today, the ongoing development efforts of manufacturers continually increase the variety of commercially available alloys. Those materials contain either tin or niobium or both constituents with a single digit percentage (approximately 1 % - 2.5 %) besides other constituents in amounts of usually less than 1 % each.

Table 2.1.: Composition of commercial zirconium-based cladding alloys, as given in Billone et al. [8].

wt. %	Zry-2	Zry-4	E 110
Sn	1.45	1.45	-
Nb	-	-	1.0
Fe	0.14	0.21	0.009
Cr	0.10	0.10	-
Ni	0.06	-	-
O	0.125	0.125	0.06
Zr	balance	balance	balance

Each of these alloys, despite being corrosion-resistant, is inevitably subject to oxidation even under the normal operation conditions of a light water reactor. In the course of this chemical process, different phases form depending on the molar oxygen fraction x_O and the temperature T of the material. The binary zirconium-oxygen system, hereinafter referred to as the Zr-O system, comprises five solid solutions and one liquid phase that can occur and exist in thermodynamic equilibrium. These are the metallic phases α- and β-Zr, the oxidic phases α-, β-, and γ-ZrO$_2$, and the liquid phase L. Fig. 2.1 shows the Zr-O binary phase diagram, which was developed by Abriata et al. [1].[1]

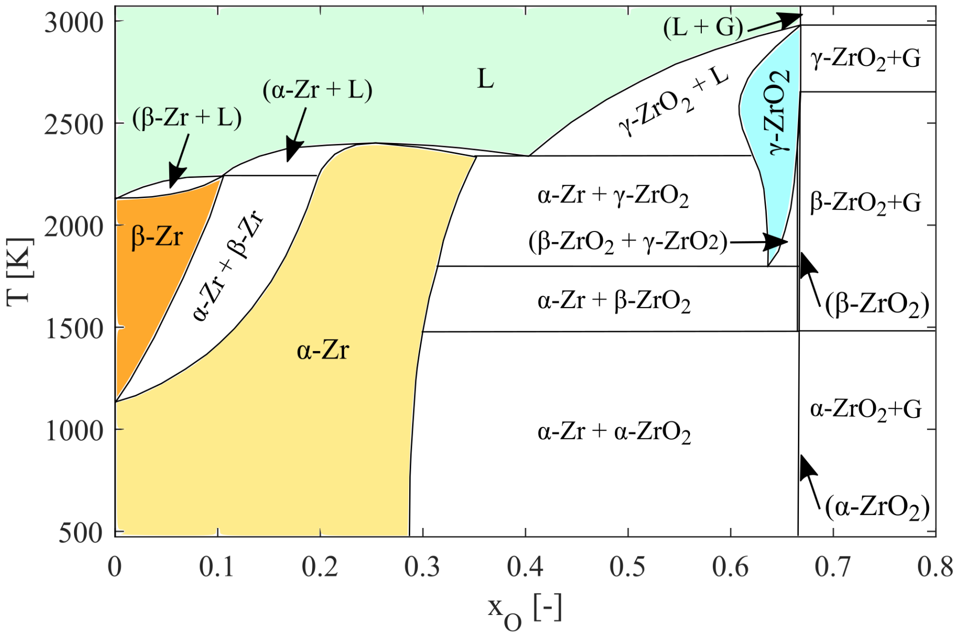

Figure 2.1.: Zr-O binary phase diagram, adapted from Abriata et al. [1].

---

[1] For the sake of clarity in the further course of this work, phase diagrams are presented without color coding and explicit labeling of two-phase regions.

According to the current state of the art, α-ZrO$_2$ only exists in its stoichiometric composition (or very close to it) if a material sample is in thermodynamic equilibrium (see, for example, [9] or [10]). This special characteristic manifests by the fact that the stability region of α-ZrO$_2$, as shown in Fig. 2.1, is so narrow that it can be easily misinterpreted to be a line. The same applies to β-ZrO$_2$, where the stability region is only marginally wider.

According to Lemmon [11], there is a strong resemblance between the stable regions of the phases in the ideal zirconium-oxygen system and the stable phases formed by its alloys. Consequently, phase diagrams of the Zr-O system are commonly applied to the various traditional and modern zirconium alloys in the related literature. Conversely, the Zr-O binary phase diagram is completed as until today using data points that have been determined in experiments with the various alloys.

The validity of a binary state diagram is bound to the condition that the considered system has attained its thermodynamic equilibrium state, which requires infinite time in theory. An oxidation process, in contrast, is caused by a gradient in the oxygen concentration and causes heat sinks and sources. Therefore, oxidation reactions are, in general, hosted by systems that are in global thermodynamic non-equilibrium. To describe such processes with the limited means of equilibrium thermodynamics, spatial subsystems must be identified, which can be assumed to be a local thermodynamic equilibrium. For the Zr-O system, the only investigation regarding the validity of this assumption was published by Iglesias et al. [12]. Although this paper justifies a positive conclusion, the assumption of local thermodynamic equilibrium must be applied with care, ensuring that the subsystems that fall into this category are explicitly labeled throughout this work.

It is known from metallographic examinations (e.g., Bostrom [13]) that oxygen-rich zirconium phases build adherent, non-porous layers on top of the metallic base material if the reaction is caused by the presence of steam (Pilling-Bedworth rule, see Bedworth and Pilling [14]). The transformation of metallic zirconium into oxidic zirconium dioxide (zirconia) is not instantaneously stoichiometric, but it is linked to a gradual increase of the molar oxygen fraction x_O in both time and space. During this process, several phases can form, which, in the case of isothermal conditions, are separated by sharp phase interfaces.

Fig. 2.2 sketches an oxygen concentration profile (expressed via the molar oxygen fraction x_O) that exemplifies microsections of samples retrieved from isothermal cladding oxidation experiments. Following the work of Olander [15], this profile can be described as follows. At the surface, which is in direct contact with steam (Fig. 2.2: a), stoichiometric β-ZrO$_2$ is formed and gaseous hydrogen H_2 is released to the ambient.[2] Within the β-ZrO$_2$ scale, the oxygen concentration decreases to the phase's lower oxygen concentration limit (Fig. 2.2:

---

[2] Embrittlement of cladding tubes due to hydrogen uptake is not considered in this work.

a-b$_{\text{high}}$). Here, a sharp phase interface between oxidic β-ZrO$_2$ and metallic α-Zr forms, which manifests as a rapid reduction in oxygen concentration (Fig. 2.2: b$_{\text{high}}$-b$_{\text{low}}$). The growth of the oxide layer occurs at the expense of the metallic base material. Therefore, the phase interface between oxide and metal moves inward as time progresses, as indicated by the velocity $v_{\text{ox.-met.}}$. The α-Zr layer again spans from the phase's upper to its lower oxygen concentration limits (Fig. 2.2: b$_{\text{low}}$-c$_{\text{high}}$) and verges on a second interface, which separates the α-Zr phase from the β-Zr phase (Fig. 2.2: c$_{\text{high}}$-c$_{\text{low}}$) and moves with the velocity $v_{\alpha-\text{Zr}-\beta-\text{Zr}}$. This interface is, in turn, connected to the oxygen concentration profile of the β-Zr phase, which links its higher concentration limit to the lower oxygen content of the (virgin) base material (Fig. 2.2: c$_{\text{low}}$-d).

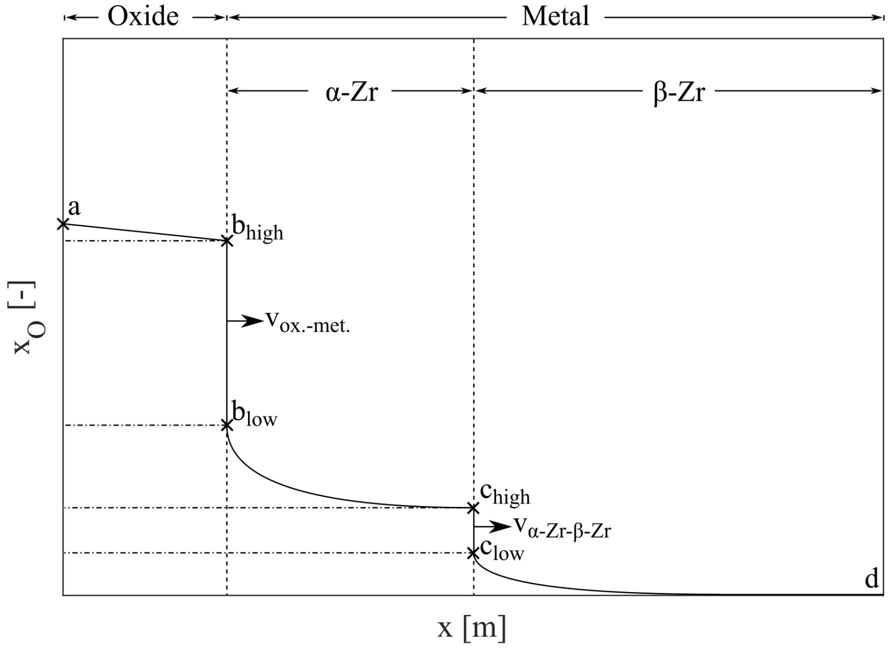

Figure 2.2.: Oxygen concentration distribution during the oxidation of zirconium alloys in steam, following Olander [15], modified.

Accident-tolerant fuels

Over the last decade, both materials scientists and fuel manufacturers have invested substantial effort into the development of so-called accident-tolerant fuels. These fuels, or rather their less reactive claddings, tolerate a disruption of the active cooling measures for a longer time before entering the state of high-temperature oxidation. This effect builds up, for example, on the use of chromium coatings, which delay the onset of the high-temperature oxidation (see, for example, Ševeček et al. [16]). It is possible to use the resulting extended time margin to initiate accident management and mitigation measures, including emergency cooling systems. However, once the protective effect of these claddings is lost, the exothermic nature of the chemical reaction still inevitably leads to its escalation. In chromium coated claddings, this point coincides with the eutectic melting point of chromium and zirconium, which is approximately 1310 °C. From this point on, the need for the development advanced oxidation models remains unaltered. Furthermore, the development of these materials is at an early stage, which means that the classic cladding tube materials are still used today.

2.2. Mass transport

Oxidation reactions can be regarded as mass transfer processes caused by a global non-equilibrium of oxygen concentrations. Since the late 1950s, the kinetic behavior of the high-temperature oxidation of zirconium in steam has been systematically investigated by a large number of scientists. As a result, three regimes are distinguished today:

- Reaction under optimal steam supply (ideal oxidizing conditions)
- Reaction under limited steam supply
- Reaction under the absence of steam (full steam starvation)

Early works in this field trace back to Bostrom [13] and Lemmon [11]. These authors conducted experiments under isothermal conditions, with ideal steam supply and samples, which were thick compared to the ultimate growth of the oxide layer. Their studies revealed that the growth of oxygen-rich phases $\Delta s(t)$ and the gain in oxygen mass $\Delta m_O(t)$ under laboratory conditions are proportional to the square root of time.

$$\Delta m_O(t) \propto \sqrt{t} \tag{2.1}$$

$$\Delta s(t) \propto \sqrt{t} \tag{2.2}$$

Since the oxidation kinetics are limited by the slowest process, it has been concluded that the oxygen anion diffusion in the growing oxide scale is the rate-controlling step under the given conditions. Accordingly, it has been successfully shown that the growth of the oxide follows parabolic rate laws, which is the common understanding today. Correlations describing this very kinetic behavior are, in fact, the standard in the oxidation models, which are implemented into today's severe accident analysis codes. Hence, their mathematical-physical background, as well as their advantages and limitations, are further addressed in Chapter 3.1.

In the course of time, it was found that the oxidation reaction is retarded if the presence of steam is limited or the hydrogen content in the ambient gas phase is increased. Chung and

Thomas [17] found that the reaction is attenuated by a factor of five for a hydrogen molar fraction of the ambient gas phase of 50 %. In contrast, Moalem and Olander [18] observed that the reaction kinetics are independent of the hydrogen content of the environment as long as the hydrogen molar fraction is less than 90 %. Independent on the absolute extent, both groups have identified two major mechanisms that slow the oxidation down as they fall below the anion diffusion in the oxide scale as the slowest process: on the one hand, the deteriorated steam transport from the gas phase to the oxidic surface through the gas phase's boundary layer; and on the other hand, the recombination of dissociated steam molecules. Although no standard correlation arose from this or related studies, their findings are of major importance as they showcase limitations in the applicability of the abovementioned parabolic rate laws.

The understanding of reaction kinetics was advanced by the experimental and theoretical studies of Stuckert and Veshchunov [19], who investigated the oxygen transport under isothermal conditions and the complete absence of steam. Their work shows that oxidic scales, previously grown under oxidizing conditions, are partially or completely consumed by subjacent metallic phases under steam-starved conditions. This finding fits into the picture of experimental investigations on isothermal chemical dissolution processes in systems where oxidic ZrO_2 is in contact with metallic Zr melts (e.g., Hayward and George [20]). In both experiments, the oxidic phases serve the metallic phases as an oxygen source, while the systems strive to attain thermodynamic equilibrium. This striving results in the continuation of oxygen diffusion from the oxidic phases to the metallic phases in order to eliminate persisting differences in the chemical potentials. Since all phases have an upper and a lower stability limit regarding their molar oxygen fraction (see Fig. 2.1), they can act as either oxygen sinks or sources in these reactions. Accordingly, the outcomes of such reactions manifest in different ways depending on the initial departure from equilibrium.

This finding of Stuckert and Veshchunov [19] explains why accident measures that aim at the reflooding and cooling of degraded core structures result in sharp increases in hydrogen and heat generation. Under temporary phases of steam starvation, oxidic scales recede. Therefore, their resistance for the oxygen uptake declines so that the oxidation reaction is strengthened if the steam availability is subsequently restored. Such partly-reversed oxygen mass transfer processes, however, cannot be captured by parabolic rate equations and, thus, call for different modeling approaches.

Parabolic rate laws can be derived from an analytical solution of Fick's second law of diffusion under simplifying assumptions, which largely resemble the conditions in isothermal oxidation experiments (see Sections 3.1 and 3.3). Therefore, the oxygen transport in zirconium alloys in the high-temperature region follows mechanisms that can be described with Fick's second law itself. This knowledge can be made use of to describe systems that are subject to both oxidizing and steam-starved conditions, and it is the general basis of integral models and spatially discretized models. With D_O as the oxygen diffusion coefficient, ρ_O as the partial oxygen density, and t as time, Fick's second law of diffusion reads:

$$\frac{\partial}{\partial t}\rho_O = \nabla\left(D_O \nabla \rho_O\right) \tag{2.3}$$

Independent of the allotropic form of the phase that is present, the dominating oxygen transport mechanism in metallic zirconium phases is interstitial diffusion, while the transport via anion vacancies prevails in oxidic phases [15]. Both diffusive processes are significantly enhanced by microscopic defects such as surfaces and phase and grain boundaries, as well as macroscopic defects such as pores and cracks. The order of magnitude of the transport processes shows an exponential dependency on the temperature. Correlations from the literature, which describe this exponential behavior, are the topic of Chapter 5.2. For the moment, an overview of typical diffusion coefficients of oxygen in both oxygen-free zirconium (metal) and stoichiometric zirconium dioxide at different temperatures is given in Table 2.2.

Table 2.2.: Guide values for oxygen diffusion coefficients in zirconium and stoichiometric zirconia between $1273\,K$ and $2128\,K$ (melting point of Zr), calculated using correlations from Olander [6] and Iglesias et al. [12] (asterisks: extrapolations).

T	$D_{O,Zr}$ in $\frac{m^2}{s}$	D_{O,ZrO_2} in $\frac{m^2}{s}$
$1273\,K$	$7.1 \cdot 10^{-13}$	$1.5 \cdot 10^{-11}$
$1473\,K$	$1.1 \cdot 10^{-11}$	$9.6 \cdot 10^{-11}$
$1673\,K$	$8.9 \cdot 10^{-11}$	$4.0 \cdot 10^{-10}$
$1873\,K$	$4.6 \cdot 10^{-10}$	$1.8 \cdot 10^{-9}$
$2073\,K$	$1.7 \cdot 10^{-9}$ (*)	$4.0 \cdot 10^{-9}$
$2128\,K$	$2.4 \cdot 10^{-9}$ (*)	$4.9 \cdot 10^{-9}$

Considering the exponential relationship and the resulting substantial range of diffusion coefficients, the creeping corrosion of zirconium alloys and, therefore, especially the oxidation of fuel rod claddings under operating conditions of light water reactors can be clearly delineated from the rapid high-temperature oxidation in steam that is observed in the course of nuclear accidents. Under operating conditions, the growth rates of oxide scales on cladding tube surfaces that are in contact with water are typically in the order of $5\,\frac{\mu m}{a}$ to $20\,\frac{\mu m}{a}$ (see, for example, Hillner et al. [21]). At this rate, hydrogen generation and heat release are negligible so that the process is mainly of interest due to its deteriorating effect on the mechanical properties of the cladding tubes. Under higher temperatures, the transformation of metallic zirconium into zirconium dioxide accelerates. The onset of the high-temperature oxidation in steam is often related to cladding temperatures between $1273\,K$ and $1473\,K$. Nevertheless, a uniform definition does not exist in the literature. At these temperatures, the oxide scale grows in the order of some tenths of a micrometer per second on virgin material in a steam-rich environment and, therefore, is approximately five to six orders of magnitude faster than under operating conditions. As a consequence, the exothermic chemical reaction becomes a considerable heat source that can enter a state of self-reinforcement under adverse cooling conditions.

With the onset of melting processes and the emergence of a liquid phase, more complex mass transfer mechanisms based on free and forced convection come into action. For the sake of brevity, these effects will not be described here. This is because they strongly depend on geometric prerequisites and external constraints and are, therefore, dominated by the specifics of a prescribed configuration.

2.3. Heat effects and heat transport

Considering oxidation reactions under non-isothermal conditions substantially increases the complexity of the phenomena related to the high-temperature oxidation of zirconium in steam. The reason for this is because both heat and mass transport are thermodynamically linked via chemistry.

In the previous section, it was explained that the conversion of metallic zirconium into oxidic zirconium dioxide is a multi-step process that occurs along with the formation of a concentration profile (Fig. 2.2). Analogously, the heat of the reaction is not released instantly but over several steps (the same applies for the reverse reaction). In this context, due to the conversion of chemical energy into thermal energy, both the gradual concentration changes of phases within their stability limits ($\Delta H_{sol.}$) and the chemically-induced phase transitions ($\Delta H_{chem.-trans.,}$) manifest as either heat sinks or sources. This heat, in turn, can cause either a change of sensible heat ($\rho c_p \Delta T$), and therefore a gradual change in temperature, or a change of latent heat ($\Delta H_{therm.-trans.}$), and thus a thermal phase transition (e.g., solidification, melting, or an allotropic transformation). For the sake of clarity, Fig. 2.3 illustrates an example for each of the four aforementioned processes, which are depicted as arrows in a binary phase diagram. Aside from these heat effects, further energy contributions must be increased for the chemical dissociation of steam into hydrogen and oxygen ($\Delta H_{diss.}$) at a sample's surface.

Since the abovementioned enthalpy contributions change not only from phase to phase or with the respective phase transition, but also with temperature and molar fractions, a physically consistent description of enthalpy differences between various thermodynamic states is hardly possible to achieve by hand. Today, such tasks are carried out using thermodynamic computer programs and databases. Such an approach is taken in this work and presented in Chapter 4.

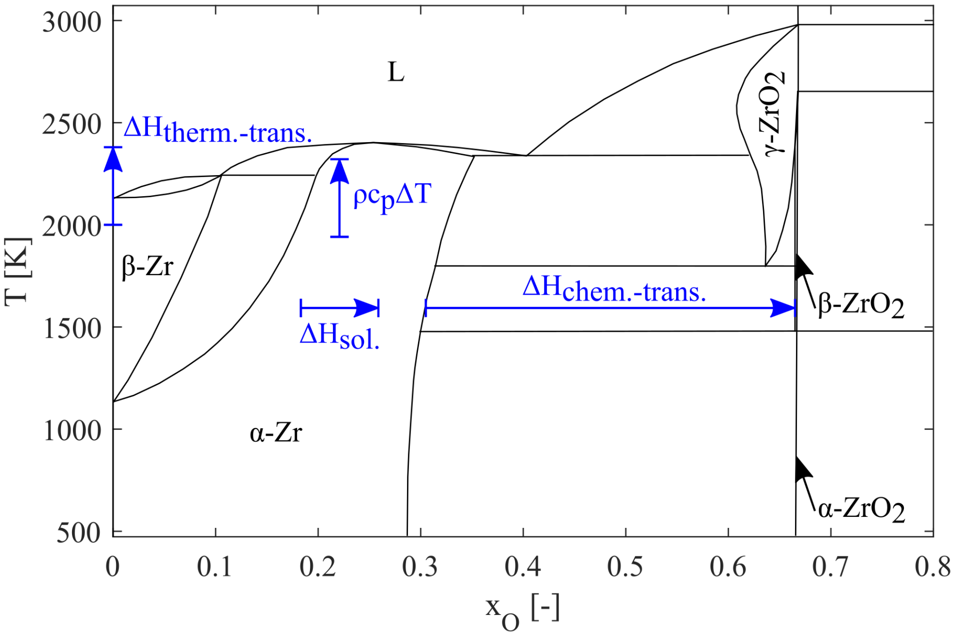

Figure 2.3.: Example of heat effects accompanying the oxidation reaction in the Zr-O phase diagram.

A system that hosts the aforementioned heat sinks and sources, and which is affected by its environment, features a global non-equilibrium of temperatures that gives rise to temperature gradients and the development of complex temperature profiles. The kinetics of heat transfer in solids follow the rules of the heat equation, which shows a strong analogy to Fick's second law of diffusion. With ρh as the enthalpy per volume, λ as the thermal conductivity, T as the temperature, and t as time, the heat equation reads:

$$\frac{\partial}{\partial t}\rho h = \nabla\left(\lambda \nabla T\right) \tag{2.4}$$

In this context, the chemical conversion of the material has a vast impact on the temperature profiles since the thermal conductivities of zirconium metal and zirconium oxide differ by a factor of approximately 30 ($\lambda_{Zr}(1525\,°\mathrm{C}) = 31.4\,\frac{W}{mK}$, $\lambda_{ZrO_2}(1525\,°\mathrm{C}) = 1.1\,\frac{W}{mK}$, as calculated with correlations from Bobkov et al. [22] and Gilchrist [23]). Hence, strong temperature differences can develop in samples with larger geometries and, thus, have a perceptible impact on the oxygen mass transport kinetics, as stated by Berdyshev and Veshchunov [24].

3. State of the art

Computer models for the simulation of zirconium oxidation in severe accident analysis codes combine knowledge about the oxidation reaction, as presented in the previous chapter, with requirements regarding physical precision and computational effort. Hence, this chapter is dedicated to a description and analysis of the state of the art of these models. It aims to unfold their capabilities and limitations and, in this way, to identify requirements for the development of an advanced oxidation model.

Due to the widespread use of models based on parabolic rate laws, this chapter starts with a description of these models. In turn, so-called integral models are made the subject of the discussion, which are advocated by several authors [5, 6, 25]. This is because they can overcome several limitations of the models based on parabolic rate equations. Subsequently, the experimental database is described, which can be used to test, verify, and validate novel modeling approaches. Finally, the outcomes of this chapter are summarized in order to substantiate the aim of this work by defining the objectives that an advanced oxidation model must meet.

3.1. Parabolic rate equations

Mathematical-physical model

Today's integral codes have parabolic rate equations implemented as default models for oxidation in the various stages of possible core degradation processes. As explained in Section 2.2, those equations are based on the consistent findings reported in various experiments between the late 1950s and the 1980s, indicating that the high-temperature zirconium oxidation of virgin zirconium-based cladding materials follows parabolic kinetics, which is limited by the diffusion of oxygen anions through the oxidic scale. This temporal behavior can be substantiated by an analytical solution of Fick's second law of diffusion in one dimension, which is derived under certain simplifying assumptions.

$$\frac{\partial}{\partial t}\rho_O = \frac{\partial}{\partial x}\left(D_O \frac{\partial}{\partial x}\rho_O\right) \tag{3.1}$$

To derive a simple oxidation model, only two substitute phases are considered: the solid oxide scale and the solid metallic base material. These summarize the various respective allotropes (metal: α-Zr and β-Zr; oxide: α-ZrO$_2$, β-ZrO$_2$, and γ-ZrO$_2$). Following this assumption, a set of partial differential equations for the oxide scale and the metallic base material can be established (see Fig. 3.1):

$$\frac{\partial}{\partial t}\rho_{OI} = D_{O_I}\frac{\partial^2}{\partial x^2}\rho_{OI},\ 0 \le x \le x^*(t) \tag{3.2}$$

$$\frac{\partial}{\partial t}\rho_{OII} = D_{O_{II}}\frac{\partial^2}{\partial x^2}\rho_{OII},\ x(t)^* \le x < \infty \tag{3.3}$$

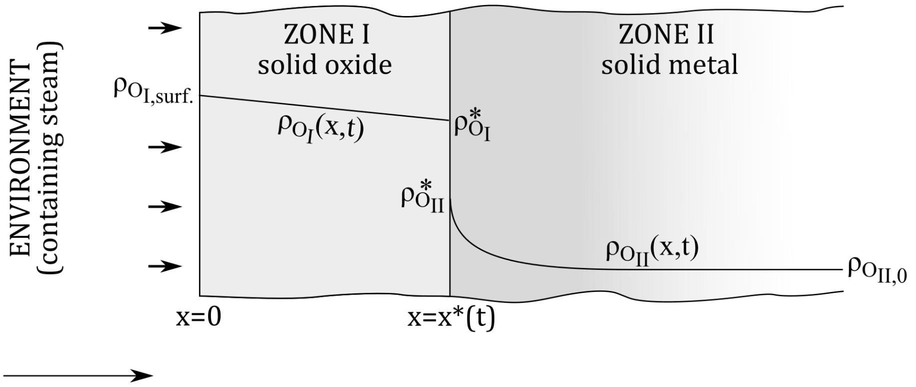

Figure 3.1.: Assumption of composed concentration profiles underlying parabolic rate equations.

In these equations, D_O denotes the oxygen diffusion coefficient depending on the phase present, x the place, and t the time. ρ_O is the oxygen mass concentration, which is also known as partial oxygen density. For reasons of readability, ρ_O is called a concentration throughout this work and the prefix «mass» is omitted.

To obtain an analytical solution, isothermal conditions are assumed. As known from experimental investigations, a sharp interface forms under these conditions (see Section 2.1), which in turn supports the assumption of local thermodynamic equilibrium at the phase interface.

$$\rho_{OI} = \rho_{OI}^*,\ x = x^*(t) \tag{3.4}$$

$$\rho_{OII} = \rho_{OII}^*,\ x = x^*(t) \tag{3.5}$$

In this context, $\rho_{O_I^*}$ denotes the phase equilibrium concentration of the oxide at the position of the phase interface $x^*(t)$ at a time t, and is here again expressed as an oxygen partial density. Analogously, $\rho_{O_{II}^*}$ is the phase equilibrium concentration of the metal. With the help of these equilibrium concentrations, the following moving boundary condition is formulated:

$$(\rho_{O_I^*} - \rho_{O_{II}^*})\frac{\partial x^*}{\partial t} = D_{O_I}\frac{\partial}{\partial x}\rho_{O\,I} - D_{O_{II}}\frac{\partial}{\partial x}\rho_{O\,II}, x = x^*(t) \tag{3.6}$$

To obtain a closed solution, the system of equations is further completed by suitable initial and boundary conditions. It is assumed that there is no zirconium dioxide at the beginning, only a slab of virgin (oxygen-free) metallic zirconium, the surface of which is in contact with steam.

$$x^*(t=0) = 0 \tag{3.7}$$

$$\rho_{O\,II}(t=0) = \rho_{O\,II,0} \tag{3.8}$$

Regarding the left boundary of the system, it is assumed that, due to the chemical reaction of zirconium with steam, stoichiometric zirconium dioxide is permanently formed at the outer surface, which explicitly excludes steam-starved conditions (see Fig. 3.1). Furthermore, a semi-infinite body is assumed, so that saturation effects of the base material are excluded from consideration.

$$\rho_{O\,I} = \rho_{O\,I,surf.},\ x = 0 \tag{3.9}$$

$$\rho_{O\,II} = \rho_{O\,II,0},\ x \to \infty \tag{3.10}$$

The analytical one-dimensional solution further requires the assumption of the immutability of parameters such as the oxygen diffusion coefficients D_O, the densities ρ, and the phase interface concentrations $\rho_{O_I^*}$ and $\rho_{O_{II}^*}$. This assumption is only true for the aforementioned isothermal conditions.

Following the assumption of local thermodynamic equilibrium, the information regarding the oxygen partial densities $\rho_{O_I^*}$ and $\rho_{O_{II}^*}$ at the phase interface can be obtained using the given state equations or a state diagram such as the Zr-O binary phase diagram (see Fig. 3.2). For the described system of equations (Eq. 3.2 to Eq. 3.10) a similarity solution exists:

$$\rho_{O\,I}(x,t) = \hat{A}_I + \hat{B}_I erf\left(\frac{x}{2\sqrt{D_{O_I}t}}\right),\ 0 \leq x \leq x^*(t) \tag{3.11}$$

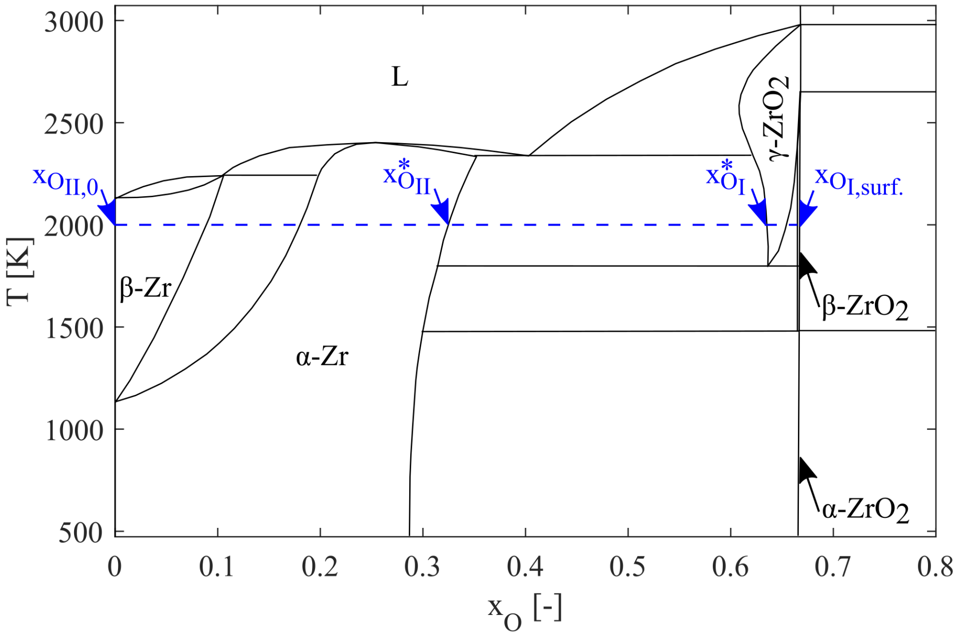

Figure 3.2.: Determination of phase boundary concentrations using the binary Zr-O phase diagram for an exemplary isothermal system.

$$\rho_{O_{II}}(x,t) = \hat{A}_{II} - \left[1 - \hat{B}_{II} erf\left(\frac{x}{2\sqrt{D_{O_{II}}t}}\right)\right], \quad x^*(t) \le x < \infty \tag{3.12}$$

This similarity solution is based on the Gauss error function and comprises four factors ($\hat{A}_I$, $\hat{B}_I$, $\hat{A}_{II}$ and $\hat{B}_{II}$), which are only based on the respective diffusion coefficients and boundary conditions. Moreover, the system defined by Eq. 3.11 and Eq. 3.12 has a solution at $x = x^*(t)$ only if the position of the interface at $x^*(t)$ itself is a function of the square root of time:

$$\frac{x^*(t)}{2\sqrt{t}} = const. \tag{3.13}$$

The required constant again is a function of the diffusion coefficients D_O and the interface concentrations ρ^*_O of both the oxide and the metal. Continuing from this point, it is possible to derive an analytical solution based on diffusion coefficients and phase equilibrium concentrations. Such a solution is used in Chapter 8 for the verification of the numerical models, which are developed in the framework of this work. To develop parabolic rate equations, however, a detailed consideration of these parameters can be omitted because the constant can be directly obtained from experiments. Actually, parabolic rate constants are used to derive the diffusion coefficients that are required in more detailed zirconium oxidation models (i.e., integral models). Depending on the techniques used for the execution and evaluation of the experiment, either a rate constant for the growth of the oxidic scale k_{ox} or a rate constant for the mass gain k_τ, or both, are provided. The corresponding rate equations usually take the following form:

$$x^*(t) = k_{ox}\sqrt{t} \tag{3.14}$$

$$\Delta m_O(t) = k_\tau \sqrt{t} \tag{3.15}$$

The standard correlations used in this context are those of Baker and Just [26], Prater and Courtright [27], Urbanic and Heidrick [28], or Cathcart and Pawel [29]. Those correlations are further analyzed in Section 5.1, which is devoted to an assessment of the set of material and transport properties that is available in the literature.

Due to the assumptions made, the use of parabolic rate equations underlies certain restrictions. The equations cannot be used in situations in which isothermal conditions are not present because, here, both the diffusion coefficients and the thermodynamic states at the phase interface are subject to changes. Furthermore, they are not applicable to situations in which the outer boundary conditions change. Therefore, it has to be excluded that saturation effects in the base material occur, so that their application to spatially finite systems is limited. This also means that only oxidation processes under ideal oxidizing conditions are covered and that the equations, in turn, cannot be applied to situations of steam starvation in which either a slowdown of the reaction or its reversal can be observed.

The fact that none of these assumptions is met under accident conditions and even in most experiments (temperature transient, finite bodies) is a flaw. However, it is largely accepted as a trade-off between the easy implementation and numerical simplicity of these models and their physical inaccuracy. Nevertheless, lately, the negative impact of these models on the overall performance of the evolving severe accident analysis codes has become increasingly obvious. Thus, several authors advocate the development and deployment of more advanced modeling approaches such as integral models [5, 6, 25, 30]. Since all of the aforementioned deficits are intrinsic to the parabolic approach, it is impossible to derive an advanced oxidation model on its basis.

Generation of hydrogen and heat

It is a common approach applied in severe accident codes to calculate the generation of hydrogen and heat directly from the oxygen uptake $\frac{dm_O}{dt}$. To do so, the first time derivative of Eq. 3.15 must be established:

$$\frac{dm_O}{dt} = \frac{k_\tau(T)}{2\sqrt{t}} \tag{3.16}$$

Under the assumption of an instantaneous chemical conversion, the generation of hydrogen $\frac{dm_{H_2}}{dt}$ and heat $\frac{dQ}{dt}$ can be readily calculated from the oxygen uptake using the chemical equation given in Eq. 1.1. In the case of hydrogen generation $\frac{dm_{H_2}}{dt}$, this calculation is a plain conversion task using the molar masses of the oxygen and hydrogen molecules (M_{O_2} and M_{H_2}).

$$\frac{dm_{H_2}}{dt} = \frac{dm_O}{dt}\frac{M_{H_2}}{M_{O_2}} \tag{3.17}$$

Analogously, heat generation $\frac{dQ}{dt}$ is calculated as the product of the molar oxygen uptake $\frac{dN_O}{dt}$ and the difference of the enthalpies of formation of gaseous water $\Delta H^0_{f,H_2O}$, which has to be increased for its dissociation, and zirconium dioxide $\Delta H^0_{f,ZrO_2}$, which is released as a consequence of the oxidation of metallic zirconium. The temperature dependency of the enthalpies and a differentiation between different allotropes of the zirconium dioxide (ZrO_2) that can be formed are usually neglected.

$$\frac{dQ}{dt} = \frac{dm_O}{dt}\frac{\Delta H_R}{M_{O_2}} \tag{3.18}$$

These equations must be supported by an energy balance that provides for a temperature feedback and, thus, an update of the temperature-dependent rate constants. This balance is commonly, albeit loosely, coupled to the thermo-hydraulic models of a code. The advantage of such an approach to cover the heat effects of the oxidation reaction is again its simple implementation because the oxygen uptake, the generation of hydrogen, and the release of heat are covered by three equations only.

Since transient temperatures can lead to massive changes in the oxidation rate, it is reasonable to track the history of the oxidation reaction in order to incorporate the inhibiting effect of the oxide layer appropriately. To do so, such models, despite being based on parabolic rate equations, require a numerical solution. A plain model that follows these ideas, and which is developed and used in the course of this work, is presented in Appendix A.

Adding to the disadvantages intrinsic to parabolic rate equations, the application of isothermal models to calculate heat effects is, at the very least, questionable. Against the background of the large differences in the values of the thermal conductivities in metallic zirconium and oxidic zirconia, a uniform temperature profile does not seem likely. However, the consideration of spatial temperature non-uniformities calls for more elaborate modeling approaches.

The assumption to regard the heat effect of the chemical reaction as a single heat source further conflicts with the fact that the conversion from metallic Zr into oxidic ZrO_2, along with the corresponding release of chemical reaction heat, is a multi-step process. In this context, Olander [15] presented three modeling approaches based on parabolic rate equations, which take this consideration into account. He reported that such modeling results in differences of less than 3 % regarding the release of chemical heat compared to the trivial solution. Considering the substantial increase in the modeling effort, the high number of additional assumptions, and the high degree of uncertainty regarding the enthalpies of the partial chemical reactions, such an approach can be considered unreasonable. Nevertheless, the basic considerations of these models are summarized in Appendix B because their ideas have been used by other authors to develop an integral model that considers heat effects. This is picked up in Section 3.2 and tested in comparison to other models in Section 9.1.

3.2. Integral diffusion models

Use in the literature

In general, integral models can be used for the description of either heat or mass transport problems involving a change of phase (however, they cannot be applied to coupled heat and mass transfer problems that cause phase changes). Hence, they can be applied to solidification and melting problems in unary systems (e.g., water and ice) or to reproduce diffusion-controlled chemical reactions under isothermal conditions (e.g., zirconium oxidation).

Olander [6] introduced the integral approach for the modeling of the isothermal oxidation of solid zirconium in the early phase of core degradation and, thus, the oxidation of fuel rod claddings. He proposed it as an alternative to the simplified parabolic rate equations in order to lift some of their restrictive assumptions such as semi-infinite geometries or unlimited steam supply. Consistent with Olander's motivation, Stuckert et al. [19] demonstrated that isothermal integral models can reproduce the results of experimental investigations of the oxidation of fuel rod claddings between approximately 1300 °C and 1500 °C.

As part of the same working group as Stuckert et al., Hofmann et al. [25] and Veshchunov et al. [31] compared simulations using isothermal integral models to experimental data describing the dissolution of zirconium dioxide crucibles by liquid zirconium melt (2100 °C to 2300 °C). Their work indicated that integral models are applicable to solid-liquid systems and are capable of correctly reproducing the temporal behavior of isothermal chemical dissolution and solidification processes. In addition, to model fuel-cladding chemical interactions, Veshchunov et al. [31] and Müller et al. [32] extended the material system to cover not only zirconium and oxygen but also uranium. Through both the modeling of solid-liquid systems and the extension to the U-Zr-O system, initial steps were made towards the modeling of the corium oxidation that occurs during the late phase of core degradation.

The implementation of these models into severe accident analysis codes has been limited by the lack of thermodynamic phase equilibrium data for the U-Zr-O system. In this context, further advances were made by developers of ICARE at IRSN, who coupled an isothermal integral model to the thermodynamic computer code GEMINI. This code is capable of supplying the oxidation model with the required thermodynamic data but is computationally expensive. Therefore, Nigbur et al. [33] took the idea one step further and coupled an isothermal integral model to a quickly accessible lookup table comprising such thermodynamic data.

Another significant improvement was made by Veshchunov et al. [7]. Based on an approach first presented by Olander [15] in the context of parabolic rate laws, these authors developed an integral model that overcomes the limitation to isothermal conditions at least partially, and which can cover the mass transfer related heat effects. However, since this model relies on fragmentary and inconsistent thermodynamic data supplied in the form of constants, it is restricted to limited temperature ranges and, in general, incapable of capturing systems undergoing complex, especially temperature-induced, phase transitions (e.g., solidification or melting processes).

Due to the limitation to isothermal conditions of some integral models and the reliance on fragmentary thermodynamic data of others, integral models can only be found in some codes such as ICARE and SOCRAT today, where they are primarily used for the description of chemical fuel dissolution. Consequently, a widespread application of the integral approach as an oxidation model has not yet been established.

Isothermal mass transport model

Similar to models based on parabolic rate equations, integral models consider the oxidation reaction as a mass diffusion-controlled moving boundary problem but go after its numerical solution (parabolic rate equations: analytical solutions). With the help of integral models, the high numerical expenditure of a solution of the partial differential equation describing the mass transfer process, Fick's second law of diffusion, on a discrete grid can be avoided.

To achieve this, integral models build up on mass balance approximations that summarize phases into zones. Thus, distinct metallic and oxidic phase are represented by individual zones, which are separated by moving interfaces. Their high modeling effort and input complexity is rewarded by the capability to model the oxygen transport without most of the restrictions of parabolic rate equations. Hence, they are applicable to systems with arbitrary geometries (e.g., thin claddings), allow a free choice of initial conditions (e.g., pre-oxidized based material), and can even be used in combination with changing boundary conditions. Therefore, they enable the consideration of the phases of steam starvation and even capture a reversal of the progression of phase interfaces as it can be observed (i.e., in chemical dissolution experiments).

A typical isothermal integral model is based on a one-dimensional approach covering adjacent zones, an example of which is given in Fig. 3.3. In analogy to the mathematical derivation of the parabolic rate equations, the materials chemistry and oxygen transport are described with basic diffusion theory as a boundary value problem with a moving boundary condition.

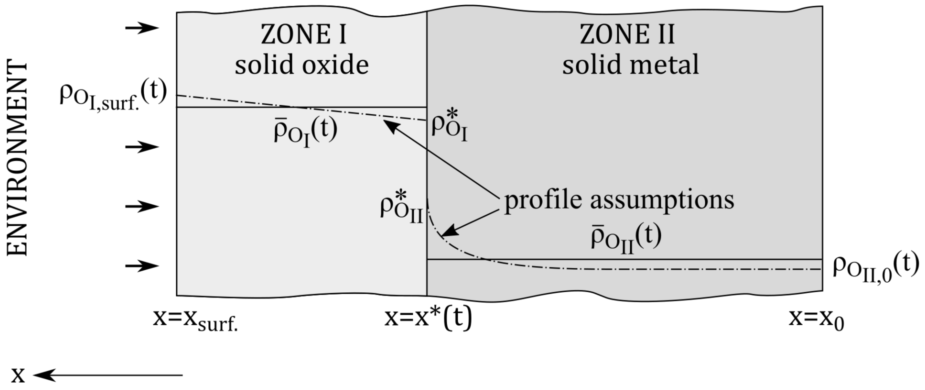

Figure 3.3.: Composed oxygen concentration profile of an exemplary integral model consisting of a partial profile for the oxide and a partial profile for the metal (arbitrary boundary conditions).

An integral model is based on the hypothesis that oxygen is the only diffusing component. Hence, the zirconium, whose diffusivity is smaller compared to that of oxygen, is viewed merely as a stationary host matrix. Consistent with experimental observations and similar to the approach of parabolic rate equations, a sharp phase interface is assumed. Accordingly, the transition between two zones at an interface is assumed to be small and its mass is neglected. The moving boundary condition is again linked to the assumption of local thermodynamic phase equilibrium. The concentration profiles within the phases are assessed using appropriate model representations that are consistent with the boundary conditions at the phase interfaces. As illustrated graphically in Fig. 3.3, the assumption of local thermodynamic equilibrium implies a jump in the concentration profile at the inner phase boundary. The initial and boundary conditions of an integral model can be chosen freely as long as they are consistent with the thermodynamic phase diagram. Hence, at a system's outer perimeters, for example, ideal oxidizing conditions can be implemented (e.g., as a Dirichlet condition) or reflective boundary conditions can be chosen in order to simulate a case of full steam starvation (e.g. as a Neumann condition). Applying the aforementioned assumptions, a differential-algebraic system of mass balances and equations for the velocities (positions) of the interfaces between different zones is set up.

In the rest of this section, the mathematical-physical equations for an isothermal integral model for the high-temperature oxidation of zirconium in steam are derived in detail. As a first step, mass balances are set up for each component c (Zr, O) in each respective zone. The integral mass balance equation for volume Ω confined by its surface $\partial\Omega$ can be expressed as:

$$\frac{D}{Dt}\int\limits_{\Omega} \rho_O dV = -\int\limits_{\Omega} \nabla \vec{j_O} dV \tag{3.19}$$

where ρ_O is the partial density (mass concentration) of oxygen, j_O is the oxygen mass flux, and t is time. Applying Gauss's and Reynolds's theorems yields:

$$\int\limits_{\Omega} \frac{d}{dt}\rho_O dV = -\oint\limits_{\partial\Omega} \left(\vec{j_O}\cdot\vec{n}\right) dA + \oint\limits_{\partial\Omega} \rho_O \left(\vec{v}\cdot\vec{n}\right) dA \tag{3.20}$$

Considering a one-dimensional case as shown in Fig. 3.4, which presents a volume Ω confined by two surfaces at x_- and x_+ (which is suitable for the implementation into the nodal structure of severe accident analysis codes), the equation can be transformed into its integral form:

$$\Delta x \frac{d}{dt}\overline{\rho}_O = -\left[j_{O+} - j_{O-} - \left(\rho_{O+}v_+ - \rho_{O-}v_-\right)\right] \tag{3.21}$$

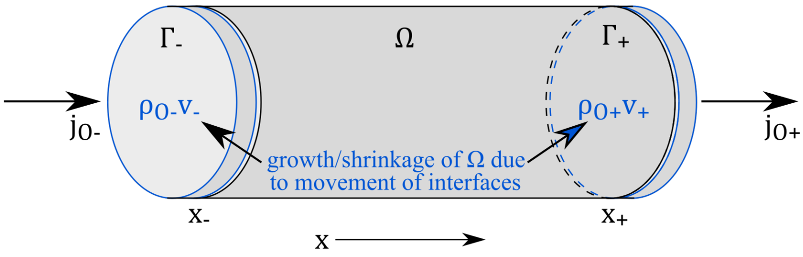

Figure 3.4.: Schematic illustration of a volume Ω confined by two surfaces Γ_+ and Γ_-.

Generalized for a zone z, such as zone I ($z = I$) or zone II ($z = II$) in Fig. 3.3, confined by its right and left interfaces at x_+ and x_-:

$$\Delta x_z \frac{d}{dt}\overline{\rho}_{Oz} = -\left[j_{Oz,+} - j_{Oz,-} - \left(\rho_{O+}v_+ - \rho_{O-}v_-\right)\right] \tag{3.22}$$

where $\overline{\rho}_O$ is the bulk averaged oxygen partial density (mass concentration) of a zone z; j_{O+} and j_{O-} are (diffusive) mass fluxes over the zone's phase boundaries Γ_+ and Γ_-, which are evaluated at x_+ and x_-; and $\rho_{O+}v_+$ and $\rho_{O-}v_-$ are material losses or gains due to the movement of the interfaces Γ_+ and Γ_-, which cover the growth or shrinkage of the zone due to phase changes. According to the use of zone-averaged mass concentrations $\overline{\rho}_O$, material properties are treated as bulk properties and assumed to be independent of the local oxygen concentration.

Since the information about the oxygen concentration profiles $\rho_O(x)$ is lost in the integration process, it is necessary to find an appropriate model representation for the concentration gradients at the positions of the phase interfaces $\frac{\partial \rho_O}{\partial x}$. In a first approach, those gradients can be approximated as the difference in the oxygen partial density calculated from the bulk value $\overline{\rho}_O$ and the value at the respective phase boundary ρ_O^* divided by the distance between the zone's center and the corresponding phase interface Δx. The phase equilibrium concentration ρ_O^* (here, ρ_{O+} and ρ_{O-}) is part of the moving boundary condition. An exemplary oxygen flux reads:

$$j_{O+} = D_O \frac{d}{dx} \rho_O \bigg|_{x=x_+} \approx D_O \frac{\Delta \rho_O}{\Delta x} = D_O \frac{\rho_{O+} - \overline{\rho}_O}{0.5 \Delta x} \tag{3.23}$$

A more elaborate means of calculating the fluxes, which is based on the assumption of parabolic concentration profiles, can be found in Appendix C.

The phase change is included via the velocity v of the phase interface between two zones, which is deduced from an integral balance equation evaluated at the respective interface Γ between two zones (e.g., zone I and zone II) (see Fig. 3.5):

$$\begin{aligned} &\frac{D}{Dt} \int\limits_{\Omega_I} \rho_{OI} dV + \frac{D}{Dt} \int\limits_{\Omega_{II}} \rho_{OII} dV + \frac{D}{Dt} \int\limits_{\Gamma} \rho_{O\Gamma} dV = \\ &\qquad - \oint\limits_{\partial \Omega_{II}} \left(\vec{j}_{OI} \cdot \vec{n}_I \right) dA - \oint\limits_{\partial \Omega_{II}} \left(\vec{j}_{OII} \cdot \vec{n}_{II} \right) dA - \oint\limits_{\partial \Gamma} \left(\vec{j}_{O\Gamma} \cdot \vec{n}_\Gamma \right) dA \end{aligned} \tag{3.24}$$

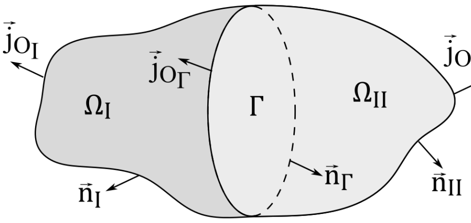

Figure 3.5.: Schematic illustration of a surface Γ dividing two volumes Ω_I and Ω_{II}.

Applying Reynolds's theorem and conducting a contraction of the volumes $\Omega_I \rightarrow 0$, $\Omega_{II} \rightarrow 0$ and $\Gamma \rightarrow 0$, and the surfaces $\partial\Omega_I \rightarrow \partial\Gamma$ and $\partial\Omega_{II} \rightarrow \partial\Gamma$, yields the following equation for a one-dimensional case:

$$0 = -\left[j_{O\,I} - j_{O\,II} - \left(\rho_{O\,I} - \rho_{O\,II}\right) v_\Gamma\right] \tag{3.25}$$

This equation can be transformed into an expression for the movement of the interface:

$$v_\Gamma = \frac{j_{O\,I,+} - j_{O\,II,-}}{\rho_{O\,I,+} - \rho_{O\,II,-}} \tag{3.26}$$

The velocity v_Γ of the phase interface separating two zones covers phase changes from the imbalance of diffusive mass fluxes to the left and right side of the interface. Hence, the solution of Eq. 3.22 and Eq. 3.26 requires a consistent treatment of the concentration leap at the phase interface in the form of donor and acceptor concentrations $\rho_{O\,I,+}$ and $\rho_{O\,II,-}$, which depend on the direction of the interface's velocity. To avoid unphysical results, it is specified that the donor phase loses material with its bulk concentration $\overline{\rho}_O$ while the acceptor phase gains material with its equilibrium concentration ρ_O^* at the phase interface.

The resulting system of equations obtained for the mass transport problem consists of two mass balances (ordinary differential equations, one equation for each component c (Zr, O), Eq. 3.22) for each phase/zone and one algebraic equation for the velocity of each inner phase interface (Eq. 3.26). The following system of equations describes the mass transfer at the example of the system depicted in Fig. 3.3. This system consists of an inner metallic zone (α-Zr) and an outer oxidic zone (γ-ZrO$_2$), which is in contact with the environment and, hence, is one-sidedly oxidized by the reaction with steam.

$$v_{int.} = \frac{j_{O\,I,int.} - j_{O\,II,int.}}{\rho_{O\,I,int.} - \rho_{O\,II,int.}} \tag{3.27}$$

$$\Delta x_I \frac{d}{dt}\overline{\rho}_{O\,I} = -\left[j_{O\,I,surf.} - j_{O\,I,int.} - \left(-\rho_O v_{int.}\right)\right] \tag{3.28}$$

$$\Delta x_{II} \frac{d}{dt}\overline{\rho}_{O\,II} = -\left[j_{O\,II,int.} - \left(\rho_O v_{int.}\right)\right] \tag{3.29}$$

$$\Delta x_I \frac{d}{dt}\overline{\rho}_{Zr\,I} = -\left[-\left(-\rho_{Zr} v_{int.}\right)\right] \tag{3.30}$$

$$\Delta x_{II} \frac{d}{dt}\overline{\rho}_{Zr\,II} = -\left[-\left(\rho_{Zr} v_{int.}\right)\right] \tag{3.31}$$

Such a system of equations is typical for an isothermal integral model. Its solution requires knowledge of the phase equilibrium concentrations $\rho_O^*(T)$, which can be provided, for example, with the help of state equations or a readout of phase diagrams (see

Fig. 3.2). As previously mentioned, a modern approach involves coupling integral models to thermodynamic codes in order to receive precise information regarding these phase equilibrium data. Such a thermodynamic code and a lookup table comprising thermodynamic phase equilibrium information is presented in Chapter 4. The solution further requires the provision of oxygen diffusion coefficients D_O and densities ρ of the various phases, which is the subject of Chapter 5. It is preempted at this point that due to the scarce availability of material data, it is a common approach to summarize all adjacent solid metallic phases (α -Zr and β-Zr → met.-Zr), all adjacent solid oxidic phases (α-ZrO_2, β-ZrO_2 and γ-ZrO_2 → ox.-Zr), all liquid phases (L) into just one substitutional phase each (see Chapter 5).

Elaborate integral models

As already stated, Veshchunov et al. [7] presented an elaborate integral model that accounts for heat effects in the context of oxidation and dissolution processes in the U-Zr-O system. Nevertheless, their model can readily be reduced to the Zr-O system to match the requirements of this work. Their approach is based on an isothermal integral model as described by Eq. 3.27 to Eq. 3.31, which is extended by one heat balance equation for each respective phase. For a zone z, this equation reads:

$$\Delta x_z \rho_z c_{p_z} \frac{d}{dt} \overline{T_z} = -\left[q_{z,+} - q_{z,-}\right] \tag{3.32}$$

where Δx_z denotes the spatial extension of a zone z, ρ_z its density, c_{p_z} its heat capacity, T_z its temperature, and q_z the heat fluxes over the zone's right and left boundaries. To account for heat effects, their model uses an approach that was developed by Olander [15] in the context of parabolic rate equations (see Section 3.1 and Appendix B). Olander's approach expresses heat effects through the multiplication of oxygen mass fluxes over phase boundaries with specific heat contributions of the respective chemical partial reactions. The application of this approach to an integral model benefits from the fact that the required information regarding the mass fluxes over the various phase interfaces can be readily expressed through the oxygen mass fluxes $j_{OI,surf.}$, $j_{OI,int.}$, $j_{OII,int.}$, and $\rho_{OI,+} v_{int.}$, $\rho_{OII,-} v_{int.}$. The enthalpy contributions of the involved chemical partial reactions are derived from considerations regarding the chemical processes occurring at the interfaces, and can be readily taken from Olander [15]. With both the information about the oxygen mass fluxes and the enthalpy values of the chemical partial reactions at hand, Veshchunov et al. [7] prepared a heat flux balance for the phase interface between metallic zirconium and oxidic zirconia.

$$\underbrace{\lambda_I \frac{T^* - \overline{T}_I}{{}^1\!/_2 \Delta x_I}}_{q_{I,+}} + \underbrace{\lambda_{II} \frac{T^* - \overline{T}_{II}}{{}^1\!/_2 \Delta x_{II}}}_{q_{II,-}} = \left(j_{O_{I,+}} - j_{O_{II,-}}\right) \Delta H_{diff.} + \left(v_{int.} \rho_{int.}\right) \Delta H_{chem.-trans.} \tag{3.33}$$

Considering that the bulk temperatures are the solution variable of the heat balance equations (Eq. 3.32) and that the oxygen mass fluxes are known from the mass transfer model, the interface temperature T^* is the only unknown variable in Eq. 3.33 (ρ_Γ is the known density of the donor phase). Therefore, Eq. 3.33 can be rearranged in such a way as to determine the interface temperature T^*. Subsequently, the interface temperature T^* allows the calculation of the heat fluxes between the interface and adjacent bulks $q_{I,+}$ and $q_{II,-}$, which, in turn, ensure that the heat effects find their way into the heat balances of the phases.

Heat fluxes over the outer boundary of the system are considered via boundary conditions. Through the assumption of temperature profiles, Veshchunov et al. [7] were able to calculate temperatures for each zone bulk, each interface, and the surface (e.g., the outer surface, the oxidic bulk, the inner interface, and the metallic bulk).

The described model is capable of covering phase transitions due to mass transfer processes in systems that are subject to slight temperature variations. Nonetheless, it has to be explicitly stated that this model cannot capture temperature-induced phase transitions such as solidification and melting or allotropic transformations. Hence, the model is limited to the temperature range defined by the stability limits of its predefined phases because phases and phase transitions, the occurrence of which has not been anticipated beforehand, are not captured. Therefore, the model is unsuitable for a holistic representation of heat and mass transport processes, which relate to the high-temperature chemical reaction between zirconium and steam.

The model's advantages compared to the isothermal approach lie in its consideration of temperature variations, which can be used to update thermodynamic properties such as the phase boundary concentrations and material and transport properties. Nonetheless, the approach is associated with certain shortcomings. By adopting Olander's considerations [15], his assumptions are transferred into the new model. Therefore, it is important to review these carefully because they are aimed at their original purpose of developing a model based on parabolic rate equations. In this context, the original model assumes ideal oxidizing conditions and the absence of saturation effects in the metallic base material. Hence, the influence of implicitly adopted assumptions regarding the concentration profiles on the enthalpy values assigned to the chemical partial reactions can adversely affect simulation results, especially if the model is applied to systems that are subject to steam-starved conditions or situations in which saturation effects of the base material can occur. Another disadvantage of the approach is the substantial lack of reliable information regarding the much needed enthalpies of the chemical partial reactions, which both Olander [15] and Veshchunov et al. [7] state.

3.3. Experimental data basis

The development of oxidation models to simulate the high-temperature oxidation of zirconium in steam-containing environments requires a data basis for the testing, verification, and validation of the models and, above all, the assumptions made. Of greatest interest in this context are separate-effect experiments, which ideally combine information on the progress of the oxidation reaction and the accompanying thermal effects.

Various sample geometries are suitable for separate-effect experiments, including zirconium chips, cladding tube pieces, or small crucibles, which are all carried out on a small scale (mm to cm range). In these experiments, temperatures are usually imprinted on the samples using different heating methods, including inductive or resistance heating, or by performing the experiment in furnaces (for an overview, see Schanz [5]). The ambient conditions for the mass transfer are simulated by feeding water vapor or inert gases into the experimental facilities. The simulation of temporally shifting conditions can be implemented using orchestrated experimental procedures.

The implementation of suitable measurement procedures to track important data, which enable the later exploitation of the experiments (i.e., to validate computer models), is not trivial. Temperature measurements are mostly carried out on the surfaces of samples with the aid of thermocouples or pyrometers, whereby the latter method is often subject to high uncertainties due to significant changes in the radiative properties associated with chemical transformations (see, for example, Veshchunov et al. [31]). Real-time monitoring of the oxidation reaction is possible by measuring the increase in weight (gravimetric method) or hydrogen generation, whereby the former is rare and the latter unreliable. High-quality results can be achieved with metallographical and chemical analyses (microsections). Monitoring the reaction with these methods, however, requires considerably greater effort. A temporal sequence can only be investigated by multiple repetitions of identical experiments with initially identical samples, which are stopped after different test durations. Here, the difficulty is to «freeze» the reaction at a point in time by rapid cooling of the sample, whereby allotropic phase changes cannot always be suppressed.

There is a large number of datasets of experiments available, which give insight into isothermal oxidation processes. These originate from the determination of parabolic rate constants in the late 1950s. A detailed overview of the experimental setups and measurement methods applied by various authors and the quality of their investigations is given in Schanz [5]. Most of these investigations cover a temperature range from less than 1000 °C to the melting point of zirconium (1855 °C), with the availability of data becoming increasingly sparse towards higher temperatures. The use of such data for the validation of models that represent temperature transient processes is limited. Nevertheless, since these investigations have contributed significantly to the determination of parameters such as diffusion coefficients and phase equilibrium concentrations, they have a certain influence even on advanced models.

Significantly fewer experiments have been carried out to investigate the isothermal chemical processes under changing, oxidizing, and steam-depleted conditions. A systematic investigation of such processes as part of larger measurement campaigns was conducted at the Forschungszentrum Karlsruhe (FZKA) in Germany [25]. In these experiments, the progression of mass transfer processes over the course of time was tracked by metallographical analyses of samples at the beginning and end of a test or a respective test sequence. These experiments made a major contribution to the understanding of the phenomenology of the oxidation reaction by demonstrating the regression of oxidic scales under steam-depleted conditions. They are also important for the validation of isothermal integral models.

Further experiments have been undertaken to investigate isothermal chemical dissolution processes, including the dissolution of oxidized cladding tube surfaces or the dissolution of nuclear fuel by melting cladding materials. Such processes are investigated in special crucible geometries in which a crucible is formed from oxidic material and metal is melted in its depression. These kinds of experiments have been conducted by Atomic Energy of Canada Limited (AECL) [20] and FZKA [25]. Due to the difficulties associated with the experimental conditions and the measurements, both studies are associated with significant uncertainty in terms of their results, particularly in terms of the temperatures that were set. In addition, these experiments are affected by multidimensional effects, which means that they have low reproducibility overall.

Compared to the isothermal case, significantly fewer experiments have been performed under the influence of temperature transients. In this context, cladding tube oxidation experiments with simultaneous heating of the samples or heat-up of the environments stand out since their execution is similar to their isothermal counterparts. Iglesias et al. [34] investigated the oxidation of zirconium samples in a temperature range from 1000 °C to 1700 °C under the influence of heating rates ranging from $1.5\,K/s$ to $100\,K/s$. However, their publication contained a low number of measurement points. Similar work was undertaken by researchers at FZKA [20] who used cladding tube samples, including a ZrO_2 pellet dummy. The investigations started at 1400 °C and were continued to the onset of melting processes. However, the data points from these measurements were also limited, which means that there is, in general, no usability for the validation of new oxidation models.

Data on temperature transient oxidation experiments without temperature constraints are rare. The experimental design of these experiments is as follows. In the first phase, the sample is heated up in an environment consisting of inert gas. When the sample reaches a thermally stable state, steam is injected. In this second phase, measurements keep track of the sample's temperature, while the ambient conditions are kept constant. Of all the separate-effect experiments mentioned above, this is the only experimental setup that allows conclusions to be drawn about the self-heating of a sample and, therefore, the released chemical reaction heat. Although this is the most interesting experimental setup, it is also the configuration with the lowest data available. In this context, only a single data set from Moalem and Olander [18] is known, in which a zirconium sample was oxidized (chip geometry). This experiment was started at a temperature of 1600 °C and shows a self-heating of the sample up to a temperature of approximately 1800 °C. A noticeable saddle point in the temperature data indicates that the melting point was reached before the temperature decreased again. Since there is only a single data set available, the outcome of the experiment cannot be assessed appropriately, which means that its data is again unsuitable for model tests.

A large body of experimental data originates from so-called integral tests, such as the QUENCH experiments that were conducted at FZKA. In such experiments, specific structures of reactor cores are simulated (bundle experiments) and correspondingly large geometries are used. The aim of these investigations is to obtain information about the degradation of the structures in certain accident sequences. For this purpose, a sequence of changing environmental conditions is simulated experimentally. Although these investigations provide excellent data regarding the bundle's temperatures, they offer little insight into the local progress of oxidation reactions. The large geometries are disadvantageous as they favor heterogeneous environmental conditions, spatial temperature profiles, and steam availability. Furthermore, the validation of a model with such data is only possible as part of a larger code package, which also contains thermo-hydraulic and structure-mechanical models. With the higher complexity, however, the susceptibility to undetected model errors increases, as errors can be amplified or compensated by the other physical models. Therefore, their data is also unsuitable for the validation of an advanced oxidation model at an early development stage.

Another large group of experiments is dedicated to the investigation of zirconium-containing melts flowing into water reservoirs, where the material oxidizes and solidifies within seconds (e.g., the FARO L-11 experiment [35] or the MISTEE-OX experiments [36]). In these experiments, the extent of the oxidation is largely determined by mechanical forces so that the layered structure of phases in the solidified melts differs significantly from structures, which evolve under the influence of dominant diffusion processes. Hence, these experiments are also unsuitable for the desired model tests within the framework of this work.

In summary, it can be stated that there are plenty of data elucidating isothermal processes. However, the existing experimental databases that are suitable for the testing, verification, and validation of advanced steam oxidation models, which are dedicated to the simulation of temperature transient processes, is extremely limited. In this context, only lone datasets are available, which provide little indication regarding the quality (repeatability) of the results. This situation is further aggravated by the fact that the models developed in the course of this work are limited to temperatures greater than $1500\,^{\circ}\mathrm{C}$ ($1773\,K$). The explanation for this limitation is given in Chapter 4. Hence, the comparison of the models developed in the framework of this thesis to other numerical models in order to assess their capabilities is without alternative.

3.4. Aim of the work

The aim of this work can be specified based on the description of the phenomenology of the high-temperature oxidation of zirconium in steam-containing environments (Chapter 2), the review of the state of the art regarding the modeling of the reaction in severe accident analysis codes (Section 3.1 and Section 3.2), and the summary of the experimental data available from the literature (Section 3.3).

The overall aim of this work is the development of a modern modeling approach for the simulation of the high-temperature oxidation of zirconium and steam in severe accident analysis codes. This model should overcome the limitations of the models used in this context today, which are based on parabolic rate approaches. At the same time, this new model has to guarantee an unchanged fast execution of the codes and must fit into their existing methodology and structure. Exceeding the capabilities of the existing integral models, this new model should be able to capture chemical reactions as coupled heat and mass transport problems, including temperature-related phase changes. To achieve this aim, various objectives and milestones must be reached.

The first objective is to provide a consistent description of thermodynamic states, which combines the information of a binary phase diagram with the urgently needed information about the enthalpy differences of different thermodynamic states. Inspired by the coupling of an isothermal integral model to the thermodynamic tool GEMINI in the mechanistic code ICARE, a quickly accessible lookup table is to be developed using IRSN's software NucleaToolbox (Chapter 4).

Any numerical model that provides a solution to both Fick's second law and the heat equation requires access to various material and transport properties. Therefore, a material library must be developed that provides these parameters for each phase occurring in the Zr-O system (Chapter 5).

Since integral models combine physical precision with reasonable numerical effort, an isothermal integral model is chosen as a starting point for the development of an advanced approach. Hence, this model is to be successively extended in such a way that it can model the coupled heat and mass transport problem (Chapter 6).

To examine the proposed advanced integral model's capabilities in detail, a model based on a spatially discretized approach is to be developed. This objective is based on two motives: first, such a model compensates for the limited availability of experimental data suitable for validation; and second, the model serves the interest of showing the differences between an integral model and a numerically expensive approach, which is unsuitable for implementation into severe accident analysis codes (Chapter 7).

As another objective, both models are to be verified in order to guarantee the high quality of their implementation (Chapter 8).

It must also be shown that the proposed advanced integral model meets the capabilities of state-of-the-art modeling approaches. Therefore, it is necessary to compare it directly to models from the literature, as well as models that are implemented into severe accident analysis codes (e.g., ATHLET-CD). In the course of these actions, differences in the solutions of the various models are identified and advances that have been made in the course of this work are demonstrated (Chapter 9).

The last and most important objective regarding the model tests is to demonstrate the advanced integral model's ability to reproduce complex coupled heat and mass transport problems that include both chemically- and thermally-induced phase transformations, which lie outside the scope of existing oxidation models (beyond state-of-the-art application). Due to the lack of experimental data, the spatially discretized model is to be used to pre-calculate representative transients. In turn, it is to be determined whether the advanced integral model can correctly reproduce these results (Chapter 10).

4. Thermodynamic lookup table

To describe the high-temperature oxidation of zirconium in steam, it is necessary to establish a linkage between the mass transfer processes, their related heat effects, and the heat transfer processes. That linkage can be achieved by a physically consistent description of thermodynamic states, which unifies the information about phase equilibrium concentrations with the related enthalpy differences of other thermodynamic states. Such complex information can be provided with the help of a lookup table that is generated with the aid of a thermodynamic computer code, such as IRSN's NucleaToolbox, which applies the so-called («Calculation of Phase Diagrams» (CALPHAD) method.

Due to the CALPHAD method's critical importance for the further understanding of the methods applied in this work, this chapter briefly introduces the method and explains its use of a Standard Element Reference (SER) in order to generate a set of physically self-consistent thermodynamic data. Subsequently, it introduces the thermodynamic software tool NucleaToolbox and the NUCLEA database, and explains the advantage of using a lookup table over a direct coupling of oxidation model and thermodynamic computer code. In the following, the concept, the development, and the structure of the lookup table that was developed and used in the work are described. In this context, special challenges regarding its information content, its limitations, and its use are explained. Thereafter, information about the phase equilibrium concentrations that are stored in the lookup table is compared to binary phase diagrams from the literature. Finally, the advantages of using of self-consistent data for the coupling of heat and mass transfer problems are explained using an example.

4.1. CALPHAD method, NUCLEA database, and NucleaToolbox

Introduction to the CALPHAD method

This section offers a brief outline of the CALPHAD method. For a comprehensive presentation, reference is made to the work of Saunders and Miodownik [37].

The second law of thermodynamics addresses questions of the irreversibility and the direction of thermodynamic processes, and it entails the necessity for the introduction of the entropy S. It states that the equilibrium state of an isolated system, which contains a constant amount of internal energy U, is accompanied by a maximum of its entropy . The assumption of a constant entropy S leads, in turn, to the minimum principle of the internal energy for closed systems in thermal equilibrium and, via a Legendre transformation, the minimum principle of the Gibbs free energy G.

Like the internal energy $U(S, V, \{N_c\})$, the Gibbs free energy $G(T, p, \{N_c\})$ is a thermodynamic potential that unambiguously describes the thermodynamic state of a system. However, its natural variables – the pressure p, temperature T, and number of particles N_c of different chemical components c – come along with substantial simplifications in search of equilibrium states. This becomes clear when its total differential dG is considered:

$$dG = -SdT + Vdp + \sum_{c=1}^{n} \mu_c dN_c, \text{ with } c = 1, ..., n \text{ and } \sum_{c=1}^{n} N_c = const.$$

$$\text{with } \mu_c = \left(\frac{\partial G}{\partial N_c}\right)_{p,T} \tag{4.1}$$

In Eq. 4.1, μ_c is the chemical potential that is dependent on the temperature T, pressure p, and number of particles N_c, which can also be expressed in terms of the molar oxygen fraction x_c.

Full thermodynamic equilibrium of a closed system comprises thermal, mechanical, and chemical equilibrium. Applying isothermic and isobaric conditions, the first two terms in Eq. 4.1 disappear, which indicates that changes in the Gibbs free energy result from chemical contributions only. Consequently, the Gibbs free energy of a given system is solely a function of the mole fractions of its constituents $G(x_c)$. Provided that the material system shows the ability to form different phases, an expression for the Gibbs free energy can be derived for each phase j. Since these phases compete for their manifestation, the only phases that will form are those that support the system's striving for the minimization of its total Gibbs free energy. This physical effect is used to compute phase equilibria for given temperatures T and pressures p in a material system consisting of known constituents $\{N_c\}$. Accordingly, computer codes that apply this principle are commonly called «Gibbs minimizers».

The required thermodynamic functions of the Gibbs free energy are derived from evaluated experimental data, estimates, and theory. These are compressed into complex mathematical models that emulate the observed behaviors of the phases. These equations, in turn, are summarized in thermodynamic databases. Details about their formulation are omitted here, but reference is made to Dantzig and Rappaz [38], who give an elaborate introduction into this approach, and Saunders and Miodownik [37], who draw up detailed modeling options for different phases and material systems.

Origin of Energies

Calculating the Gibbs free energies of a given system in various equilibrium states offers the possibility to quantify the energy differences (e.g., resulting from chemical reactions) as long as the data are self-consistent. This is possible because changes in state quantities as the Gibbs free energy $G(T, p, \{N_c\})$ or the enthalpy $H(S, p, \{N_c\})$ are independent of the path. As described in, for example, Dinsdale [39], the CALPHAD method uses an SER, which compensates for the lack of an absolute definition of energies. This reference builds on the fact that the Gibbs free energy can be divided into an enthalpic and an entropic part.

$$G = H - TS \tag{4.2}$$

The enthalpic part is defined as the most stable phase of the pure chemical element at $298.15\,K$ and $1\,bar$. In the case of the Zr-O system, this reference state H_{SER} is oxygen-free β-Zr at $298.15\,K$. The entropic part is usually nullified at $298.15\,K$ or, harnessing the third law of thermodynamics, at absolute zero ($0\,K$).

$$G_{H_{SER}} = (H - H_{SER}) + TS \tag{4.3}$$

The Gibbs free energy G, however, is an unsuitable thermodynamic variable in the context of the modeling of coupled heat and mass transfer. This is because it is defined as the capacity to do non-mechanical work. Therefore, enthalpy H is usually used in the context of engineering, which is understood as the capacity to do non-mechanical work plus the capacity to release heat. Starting from the Gibbs free energy, the enthalpy referred to in the SER can be calculated.

$$H_{H_{SER}} = G_{H_{SER}} + TS \tag{4.4}$$

The practical use of the Standard Element Reference is as follows. Enthalpy differences between equilibrium states can be calculated directly from the given data since the origins of the states cancel out. This works irrespectively of whether enthalpy differences are caused by thermal or chemical contributions.[1] Hence, the CALPHAD method makes it is possible to generate a self-consistent dataset (e.g., in the form of a lookup table) that comprises various equilibrium states, each defined by the triple of a mole fraction x_c, a temperature T, and, most importantly, an enthalpy H. Consequently, intricate models emulating thermodynamic relations based on cumbersome equations with limited applicability, as described in Section 3.2 or Appendix B, are rendered obsolete.

NUCLEA database and NucleaToolbox

The use of a self-consistent thermodynamic lookup table is a central element of the approach presented in this work. For its development, the thermodynamic database NUCLEA was used. NUCLEA was developed by Scientific Group Thermodata Europe (SGTE), a joint project of 13 European member organizations under the leadership of Thermodata, a French non-profit association closely linked to the Institut National Polytechnique Grenoble (INPG) and the Centre National de la Recherche Scientifique (CNRS).

NUCLEA was specifically designed to provide thermodynamic data for in- and ex-vessel applications. In version 15.4, it comprises 14 chemical elements that are the major components of fuel rods (U, Zr, O), control rods and blades (Ag, In, B, C), internal core structures and the pressure vessels (Fe, Cr, Ni), and concrete (Si, Mg, Al, Ca). In addition, data for two gases (Ar, H) and four fission products (Ba, La, Ru, Sr) are included [40]. The experimental data concerning the Zr-O system that are available from the literature, as well as their critical assessment, interpretation, and translation into expressions of the Gibbs energy embedded into the NUCLEA database, can be found in Chevalier and Fischer [9] and Chevalier et al. [10]. Important in this context is again the fact that there is no discrimination between pure zirconium and its various alloys in the selection of experimental references for the database (see Section 2.1).

To exploit the merits of the CALPHAD method and, hence, to calculate thermodynamic equilibria of the Zr-O system, the software NucleaToolbox (version 1.3) was used, which was developed by IRSN. For a given set of material composition, temperature, and pressure, NucleaToolbox calculates, among other issues, the phases present, their molar fractions, the phase compositions in terms of atoms (and species), and the enthalpy referred to in the SER.

---

[1] Mechanical contributions are neglected in general since mechanical equilibrium is assumed throughout this work.

4.2. Development of the lookup table

A computer model that describes transport processes in a system in thermal and chemical non-equilibrium, which is constantly undergoing concentration and temperature changes, requires an update of its thermodynamic data in each time step. However, already the computation of a single thermodynamic equilibrium is numerically expensive and takes several seconds if the software is executed on a modern desktop computer. Hence, the direct coupling of a severe accident analysis code and thermodynamic software would result in a significant slowdown of the code, thereby compromising its capability to execute simulations comprising various physical processes in real-time. To avoid this negative effect, it is expedient to pre-calculate the thermodynamic data for a given material system and the temperature range of interest and to store it in a lookup table. Using this method, the required information can be extracted by means of much faster interpolation algorithms during the execution of the oxidation model.

The lookup table used in the following chapters contains the extensive data of 14241 thermodynamic equilibria of the binary Zr-O system. The data were calculated via the variation of the molar oxygen fraction x_O from $0\,\%$ (pure zirconium) to $100\,\%$ (pure oxygen) in steps of $1\,\%$ and with the help of a temperature grid ranging from $498.15\,K$ to $3998.15\,K$ in steps of $25\,K$. In all calculations, the pressure was set constantly to $1\,bar$. Fig. 4.1 illustrates the grid points of the lookup table plotted over the temperature T against the relative molar oxygen fraction x_O. The color code of Fig. 4.1 gives a first, raw impression of the stability regions of the different phases, the resolution of which is further increased in the following.

The standard output from NucleaToolbox was condensed into a machine-readable lookup table that enables the use of quick search and interpolation algorithms. For each data point, the lookup table contains information regarding:

- The phases present (e.g., liquid (L) and γ-ZrO_2)
- Each phase's molar fraction (e.g., %-liquid and %-γ-ZrO_2)
- Each phase's compositions in terms of atoms (in %-O and %-Zr)
- Each phase's compositions in terms of chemical species (e.g., in %-Zr and %-ZrO_2)

- The enthalpy referred to in the Standard Element Reference ($H_{H_{SER}}$)
- The specific heat capacity at a constant pressure (c_p)

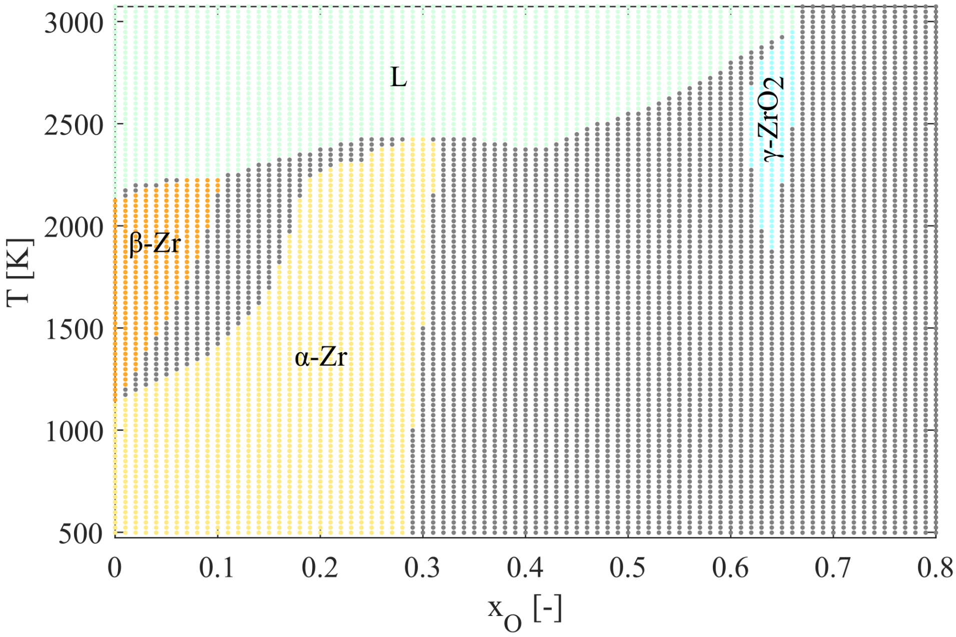

Figure 4.1.: Illustration of the grid points of the lookup table (Zr-O system). Gray dots indicate two-phase equilibria.

Binary phase diagram

A visualization of the data that resembles typical binary phase diagrams can be acquired as follows. The dataset of a two-phase equilibrium state (Fig. 4.1: grey dots) includes the individual compositions (Zr and O) of both contributing phases that are connected by a tie line belonging to an isotherm. On this tie line, the compositions of the contributing phases remain fixed, while the phase fractions are subject to changes governed by the lever rule. Thus, a phase is reliably detected if it appears at a minimum of one grid point. Summarizing this information for every temperature step unveils the lines of two-phase coexistence in high resolution, as illustrated in Fig. 4.2.

For the sake of completeness, it should be pointed out that numerically calculated equilibria that lay along the same tie line do not collapse to the exact identical saturation limits, but are slightly disturbed. Hence, the raw data must be filtered in the processing to avoid numerical instabilities of the oxidation models in which the data are to be employed later. Moreover, the use of a lookup table is intrinsically associated with a certain degree of information loss. This can be best understood if the dimension of the oxygen molar fraction and the dimension of temperature of the phase diagram are considered separately.

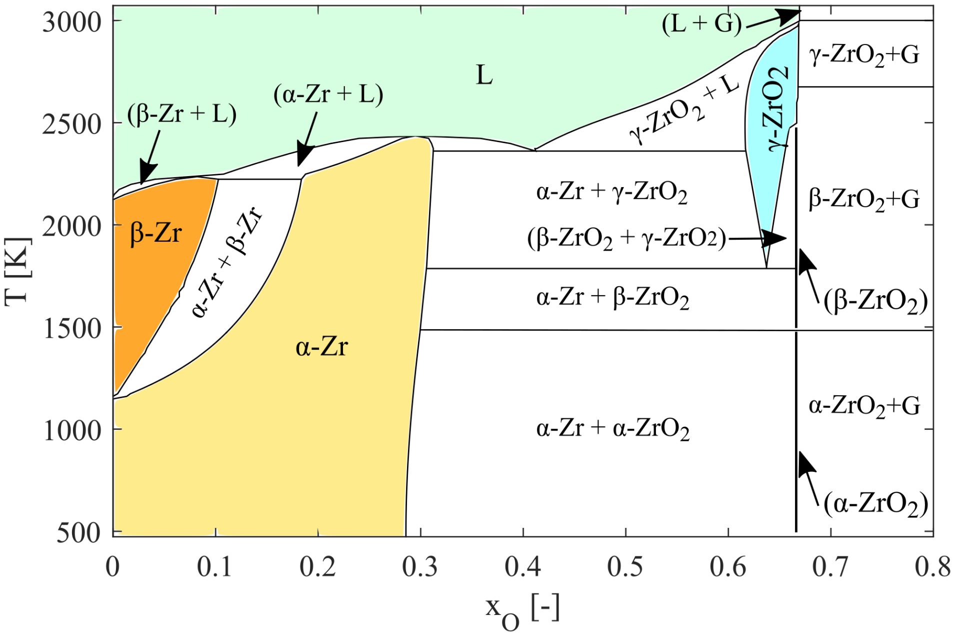

Figure 4.2.: Zr-O binary phase diagram as reconstructed from data from the thermodynamic lookup table.

Considering an isotherm in the phase diagram, it cannot be excluded completely that a two-phase region is not detected because both its left and right boundary lay between two neighboring grid points of different oxygen molar fractions. In that case, the only information retrievable is that a phase transition is located in between both. Experience shows that the probability that this error occurs is comparatively low, particularly because two-phase regions commonly span over a few percent of oxygen molar fraction, and are thus detected at several grid points. Nevertheless, such effects do occur, especially in those regions of the binary phase diagram in which two-phase regions narrow and ultimately vanish.

Considering now the oxygen molar fractions fixed, there exists no feature similar to the tie lines that can be used to complete the phase diagram in between two points of the temperature grid. In other words, the raw data charted in Fig. 4.1 contains no information about invariant points such as the melting point of pure β-Zr at $2123\,K$ or the eutectic point of α-Zr, γ-ZrO$_2$ and liquid (L) at $2338\,K$. In this context, it is virtually ruled out that the temperature grid catches any of these characteristics of the binary solution by chance. Thus, applying closer meshes can only narrow down the location of invariant points, but will not succeed in pinpointing their exact locations.

To overcome this issue, an algorithm has been developed that searches for phases that appear or disappear from one step of the temperature grid to another. If such an event is found, the algorithm inserts an intermediate subgrid point into the temperature grid, which is shifted by $12.5\,K$ relative to the regular grid. There, the arithmetic mean of the two molar fractions that are known from last tie line is inserted as an auxiliary value. Fig. 4.2 already contains these supplementary interpolated points.

Comparison with phase diagrams from the literature

The use of numerically generated data, which is furthermore completed by auxiliary data points, naturally raises the question of its conformity with data from the literature and, therefore, its reliability in general. Hence, in a first step, Fig. 4.3 compares the data of the lookup table to selected binary phase diagrams of the Zr-O system from the literature, the use of which is widely accepted. Those are the state diagrams of the following authors:

1. Abriata, Garcés, and Versaci (1986) [1], which is the main one used today
2. Elliot (1965) [41], which is frequently cited in older publications (e.g., Urbanic and Heidric [28])
3. Leistikow, Schanz, and Berg (1978) [42], which is predominantly used in German specialist literature

It should be noted that the experimental data underlying the aforementioned phase diagrams and the data describing the Zr-O system in general are relatively old, but they are the only available data. A comprehensive overview on this topic is given in [1]. Since all diagrams are nevertheless still used today, time is taken to describe their differences in the following.

Fig. 4.3 shows that the binary phase diagram of Elliot [41] and the diagram of Leistikow et al. [42] largely agree, yet they show significant differences compared to the diagram of Abriata et al. [1]. Particularly striking is the deviation in position of the eutectic point of α-Zr, γ-ZrO$_2$, and liquid (L) that is minor in oxygen molar fraction but approximately $165\,K$ in temperature. The same applies to the melting temperature of α-Zr, which is significantly lower in the diagrams of Elliot [41] and Leistikow et al. [42] compared to the work of Abriata et al. [1]. Another important finding is the differences in the slopes of the solidus line of γ-ZrO$_2$, which can have drastic effects in the context of the modeling of diffusion-based mass transfer processes.[2] Therefore, it is obvious that simulations with diffusion models lead to different results depending on the chosen phase diagram.

Both Elliot [41] and Abriata et al. [1] stated that parts of their diagrams have yet to be reliably determined by experimental work. The probable yet uncertain parts of their

---

[2] Depending on the chosen phase diagram, a temperature increase above the eutectic point in one case would result in an amplification of the concentration gradient and enforce the oxidation reaction, in the other case resulting in its reduction.

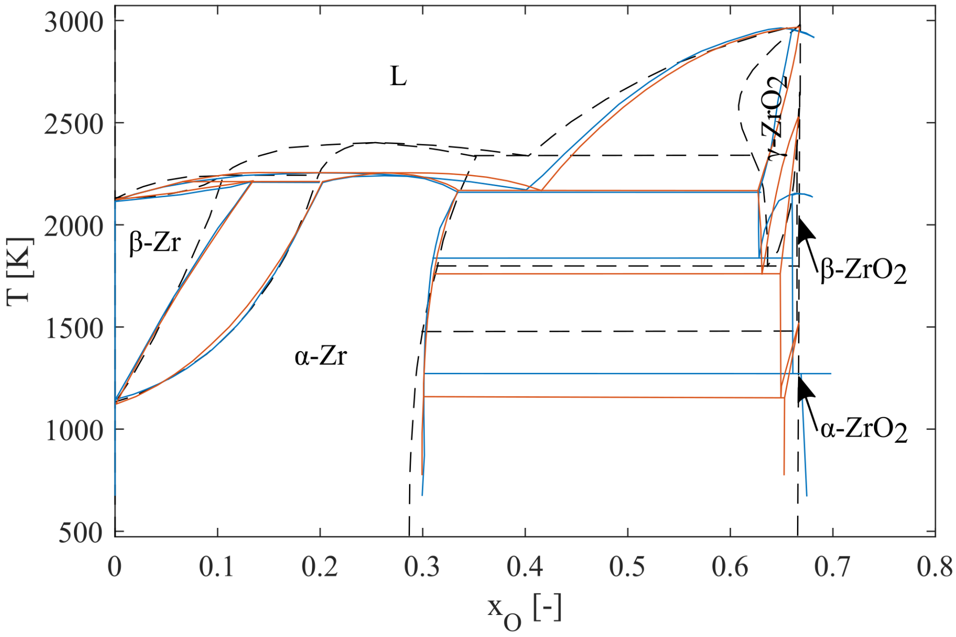

Figure 4.3.: Zr-O binary phase diagrams from the literature in direct comparison: Abriata et al. [1] (dashed lines), Elliot [41] (red lines), and Leistikow et al. [42] (blue lines).

diagrams are mainly the temperatures of the allotropic transitions and the substoichiometry or hypostoichiometry of ZrO_2. The eutectic point and the gradient of the liquidus slope could already been determined experimentally at the time Abriata et al. developed their phase diagram and is thus an advantage of their work. Therefore, their phase diagram is used as a reference in the following comparison with the diagram derived with the aid of the NUCLEA database and NucleaToolbox. The comparison of both diagrams is shown in Fig. 4.4.

The diagram derived in the course of this work shows the following differences, which are mentioned in the order of low to high oxygen molar fractions. The peritectic transition of α-Zr, β-Zr, and liquid (L) is slightly shifted to lower oxygen molar fractions. The slope of the left-hand-side line of two-phase coexistence of α-Zr is flatter, whereas its right-hand-side line of two-phase coexistence is steeper. The maximum of the melting point of α-Zr is shifted to higher oxygen molar fractions. According to the calculated data, both α-ZrO_2 and β-ZrO_2 only exist in their perfect stoichiometry in phase equilibrium for temperatures of less than 1525 °C. Since a diffusion-based approach calls for the existence of hypostoichiometric ZrO_{2-X}, the range of applicability of the lookup table had to be limited to a temperature range between 1525 °C and 3725 °C. Furthermore, the liquidus line of the two-phase region between liquid (L) and γ-ZrO_2 shows a significantly flatter gradient.

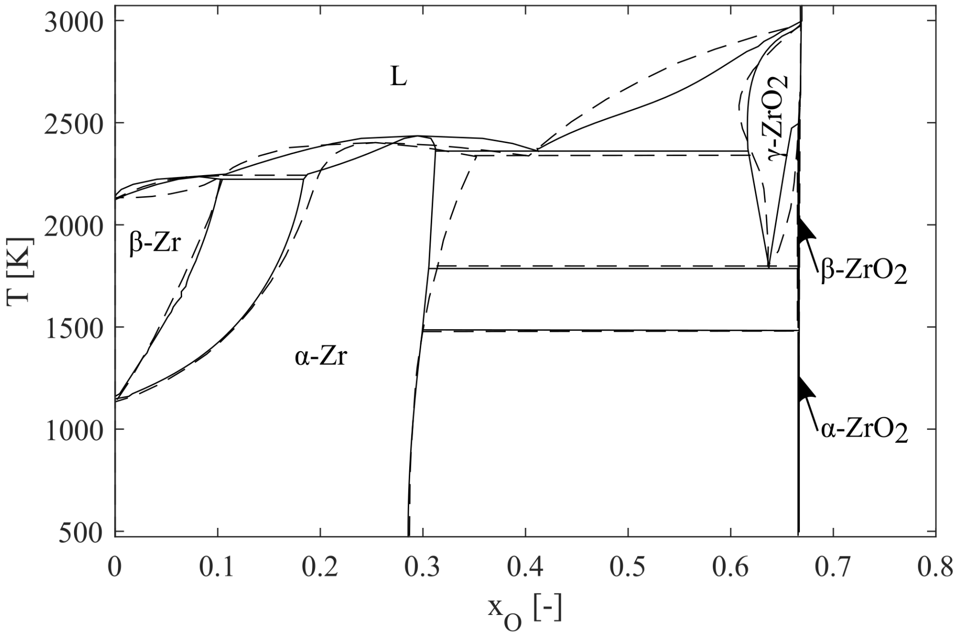

Figure 4.4.: Zr-O binary phase diagram developed in this work (solid line) compared to the diagram of Abriata et al. [1] (dashed line).

As explained in the previous section, it is necessary to restore thermodynamic data of invariant points that are not captured by the orderly grid of the lookup table with an additional interpolation algorithm. Due to this procedure, invariant points can be slightly displaced. Against this background, differences compared to the phase diagram of Abriata et al. have been systematically investigated. The results of this investigation are given in Table 4.1.

Table 4.1.: Comparison of invariant points in the Zr-O binary system as they are indicated by the lookup table and the phase diagram of Abriata et al. [1].

	Abriata et al.		**Lookup table**	
Invariant point	x_O [%]	T [K]	x_O [%]	T [K]
α-Zr, melting	25.0±1.0	2403±10	29.5	2436
β-Zr, melting	0.0	2128	0.0	2123
γ-ZrO$_2$, melting	66.7	2983	66.9	2986
α-Zr+β-Zr+L, peritectic	10.5±0.5	2243±10	10.3	2236
α-Zr+β-ZrO$_2$+γ-ZrO$_2$, eutectoid	63.5	~1798	63.7	1786
α-Zr+γ-ZrO$_2$+L, eutectic	40.0	2338±5	41.2	2361

The NUCLEA database comprises the latest development in the modeling of the thermodynamic data, and so it is the closest to a state-of-the-art representation of the Zr-O system. Nevertheless, a thorough examination indicates that its experimental background, as described in Chevalier and Fischer [9] and Chevalier et al. [10], largely matches the data used by Abriata et al. [1]. Therefore, the differences between the diagram from the literature and the one generated in the course of this work mainly arise from choice and the interpretation of experimental data by the developers of both thermodynamic tools.

x_O-T-h_m-diagram

This work uses thermodynamic data in form of a binary phase diagram not only to model the diffusive oxygen mass fluxes but also to describe the heat generation of the oxidation reaction. As described earlier, the data obtained using the CALPHAD method contain valuable information regarding the enthalpy difference between equilibrium states, which is physically self-consistent due to the concept of the Standard Element Reference.

Fig. 4.5 charts the enthalpy values belonging to each of the 14241 precalculated equilibria in the form of a x_O-T-h_m-diagram. Here, the oxygen molar fraction x_O and temperature T are defined by the input, while the molar enthalpy h_m is the result of the respective calculation.

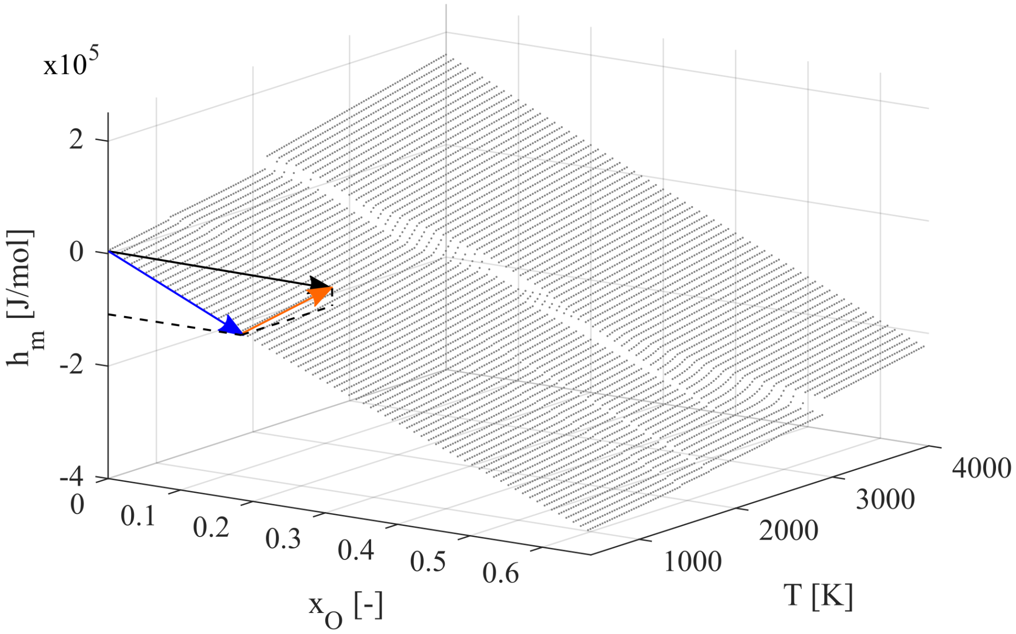

Figure 4.5.: Lookup table illustrated as x_O-T-h_m-diagram (arrows: see text).

The molar enthalpy of oxygen-free zirconium at $298.15\,K$ is set to $0\,\frac{J}{mol}$. Emanating from this point, the molar enthalpy increases with an increase in temperature since it implies a heat influx. The decrease of the molar enthalpy in the direction of the increasing oxygen concentration results from a reduced potential to enter chemical reactions compared to the reference state. Since the functional interrelation between oxygen molar fraction and molar enthalpy is less obvious, it is explained with the help of an example.

Fig. 4.5 assigns an enthalpy value to a system, which obtains a molar oxygen fraction of $0\,\%$ and corresponds to a temperature of $498.15\,K$. If this system's molar oxygen fraction is increased, the chemical reaction leads to the conversion of chemical energy into thermal energy. To maintain isothermal conditions, this thermal energy has to be removed from the system (blue arrow, in this example, from approx. $0\,\frac{J}{mol}$ to $-1 \cdot 10^5\,\frac{J}{mol}$). Assuming, by contrast, an isolated system, the reaction heat is retained and the system's temperature inevitably has to rise (orange arrow, here from $498.15\,K$ to approximately $1000\,K$) to maintain the enthalpy in equilibrium (black arrow, $0\,\frac{J}{mol}$ at $1000\,K$). Hence, the lookup table contains information about enthalpy changes between different equilibrium states irrespective of thermal and chemical contributions, which is of great importance and convenience for the coupling of the heat and mass transport problem presented in due course in this work.

x_O-T-h_m-diagram for separate phases

In a binary phase diagram, the different phases are separated by two-phase regions that are an expression of the differences in their stability limits regarding their oxygen molar fractions. When using self-consistent data that includes an enthalpy dimension, the enthalpy values of different phases show similar leaps. In analogy to the procedure described in the previous sections, it is possible to discriminate the molar enthalpy of each equilibrium state into the individual contributions of the coexisting phases (weighted by the lever rule). The obtained representation of the x_O-T-h_m-diagram strongly resembles the binary phase diagram with an additional enthalpy dimension (see Fig. 4.1).

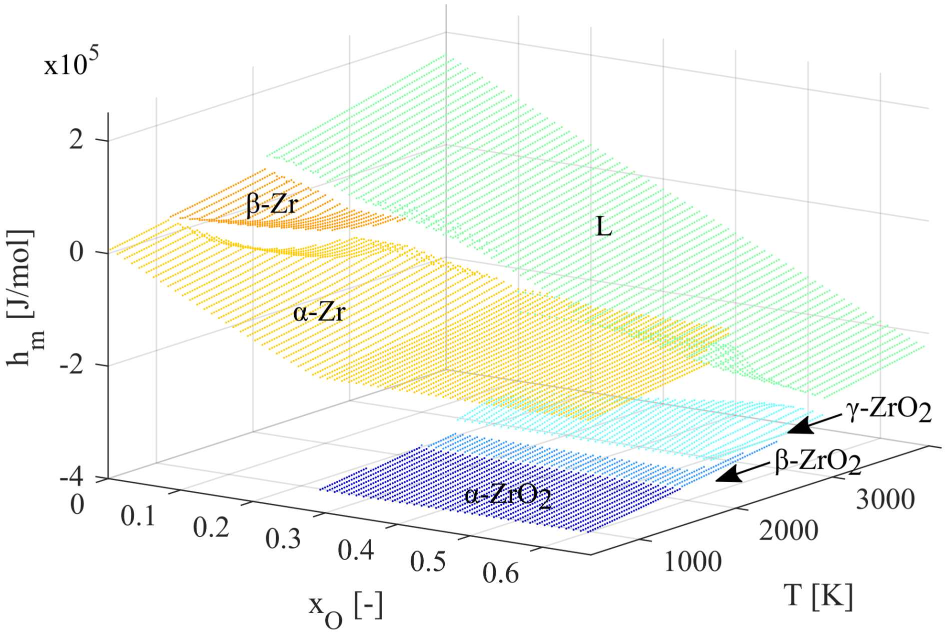

Figure 4.6.: x_O-T-h_m-diagram plotted in analogy to the logic of binary phase diagrams.

5. Material and transport properties library

The solution of a diffusion problem, assuming the validity of Fick's law and a heat conduction problem based on the heat equation, requires knowledge of different transport and material properties for various phases. These are the parabolic rate constants (k_{ox} and k_{τ}) as the data basis of the oxygen diffusion coefficients, the diffusion coefficients themselves (D_O), the thermal conductivities (λ), and the densities (ρ). With this in mind, it is the purpose of this chapter to summarize and merge such information in a library that can be coupled to the oxidation models that are developed in the subsequent chapters of this work.

The importance of a high-quality and uniform data basis for simulation codes was recognized early in the history of severe accident analysis codes. Thus, various scientific publications are devoted to the assessment of the availability, the comparison, and the recommendation of empirical correlations for the different required properties. Nonetheless, it can be stated that the information is more or less patchy. A differentiation of material and transport properties into the different allotropes usually does not take place, which means that thermal conductivities and densities, in particular, are usually just distinguished into «metallic zirconium», «oxidic zirconium dioxide», and their liquid counterparts. However, exceptions to this statement are the diffusion coefficients that are distinguished into the respective allotropes. The situation is further aggravated by the fact that it is often unclear which of the various zirconium alloys has been used in an experiment for the determination of a correlation. Temperature dependencies are mostly given, although the availability and reliability of the correlations decreases with an increase in temperature. This results in an overall lack of detailed information regarding the liquid phase, the properties of which are often only given for the melting point. Concentration dependencies of the individual properties are usually not considered at all.

5.1. Parabolic rate constants

Parabolic rate constants are derived from experiments conducted under isothermal conditions with initially oxygen-free samples in the form of chips or cladding tube pieces that are exposed to steam. The temporal progression of the oxidation is determined by either gravimetric methods, with measurements of the hydrogen generation, or by metallographical analyses, which require multiple repetitions of the experiments.

The rate constants are provided in the form of Arrhenius equations, which are valid for the isothermal oxidation of certain base materials in specific temperature ranges:

$$k = \tilde{A} exp\left(-\frac{E}{RT}\right) \tag{5.1}$$

where A is a pre-exponential factor, E the activation energy for the reaction, R the universal gas constant, and T is the absolute temperature.

Alhough one would expect a certain degree of consistency between the obtained correlations, rate constants differ significantly from one author to the other. In this light, Schanz [5] stated that the large variety of rate constants favors their misuse in order to compensate for other model errors of severe accident analysis codes. Therefore, Schanz recommends the use of a uniform set of equations within the community until new models become available. The constants recommended by Schanz, and which are most frequently used in severe accident analysis codes, are those of Baker and Just [26], Urbanic and Heidrick [28], Pawel, Cathcart, and McKee [29], and Prater and Courtright [27].

Table 5.1 presents the correlations of these authors for mass gain k_τ and oxide layer growth k_{ox}, together with their range of application as recommended by Schanz [5]. The information in this table is also vividly illustrated in Figs. 5.1 and 5.2.

Table 5.1.: Correlations for the estimation of parabolic rate constants by different authors.

Author	k_τ in $[\frac{g}{cm^2\sqrt{s}}]$	$k_{ox.}$ in $[\frac{cm}{\sqrt{s}}]$	Temperature range
Baker and Just [26]	$5.77exp\left(-\frac{22898}{T}\right)$	–	$1273\,K - 2123\,K$
Urbanic and Heidrick [28]	$0.172exp\left(-\frac{8410}{T}\right)$	$0.036exp\left(-\frac{6793}{T}\right)$	$1323\,K - 1853\,K$
	$0.296exp\left(-\frac{8305}{T}\right)$	$0.144exp\left(-\frac{8007}{T}\right)$	$1853\,K - 2123\,K$
Pawel et al. [29]	$0.601exp\left(-\frac{10050}{T}\right)$	$0.150exp\left(-\frac{9031}{T}\right)$	$1273\,K - 1773\,K$
Prater and Courtright [27]	$5.74exp\left(-\frac{13220}{T}\right)$	$5.46exp\left(-\frac{14210}{T}\right)$	$1783\,K - 2673\,K$

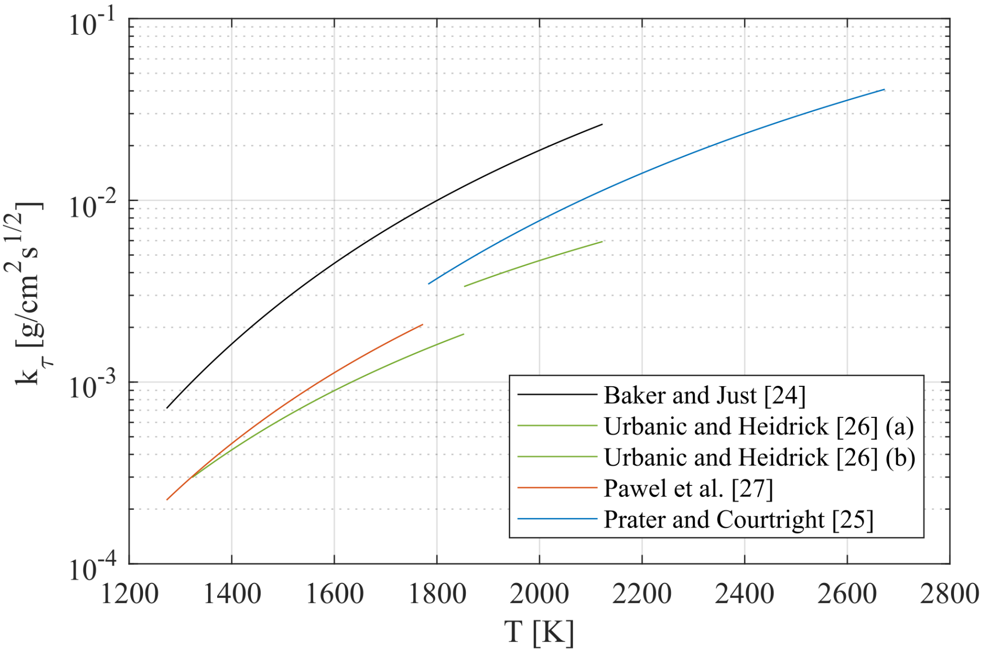

Figure 5.1.: Correlations for the estimation of the parabolic rate constant k_τ by different authors.

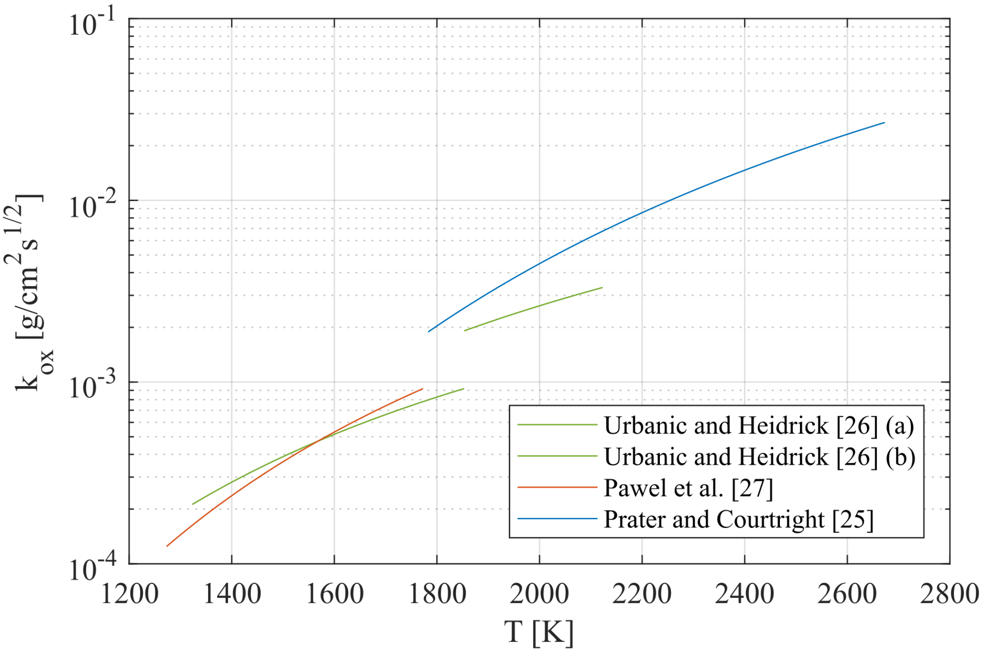

Figure 5.2.: Correlations for the estimation of the parabolic rate constant k_{ox} by different authors.

Rate constants for different alloys

A question regarding the transferability of the rate constants arises from the changes in the material composition of zirconium alloys that were used in the experiments (Zry-2 and Zry-4), their ongoing refinement, and the commercial introduction of new alloys (e.g., M5). In this context, it is a common assumption that most alloys show a similar kinetic oxidation behavior, which is reinforced by a statement of Urbanic and Heidrick in [28], who could not find significant differences between Zry-2 and Zry-4. Pawel, Cathcart, and McKee [29] reported significant deviations in the rate constants of up to 20 % already for material from different batches of the same manufacturer. Hence, the aforementioned assumption must be used with care.

5.2. Oxygen diffusion coefficients

Diffusion coefficients can be determined, for example, by examining oxygen concentration profiles along the diffusion path using microsections of samples and precise electron beam microanalysis. In analogy, a theoretical approach makes it possible to determine the diffusion coefficients of the Zr-O system from the known parabolic rate constants and phase equilibrium concentrations. A detailed mathematical description of such a theoretical approach can be found in Pawel [43] or Olander [6]. Temperature-dependent correlations for the determination of diffusion coefficients follow the same scheme as correlations for parabolic rate constants and are given as Arrhenius equations.

In this context, it should be noted that the possibility of varying the selected rate constants and phase diagrams, which can be used for the determination of diffusion coefficients, again has a negative influence on their uniformity, and that efforts for standardization have not yet been made (see Section 4.2). Besides, the availability of diffusion coefficients for oxygen in zirconium matrices is significantly lower and their quality more heterogeneous than the availability and quality of parabolic rate constants. Consequently, users of numerical models often prefer to determine their own diffusion coefficients in order to fit their simulation results to experimental references (see, for example, Hofmann et al. [25]), which is, at the very least, a questionable approach.

For these reasons, a selection of correlations for the determination of oxygen diffusion coefficients for different allotropes of different authors is given below. This information is divided into diffusion coefficients for α-Zr (Table 5.2), β-Zr (Table 5.3), β-ZrO_2 (Table 5.4), and duplex oxide (β-ZrO_2 and γ-ZrO_2, Table 5.5). As shown in Table 5.5, there is a significant lack of diffusion coefficients for temperatures higher than $2273\,K$ (or 2000 °C), which means that these data must be extrapolated in general. Graphs illustrating the temperature-dependent behavior of the oxygen diffusion coefficients for the metallic phases are summarized in Fig. 5.3, while graphs for the oxides are given in Figs. 5.4 and 5.5.

Table 5.2.: Correlations for the estimation of diffusion coefficients of oxygen in α-Zr by different authors.

Author	D_O in $[\frac{m^2}{s}]$	Temperature range
Iglesias et al. [34]	$4.11exp\left(-\frac{25682}{T}\right)\cdot 10^{-4}$	$923\,K - 1773\,K$
Pawel [43]	$3.92exp\left(-\frac{25667}{T}\right)\cdot 10^{-4}$	$1273\,K - 1773\,K$
Hofmann et al. [44]	$exp\left(0.21847-\frac{24526}{T}\right)\cdot 10^{-4}$	$1273\,K - 1973\,K$

Table 5.3.: Correlation for the estimation of diffusion coefficients of oxygen in β-Zr.

Author	D_O in $[\frac{m^2}{s}]$	Temperature range
Pawel et al. [45]	$0.0263exp\left(-\frac{28200}{T}\right)\cdot 10^{-4}$	$1273\,K - 1773\,K$

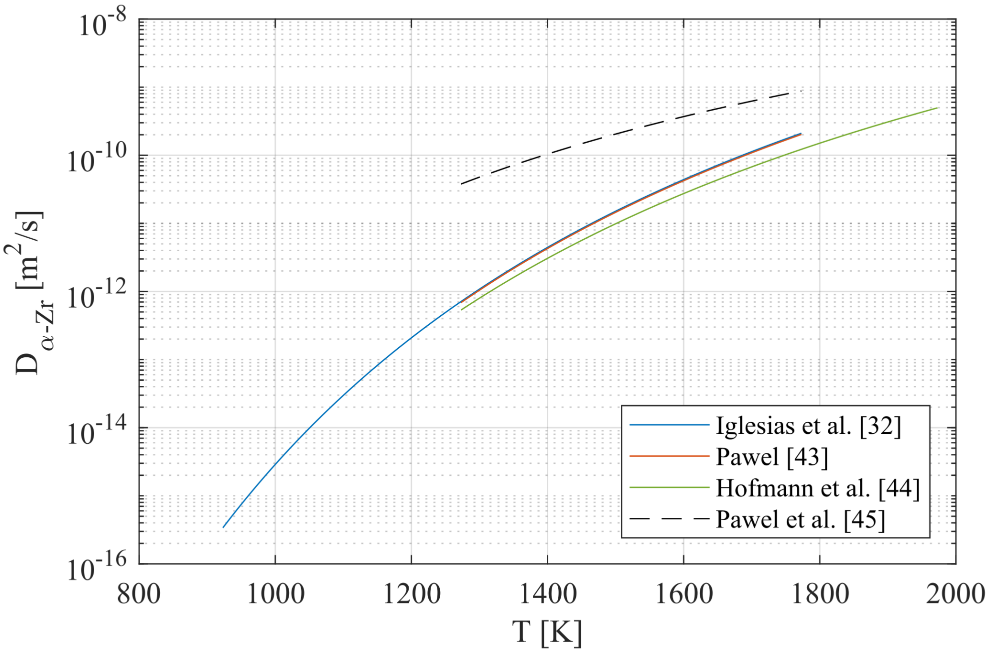

Figure 5.3.: Correlations for the estimation of diffusion coefficients of oxygen in metallic zirconium by different authors: solid lines α-Zr, dashed line β-Zr.

Table 5.4.: Correlations for the estimation of diffusion coefficients of oxygen in β-ZrO$_2$ by different authors.

Author	D_O in $[\frac{m^2}{s}]$	Temperature range
Iglesias et al. [34]	$0.157exp\left(-\frac{17685}{T}\right)\cdot 10^{-4}$	$1300\,K - 1773\,K$
Pawel [43]	$0.127exp\left(-\frac{17368}{T}\right)\cdot 10^{-4}$	$1273\,K - 1773\,K$
Olander [6]	$4.0exp\left(-\frac{19000}{T}\right)\cdot 10^{-4}$	$1273\,K - 1773\,K$
	$75.0exp\left(-\frac{22600}{T}\right)\cdot 10^{-4}$	$1273\,K - 1773\,K$

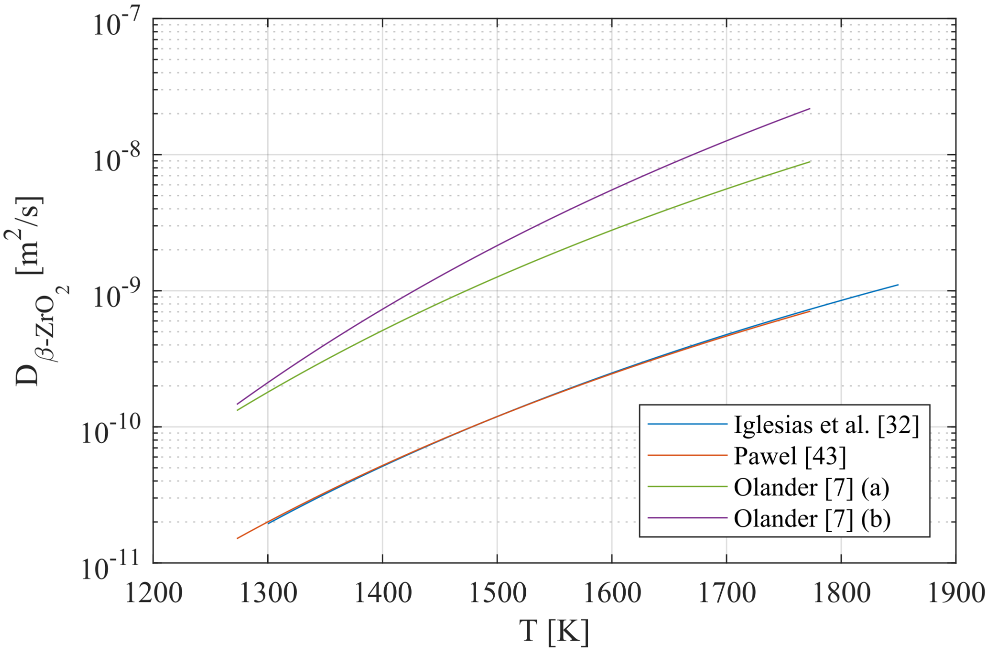

Figure 5.4.: Correlations for the estimation of diffusion coefficients of oxygen in β-ZrO$_2$ by different authors.

Oxygen diffusion in the liquid phase

The diffusion coefficients of the liquid phase represent a special case for which no experimental investigations are available. In this work, the diffusion coefficient of oxygen in the liquid phase is determined using the Stokes-Einstein equation, which assumes Brownian motion and applies to small Reynolds numbers (here, stationary liquid).

$$D_{liq} = \frac{k_B T}{6\pi\eta r} \tag{5.2}$$

Table 5.5.: Correlations for the estimation of diffusion coefficients of oxygen in dublex oxide (β-ZrO$_2$ and γ-ZrO$_2$) by different authors.

Author	D_O in $[\frac{m^2}{s}]$	Temperature range
Olander [6]	$0.09exp\left(-\frac{16000}{T}\right)\cdot 10^{-4}$	$1773\,K - 2273\,K$
Olander [6]	$120.0exp\left(-\frac{28400}{T}\right)\cdot 10^{-4}$	$1773\,K - 2273\,K$
Olander [6]	$20.0exp\left(-\frac{24000}{T}\right)\cdot 10^{-4}$	$1773\,K - 2273\,K$
Hofmann et al. [25]	$4.0exp\left(-\frac{24000}{T}\right)\cdot 10^{-4}$	$2273\,K - 2573\,K$
Hayward and George [20]	$1.3\cdot 10^{-9}$	$2273\,K$

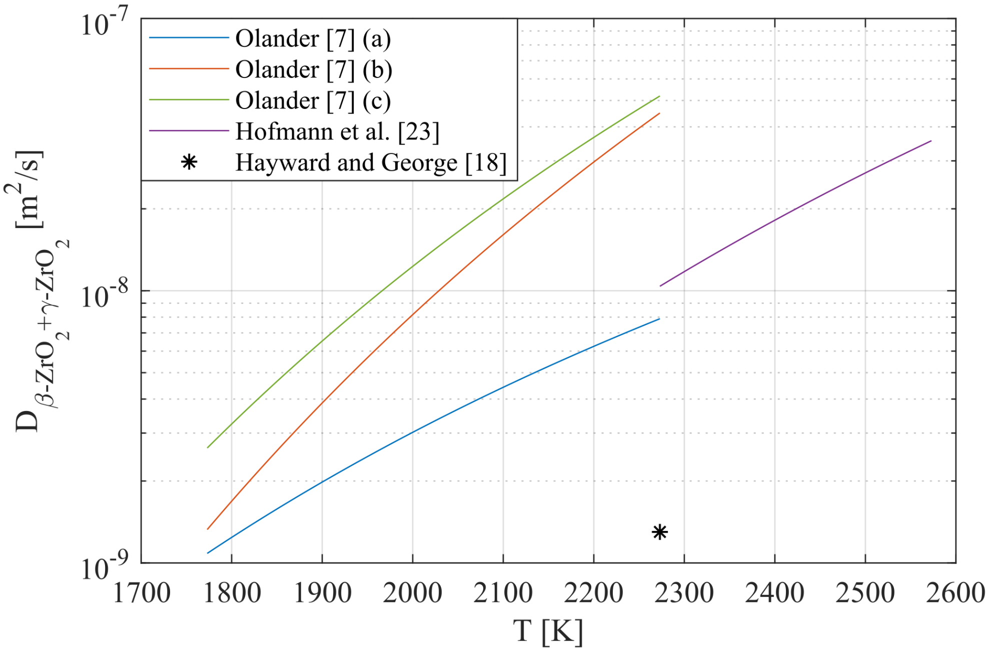

Figure 5.5.: Correlations for the estimation of diffusion coefficients of oxygen in dublex oxide (β-ZrO$_2$ and γ-ZrO$_2$) by different authors.

In Eq. 5.2, k_B is the Boltzmann constant, T the absolute temperature, η the dynamic viscosity, and r the ionic radius of the moving particle. Thus, this equation requires knowledge of the dynamic viscosities η of liquid zirconium and liquid zirconium dioxide.

The aforementioned reports of the International Atomic Energy Agency (IAEA) [22, 46] reduce the information about the viscosity of molten zircon to a constant value of

$8^{+2}_{-7}\,mPas/s$, which is associated with rather substantial uncertainty. This value was determined by Brunell and Prater in a temperature range from $2075\,K$ to $2175\,K$ [47]. Further experimental investigations of this property in a temperature range of $1800\,K$ to $2400\,K$ were published by Paradis et al. [48]. Using their correlation, very different values of $5.0\,mPa/s$ and $4.5\,mPa/s$ are obtained at $2075\,K$ to $2175\,K$.

To derive a value for the viscosity of molten zirconia at least at its melting point, Nazaré et al. [49] recommend an empirical equation by Andrade in [50].

$$\eta = C\frac{(T_{melt}M)^{1/2}}{V_m^{2/3}}\,\frac{mPa}{s} \tag{5.3}$$

In this context, T_{melt} is the melting temperature, M the molar mass, V_m the molar volume, and C a constant varying from one author to the other (Andare: $0.161 \cdot 10^{-6}$, Nazaré et al.: $0.194 \cdot 10^{-6}$). This equation can likewise be used to calculate the viscosity of liquid zirconium and liquid zirconia. Accordingly, the viscosities at the melting point of both metallic zirconium and oxidic zirconia can be estimated to be $4.1\,mPa/s$ and $4.2\,mPa/s$. Due to the qualitative agreement between these values and the viscosities provided by Paradis et al. [48], as well as the higher flexibility of the approach with regarding variable oxygen concentrations, the viscosities of Zr-O mixtures are calculated using the approach of Nazaré et al. [49] in this work.

5.3. Thermal conductivities

An equally comprehensive and detailed overview of the present knowledge on thermal conductivities (and other thermophysical quantities, such as densities) of the materials used in reactor applications was provided by the IAEA [22, 46]. Its reports are supplemented by the freely accessible materials database THERPRO, which summarizes the experimental data from the literature. The materials properties library MATPRO, which is part of the mechanistic computer code SCDAP-RELAP5, can also be understood as an evaluated source of information. Documents describing MATPRO have been published by the Office of Scientific and Technical Information of the United States Department of Energy (OSTI) and the United States Nuclear Regulatory Commission (NRC) [51].

The availability of correlations suitable for an estimation of the thermal conductivity of solid metallic zirconium is large. This stems from the fact that it is a crucial design parameter for fuel rods. A summary of a high number of different correlations for various zirconium alloys can be found in Kim et al. [46]. Consistent with the recommendation of Bobkov et al. [22], the following equation is used in this work:

$$\lambda_{Zr,sol.} = 8.8527 + 7.0820 \cdot 10^{-3}T + 2.5329 \cdot 10^{-6}T^2 + 2.9918 \cdot 10^3 T^{-1} \quad \left[\frac{W}{mK}\right] \tag{5.4}$$

There are by far fewer references available that provide a means to quantify the thermal conductivity of liquid zirconium. Hence, consistent with the recommendation of the aforementioned report [22], the following constant value is used in this work:

$$\lambda_{Zr,liq.} = 36.5 \, \frac{W}{mK} \tag{5.5}$$

In contrast, none of the reports of the IAEA [22, 46] provide a means to quantify the thermal conductivity of solid oxidic zirconium dioxide. Therefore, this work uses a correlation mentioned in the MATPRO manual [51]:

$$\lambda_{ZrO_2,sol.} = 0.835 + 1.81 \cdot 10^{-4}T \quad \left[\frac{W}{mK}\right] \tag{5.6}$$

Along the same lines, the value for the thermal conductivity of the liquid oxide is taken from MATPRO. Similar to the thermal conductivity of liquid metallic zirconium, this property can only be implemented as a constant. According to Siefken et al. [51] ,this constant is based on a correlation for the thermal conductivity of solid zirconium dioxide that is evaluated at its melting point:

$$\lambda_{ZrO_2,liq.} = 1.4 \, \frac{W}{mK} \tag{5.7}$$

5.4. Densities

Regarding the values and temperature dependencies of the required densities, the IAEA reports [22, 46] only provide information about solid metallic zirconium. This work follows their recommendation and uses the following correlation for the estimation of the density of solid zirconium, applying it independent of the respective allotrope:

$$\rho_{Zr,sol.} = 6550 - 0.1685T \quad \left[\frac{kg}{m^3}\right] \tag{5.8}$$

The density of liquid metallic zirconium in this work's materials library is taken from Wang et al. [52]. In their work, the authors compared their numerical estimations of the density with the experimental and numerical work of other groups. Due to the uncertainty of the data and the less developed temperature dependency of the density of liquid zirconium, its value is also set to a constant value in this work:

$$\rho_{Zr,liq.} = 6080\,\frac{kg}{m^3} \tag{5.9}$$

A correlation for the density of solid, oxidic zirconium dioxide is again adopted from MATPRO [51]:

$$\rho_{ZrO_2,sol.} = 5800\left(1 - 3\left(1.302 \cdot 10^{-5}T - 3.338 \cdot 10^{-2}\right)\right) \qquad \left[\frac{kg}{m^3}\right] \tag{5.10}$$

As in the case of the density of liquid zirconium, there is a significant lack of data describing the density of liquid oxidic zirconium dioxide. In this work, this information is taken from Kondo et al. [53], who provided a comprehensive overview of recent literature on this material property and, in this way, summarized both the experimental and numerical studies. Due to larger differences in the density values reported between different authors, and due to the minor reported temperature dependency of this property, only the density at the melting point is provided by this work's materials library:

$$\rho_{ZrO_2,liq.} = 4690\,\frac{kg}{m^3}; \tag{5.11}$$

Due to the lack of information, particularly regarding the densities of molten materials, the IAEA TECDOC-1496 [46] further recommends to set densities in temperature ranges in which temperature-resolved information is not available as constant, and to refrain from extrapolations. Since, moreover, the liquid phase rarely consists of pure liquid zirconium or pure liquid zirconium dioxide, but rather is a mixture, the density of the liquid phase is calculated using an ideal mixing rule that neglects excess volumes. This procedure is also recommended in the aforementioned TECDOC [46]:

$$\rho_{liq.} = \frac{\sum\limits_i y_i M_i}{\sum\limits_i y_i V_{m,i}} \tag{5.12}$$

where y_i denotes the atomic fraction of a species i (e.g., Zr and ZrO_2), M_i is the molar mass of that species i, and $V_{m,i}$ is its molar volume.

6. Advanced integral model

This work aims to develop a modern, fast-running modeling approach for the simulation of the high-temperature oxidation of zirconium in steam-containing environments for severe accident analysis codes. As described in Section 3.4, this model is to be based on an integral approach that must be extended by a suitable heat transfer model. The model is to be coupled to a thermodynamic lookup table (see Chapter 4) that provides self-consistent thermodynamic data in order to overcome the limitations of existing modeling approaches.

Hence, this work builds on the one-dimensional isothermal integral model described in Section 3.2. This chapter presents considerations leading to its extension to cover the heat transfer problem, thermally-induced phase changes, and the heat effects of the oxidation reaction itself. In this context, this chapter starts by introducing an integral model designed for the modeling of heat transfer problems in pure substances (unary systems). In turn, its applicability to a binary system is assessed, challenges are described, and viable solutions are presented. Once a suitable system of equations for the heat and mass transfer problem has been described, the coupling to the thermodynamic lookup table is explained, through which the model gains its ability to account for chemically-induced heat effects and temperature-related phase changes.

6.1. Heat transport

Modeling heat transport using an integral approach

Due to the strong analogy of Fick's second law of diffusion and the heat equation, it seems obvious to describe the heat transport as a moving boundary problem and to derive a heat transport model in analogy to the methodology presented in Section 3.2.

The moving boundary problem, which was formulated to derive mass balance approximations, entails the assumption of local thermodynamic equilibrium at the phase interfaces. This implies leaps in the spatial concentration profiles. Concerning heat transfer, a similar moving boundary problem can be set up, which in turn implies leaps in the enthalpy profile, while the temperature remains continuous. In both cases, the transition zones are assumed to be small and their mass is neglected. Fig. 6.1 illustrates these considerations.

$$\rho_{O}{}_{I}^{*} \neq \rho_{O}{}_{2}^{*}, \text{ at } x = x^{*}(t) \tag{6.1}$$

$$h_{I}^{*} \neq h_{II}^{*}, \text{ at } x = x^{*}(t) \tag{6.2}$$

$$T_{I}^{*} = T_{II}^{*}, \text{ at } x = x^{*}(t) \tag{6.3}$$

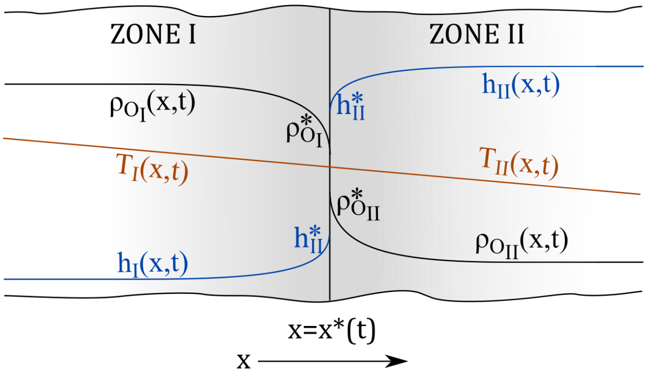

Figure 6.1.: Leaps in the concentration profile (isothermal system) and enthalpy profile (unary system) at the position of a phase interface.

Following this idea, a conservation equation is established for the bulk enthalpy $\overline{\rho h}$ of each zone z and an equation for the movement of the phase interface v_Γ due to the imbalance of the heat fluxes q between adjacent zones.

$$\Delta x \frac{d}{dt}\overline{\rho h} = -\left[q_{+} - q_{-} - \left((\rho h)_{+} - (\rho h)_{-}\right) v_{\Gamma,heat}\right] \tag{6.4}$$

$$v_{\Gamma,heat} = \frac{q_{I,+} - q_{II,-}}{(\rho h)_{I,+} - (\rho h)_{II,-}} \tag{6.5}$$

As in the case of the diffusive mass fluxes, information about the temperature profile and, thus, the temperature gradients at the phase interfaces is lost in the integration process and has to be replaced with a suitable model assumption. In analogy to Eq. 3.23, the heat flux for zone I can be approximated as follows:

$$q_{+} = \lambda \left.\frac{d}{dx}T\right|_{x=x_{+}} \approx= \lambda \frac{T_{+} - \overline{T}}{0.5\Delta x} \tag{6.6}$$

where $\overline{T}$ is the bulk temperature and T_+ is the temperature at the position of the phase interface x_+. Consistent with the use of bulk-averaged enthalpies $\overline{\rho h}$, temperatures $\overline{T}$, and bulk-averaged oxygen partial densities $\overline{\rho}_O$, material and transport properties are also treated as bulk properties.

Since there must be a leap in the enthalpy profile in order to derive a moving boundary condition, while the temperature profile must remain continuous (Eq. 6.2 and Eq. 6.3), a sharp interface can only be expected in the case of pure substances whose phase lines of two-phase coexistence (e.g., solidus and liquidus lines) manifest in a joint solidification and melting temperature.

In the case of a binary solution, two-phase regions ensure a continuous temperature profile between adjacent phases. These two-phase regions also bridge over the leaps in the enthalpy and concentration profiles so that these become continuous (see Fig. 6.2). These two-phase regions further imply the absence of imbalances in the heat and mass fluxes at the phase interfaces between single-phase and two-phase regions. These two characteristics, however, conflict with the moving boundary conditions as a key element of the integral approach (Eq. 3.26 and Eq. 6.4). Consequently, the introduction of a two-phase zone into an integral model is out of the question. In contrast, moving boundary conditions, along with their inevitable assumption of sharp interfaces, require these two-phase regions to be neglected for the sake of both the heat and mass transport model. Due to this, the integral approach is not applicable to heat transfer problems in binary systems since neglecting two-phase regions implies leaps in the temperature profile, which are again unphysical.

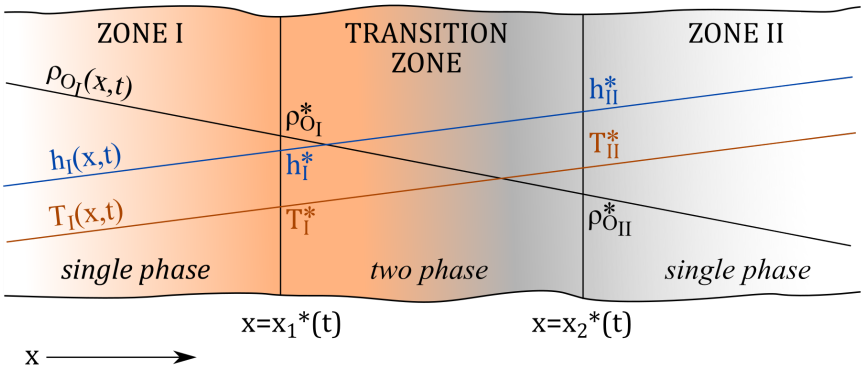

Figure 6.2.: Effect of two-phase transition zones on concentration, enthalpy, and temperature profiles in an integral model.

Modeling heat transport with an extended mass transport model

Since the integral approach is inapplicable to the heat transport problem in the binary Zr-O system, a different approach for the modeling of the heat transfer and the reproduction of thermally-induced phase changes must be found. Inspired by the work of Veshchunov et al. [7], this work considers only the mass transfer a moving boundary problem and covers the heat transfer between zones with additional heat balance equations. Hence, it is assumed that the oxygen transfer between two adjacent phases, which are separated by a two-phase region, can be approximated as the transport between two single-phase zones over a virtual sharp phase interface at which a local thermodynamic equilibrium is attained. Thereby, the basis of the integral model for the mass transfer, which can be summarized by Eq. 3.22 and Eq. 3.26, remains unchanged.

The required heat balance equations are derived in accordance with Eq. 6.4. However, the corresponding terms for the velocity of the moving interface due to the heat transfer $v_{\Gamma,heat}$ are replaced with the solution of the mass transport model $v_{\Gamma,mass}$.

$$\Delta x \frac{d}{dt}\overline{\rho h} = -\left[q_+ - q_- - \left((\rho h)_+ - (\rho h)_-\right) v_{\Gamma,mass}\right] \tag{6.7}$$

Heat fluxes are calculated based on the global temperature gradient between adjacent zones:

$$q_+ = q_- \approx \lambda^* \frac{\overline{T}_+ - \overline{T}_-}{x_+ - x_-} \tag{6.8}$$

The extended integral model described here can simulate heat and mass transport resulting from the global non-equilibria of temperatures and concentrations in a considered system. On the other side, it lacks an explicit expression for heat effects caused by chemical reactions. Moreover, it is incapable of accounting for thermally-induced phase transitions (e.g., solidification, melting, or other allotropic transformations) at this very stage of development.

In fact, the heat balance equation given in Eq. 6.7 is significantly different compared to the heat balance equations used by Veshchunov et al. [7] (Eq. 3.32). In their model, heat effects are included in the heat balances via the heat fluxes that are based on the interface temperatures T^*. These interface temperatures, in turn, change depending on the extent of the chemical reaction caused by mass fluxes over that interface, which are assumed to cause heat effects at its very position (see Eq. 3.32 and Eq. 3.33 in Section 3.2).

The novel contribution ofthe advanced integral model presented here is to cover heat effects implicitly with the aid of the physical self-consistent thermodynamic data of the lookup table (see Chapter 4). In a similar manner, phase changes due to thermal effects such as solidification, melting, and allotropic transformations are accounted for through the coupling to the thermodynamic lookup table. Due to the high complexity and critical importance of both concepts for this work, they are delineated in a subsequent section (see Section 6.3).

Since the modeling assumptions presented in this section have a substantial impact on the depiction of the oxidation process but cannot be assessed further from a theoretical viewpoint, a spatially discretized model, which can resolve both spatial concentration and temperature profiles and the formation of two-phase regions, is introduced in Chapter 7 and used as a point of reference throughout this work. In this context, the focus of Chapter 10 is directed exclusively at the assessment of the reproduction of thermally-induced phase transitions by the extended integral model in order to determine its capabilities and applicability.

6.2. System of equations

With the integral model describing the oxygen mass transport (Eq. 3.22 and Eq. 3.26), its extension by the heat balances, and the equations for the heat fluxes, the differential algebraic system of equations for the heat and mass transfer is complete. This system consists of two mass balances (one for each component c (Zr, O), Eq. 3.22) and one heat balance for each zone (Eq. 6.7), one equation for the velocity of each phase interface (Eq. 3.26), and another equation for the heat flux passing each interface (Eq. 6.8).

In the following, an exemplary system of equations is described by continuing with the model system introduced in Section 3.2, which consists of two zones: one from solid metal α-Zr and the other from solid oxide γ-ZrO$_2$ that is in contact with the environment (see Fig. 6.3). The corresponding system of equations describing the oxygen mass transport reads:

$$\Delta x_I \frac{d}{dt}\overline{\rho}_{OI} = -\left[j_{OI,surf.} - j_{OI,int.} - (-\rho_O v_{int.})\right] \tag{6.9}$$

$$\Delta x_{II} \frac{d}{dt}\overline{\rho}_{OII} = -\left[j_{OII,int.} - (\rho_O v_{int.})\right] \tag{6.10}$$

Since the diffusion of zirconium is assumed to be negligible, the system of equations describing the zirconium mass in each zone is the following:

$$\Delta x_I \frac{d}{dt}\overline{\rho}_{ZrI} = -\left[-(-\rho_{Zr} v_{int.})\right] \tag{6.11}$$

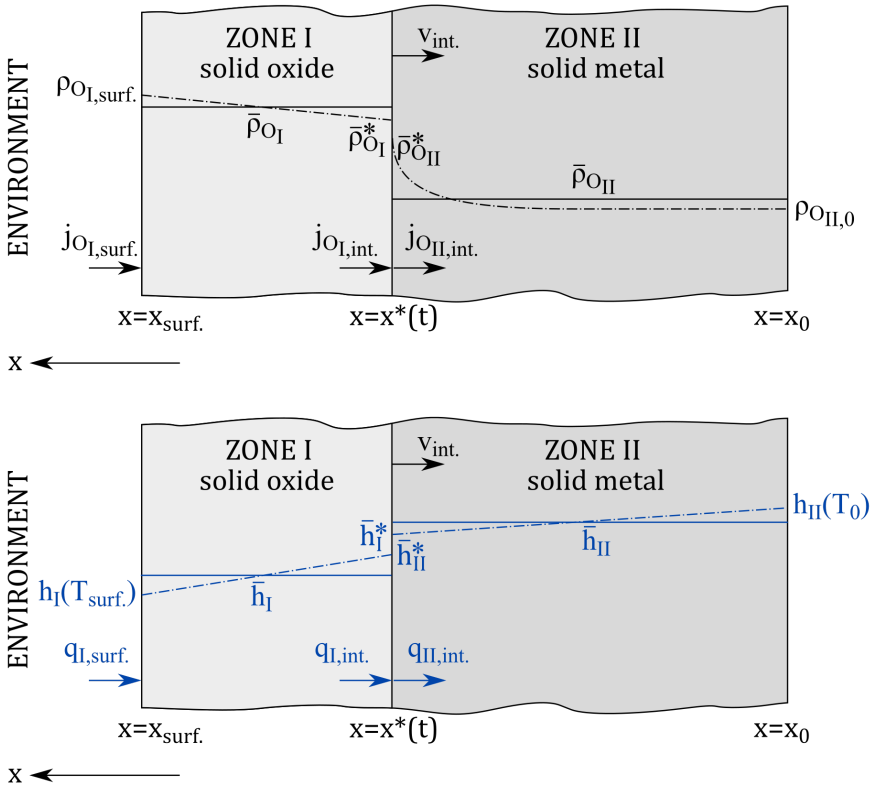
ENVIRONMENT
ZONE I
solid oxide
ZONE II
solid metal
v_int.
ρ_OI,surf.
ρ̄_OI
ρ̄*_OI
ρ̄*_OII
ρ̄_OII
ρ_OII,0
j_OI,surf.
j_OI,int.
j_OII,int.
x=x_surf.
x=x*(t)
x=x_0
x
ENVIRONMENT
ZONE I
solid oxide
ZONE II
solid metal
v_int.
h_II(T_0)
h̄*_I
h̄*_II
h̄_II
h_I(T_surf.)
h̄_I
q_I,surf.
q_I,int.
q_II,int.
x=x_surf.
x=x*(t)
x=x_0
x

Figure 6.3.: Illustration of the composed concentration and enthalpy profiles of an exemplary model system comprising an oxidic and a metallic phase underlying the advanced integral model (arbitrary boundary conditions).

$$\Delta x_{II} \frac{d}{dt} \bar{\rho}_{Zr\,II} = -\left[-\left(\rho_{Zr} v_{int.}\right)\right] \tag{6.12}$$

These equations are complemented by an algebraic equation for the velocity of the inner phase interface:

$$v_{int.} = \frac{j_{O\,I,int.} - j_{O\,II,int.}}{\rho_{O\,I,int.} - \rho_{O\,II,int.}} \tag{6.13}$$

The corresponding extension of the system of equations by the heat transport equations for this exemplary system reads as follows:

$$\Delta x_I \frac{d}{dt} \overline{\rho h}_I = -\left[q_{I,surf.} - q_{I,int.} - \left(-\rho h v_{int.}\right)\right] \tag{6.14}$$

$$\Delta x_{II} \frac{d}{dt} \overline{\rho h}_{II} = -\left[q_{II,int.} - \left(\rho h v_{int.}\right)\right] \tag{6.15}$$

The heat fluxes between both zones are described by the following equation:

$$q_{I,int.} = q_{II,int.} \approx \lambda_{int.} \frac{\overline{T}_I - \overline{T}_{II}}{\Delta x_{I,II}} \tag{6.16}$$

This system of equations is suitable for a plain model case. Systems with three or more distinct phases/zones can be modeled by a simple extension of the system of equations described above.

In a system that is subject to temperature changes and chemical transformation processes, the density is not constant. Furthermore, the oxygen uptake caused by the zirconium-steam reaction leads to an increase in the oxygen mass and, therefore, the volume. Under these conditions, a system confined by a fixed geometry would develop mechanical tensions. To account for the assumption of the absence of mechanical forces, the description of each zone is supplemented by another algebraic equation. This equation updates the zones' extensions Δx_z based on their total mass m_z, their cross-sectional area A_z, and the density ρ_z of the present phases. In the case of a zone with the zone index $z = I$, this equation reads:

$$\Delta x_I = \frac{m_I}{\rho_I A_I}, \text{ with } m_I = m_{O_I} + m_{Zr_I} \tag{6.17}$$

As mentioned in Section 3.2, the initial and boundary conditions for the outer surfaces of the system that is to be modeled with an extended integral model can be chosen freely. The only requirement is that they do not contradict and, more specifically, match the specifications of the thermodynamic lookup table.

6.3. Coupling to the lookup table

Heat and oxygen mass transfer result from gradients that are caused by the global non-equilibria of temperatures and concentrations. The difficulty regarding the modeling of oxidation processes is to substantiate the heat and mass transport processes with the limited means of equilibrium thermodynamics. This stems from the fact that data describing non-equilibrium thermodynamics are not available (see Section 2.1). Hence, it is the central assumption of the integral model that the kinetics of the chemical reactions are much faster than the transport processes. This means that local thermodynamic equilibrium is instantly established at the phase interfaces. Furthermore, it is likewise assumed that thermodynamic equilibrium states can be used to express the states of the zone bulks.

Therefore, the lookup table is coupled to the extended integral diffusion model to achieve a physically consistent description of the thermodynamic states of all zones and phase interfaces. A coupling of the heat and mass transfer model to the lookup table is made possible because the solution variables, the bulk oxygen partial density $\overline{\rho}_O$, and the specific bulk enthalpy $\overline{\rho h}$ can be readily transformed into molar oxygen fractions $\overline{x}_O$ and molar enthalpies $\overline{h_m}$ that are used by the lookup table. In turn, a zone's bulk molar oxygen fraction $\overline{x}_O$ and molar enthalpy $\overline{h_m}$ unambiguously define its thermodynamic state. Hence, in the first step, a linear interpolation algorithm is used to calculate the bulk temperatures $\overline{T}$ of all zones from their bulk molar oxygen fractions $\overline{x}_O$ and molar enthalpies $\overline{h_m}$.

$$\overline{T} = f\left(\overline{x}_O, \overline{h_m}\right) \tag{6.18}$$

This two-step linear interpolation algorithm exploits the fact that the molar enthalpy h_m is a monotonically increasing function of the temperature T if the oxygen molar fraction x_O is constant. In its first step, the algorithm sets up an array that assigns one interpolated molar enthalpy value h_m that matches the cell's known molar oxygen fraction x_O to each temperature step of the lookup table.

$$\overline{h_m} = f(\overline{T}), \text{ if } \overline{x_O} = const. \tag{6.19}$$

In the second step of the interpolation, the algorithm searches within this array for the enthalpy values enclosing the molar enthalpy value of the cell h_m and interpolates the temperature T from their relative contributions by reproducing the value h_m, assuming again a linear dependency. Fig. 6.4 shows a visualization of this concept.

$$h_m(T) = \epsilon h_m(T_{high}) + (1 - \epsilon) h_m(T_{low}) \tag{6.20}$$

$$\epsilon = \frac{h_m(T) - h_m(T_{low})}{h_m(T_{high}) - h_m(T_{low})} \tag{6.21}$$

$$T = \epsilon T_{high} + (1 - \epsilon) T_{low} \tag{6.22}$$

Consequently, heat effects caused by gradual concentration changes within the zones are implicitly included via a temperature feedback that makes their explicit formulation obsolete. Analogously, heat effects of the various chemical phase transitions, and due to solidification or melting and allotropic transformations, are implicitly captured by the model.

With the bulk temperatures $\overline{T}$ determined, it is possible to calculate the heat fluxes q between two adjacent zones (Eq. 6.8). Heat contributions from phase transitions (chemical reactions) at the interfaces are covered by the bulk enthalpy differences of the donor and acceptor phases $\left(\overline{\rho h}\right)_{I,+}$ and $\left(\overline{\rho h}\right)_{II,-}$.

In the next step of the coupling, the zones' molar phase fractions f^j of the phases j (α-Zr, β-Zr, α-ZrO$_2$,β-ZrO$_2$, γ-ZrO$_2$, liq.) are determined via the comparison of the zones' molar

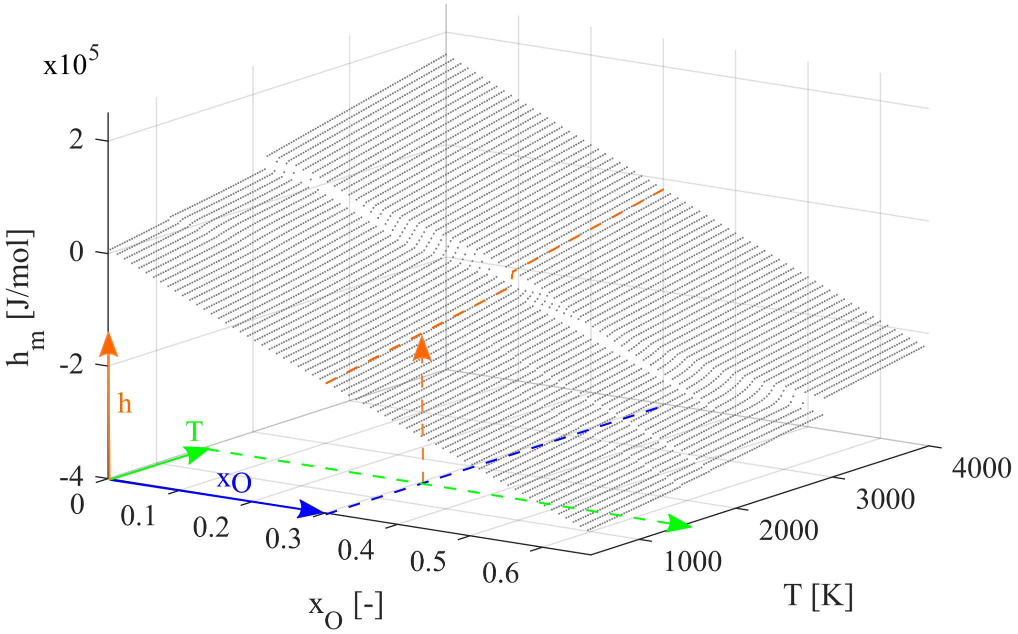

Figure 6.4.: Illustration of the concept used for the interpolation of temperature T with the aid of the oxygen molar fraction x_O and molar enthalpy h_m.

oxygen fractions $\overline{x}_O$ and bulk temperatures $\overline{T}$ with the phases' stability regions known from the lookup table. In the course of the same process, the phases' molar oxygen fractions in phase equilibrium concentrations $x_O^{j,*}$ are determined. Both procedures are possible since the lookup table holds the same information as a binary phase diagram of the Zr-O system, as shown in Section 4.2. Hence, an algorithm was developed to extract the values of molar phase fractions f^j and saturation limits $x_O^{j,*}$ from the lookup table based on the information about the zones' bulk molar oxygen fractions $\overline{x}_O$ and bulk temperatures $\overline{T}$ at hand.

$$\overline{f}^j = f\left(\overline{x}_O, \overline{T}\right), \text{ with } \sum_j^6 \overline{f}^j\left(\overline{x}_O, \overline{T}\right) = 1, \text{ with } j = 1, ..., 6 \tag{6.23}$$

$$\rho_O^{j,*} = f\left(\overline{x}_O, \overline{T}\right) \tag{6.24}$$

The concept of the derivation of the zones' molar phase fractions $\overline{f}^j$ and saturation limits $\overline{x}_O^{j,*}$ is sketched in Fig. 6.5. In the first example (blue arrows), a zone's bulk-averaged molar oxygen fraction is $\overline{x}_O = 0.2$ and its bulk temperature is $\overline{T} = 1500\,K$. This point lays within the stability region of the α-Zr phase so that its molar phase fraction is $\overline{f}^{\alpha-Zr} = 1.00$ and the phase fraction of any other phase is $\overline{f}^{j \neq alpha-Zr} = 0.00$. The α-Zr phase's saturation limits $\overline{x}_O^{\alpha-Zr,*}$, which are used to calculate the phase equilibrium concentrations $\rho_O^{\alpha-Zr,*}$, are obtained by following the isotherm $(1500\,K)$ to the phase's left- and right-hand side lines of two-phase coexistence ($\overline{x}_O^{\alpha-Zr,low,*} = 0.12$ and $\overline{x}_O^{\alpha-Zr,high,*} = 0.30$). The second

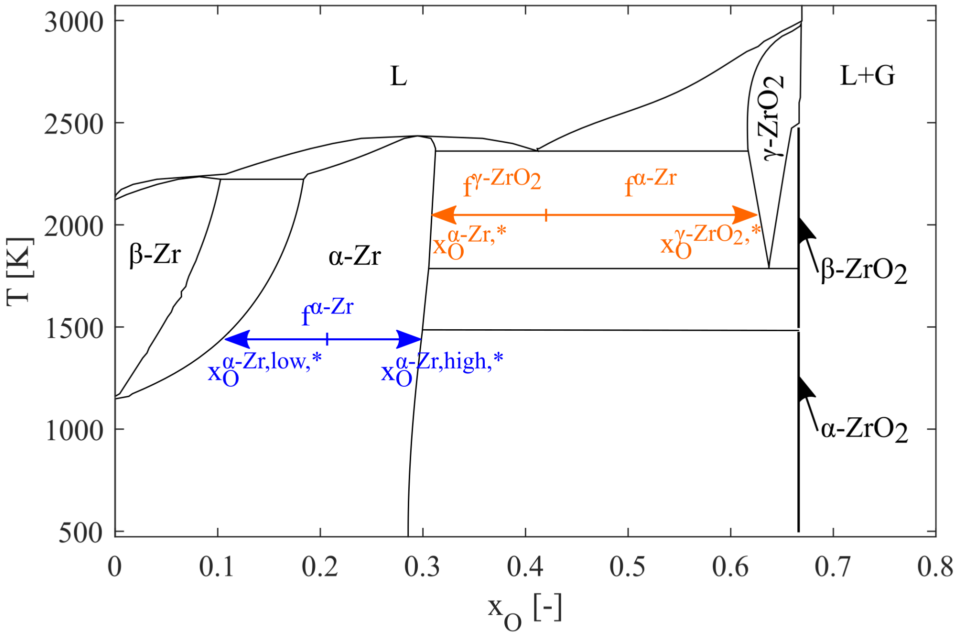

Figure 6.5.: Illustration of the concept used to derive molar oxygen fractions of phases in phase equilibrium x_O^*.

example is a zone with a bulk molar oxygen fraction of $\overline{x}_O = 0.4$ and a bulk temperature of $\overline{T} = 2000\,K$ (orange arrows). This point lays within a two-phase region between α-Zr and γ-ZrO$_2$. The molar phase fractions of both phases are calculated using the lever rule ($\overline{f}^{\alpha-Zr} = 0.71$ and $\overline{f}^{\gamma-ZrO_2} = 0.29$). The phases' saturation limits $\overline{x}_O^{j,*}$ are again obtained by following the isotherm ($\overline{T} = 2000\,K$) to the lines of two-phase coexistence ($\overline{x}_O^{\alpha-Zr,*} = 0.31$ and $\overline{x}_O^{\gamma-ZrO_2,*} = 0.63$).

To avoid numerical instabilities in the execution of the advanced integral model, the phase equilibrium concentrations at the interfaces ${\rho_O}^{j,*}$ are calculated using the temperature of the zones' bulks $\overline{T}$ and, thus, explicitly do not use temperatures at the phase interfaces. These are not determined in the model. Negative effects of this simplification are assessed in Chapter 10.

In a last step, having determined both the temperatures $\overline{T}$ and the phase fractions $\overline{f}^j$, the material and transport properties of the various phases are updated, including the density $\rho^j(\overline{T})$, the diffusion coefficients $D_O^j(\overline{T})$ and the thermal conductivities $\lambda^j(\overline{T})$.

Thermally-induced phase changes

Since the phase fractions f^j of a zone in the advanced integral model are not preset but redetermined in each time step, the phase transitions caused by rapid temperature changes are accounted for via the conversion of single-phase zones into two-phase zones and vice versa. Therefore, changing phase fractions can be understood either as the motion of virtual phase interfaces within a zone or the changing proportion of segregations within a host matrix (see Fig. 6.6). By means of this concept, the model can capture all phase transitions intrinsic to the Zr-O binary system and, thus, is not limited to specific temperature ranges. This is the major advantage of this modeling approach over other models given in the literature that are also based on the integral approach. The capabilities and limitations of this approach are thoroughly investigated in Chapter 10.

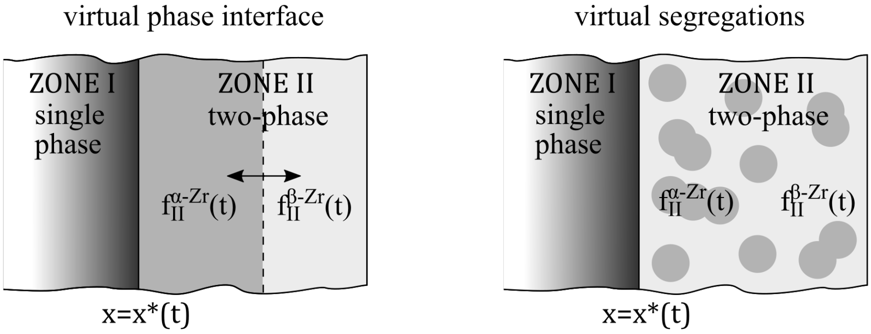
virtual phase interface
ZONE I
single
phase
ZONE II
two-phase
$f_{II}^{\alpha\text{-}Zr}(t)$
$f_{II}^{\beta\text{-}Zr}(t)$
x=x*(t)
virtual segregations
ZONE I
single
phase
ZONE II
two-phase
$f_{II}^{\alpha\text{-}Zr}(t)$
$f_{II}^{\beta\text{-}Zr}(t)$
x=x*(t)

Figure 6.6.: Interpretations of changing phase fractions f^j in the advanced integral model.

Since the bulk oxygen concentration of each phase $\overline{\rho}_O^j$ and the phase boundary concentration $\rho_O^{j,*}$ in two-phase zones match, those zones do not contribute to the oxygen mass transport as long as they are undergoing a phase transition. If a zone emerges or vanishes, the model is automatically stopped, modified, and restarted.

Implementation

The differential algebraic system of equations is solved with the help of the computer software MATLAB (version R2017a) using the solver ode15s. Programming flowcharts illustrating the implementation of the coupling of the advanced integral model to the lookup table, as well as to the materials library, are presented in Appendix D.

7. Spatially discretized model

In the development of a fast-running model for the high-temperature oxidation of zirconium in steam for the application in severe accident analysis codes, a trade-off between physical precision and computation time must be made. Using the integral approach, this trade-off is to regard only the mass transfer (chemical phase transitions) as a moving boundary problem, but thermally-induced phase transitions on the level of the zones themselves. This is because the integral approach is incapable of resolving two-phase regions between adjacent zones (see Chapter 6). The assumptions made in this context should influence the depiction of the model physics, but they cannot be further assessed from a theoretical viewpoint, and experimental data suitable for validation purposes are not available. Therefore, the comparison to another numerical model is without alternative.

The aforementioned modeling approaches, parabolic rate equations (Section 3.1), and integral models (Section 3.2 and Chapter 6) are based on the same physical theories, Fick's second law of diffusion, and the heat equation. Therefore, it is logical to assess the capabilities and limitations of the extended integral model by comparing it to a precise spatially discretized numerical solution that builds on the same model physics. Since the coupling of a spatially discretized model to a thermodynamic lookup table is a novel approach developed in the course of this work, which requires some ingenuity, this chapter is dedicated to its detailed description.

To approach this precise numerical solution, which is based on Fick's second law of diffusion and the heat equation, the vertical method of lines is applied and the spatial dimension is discretized. Thus, a cell index is introduced so that, hereinafter, cells are characterized by indices i and their left- and right-hand cell boundaries to the indices $i - 1/2$ and $i + 1/2$. Since both Fick's second law and the heat equation are partial differential equations that possess conservative features, the finite volume method is applied, which preserves this property. This choice is also advisable from the viewpoint of numerical stability because concentration and enthalpy profiles (different from temperature profiles) feature discontinuities, which require a certain degree of robustness of the applied method (see Chapter 6).

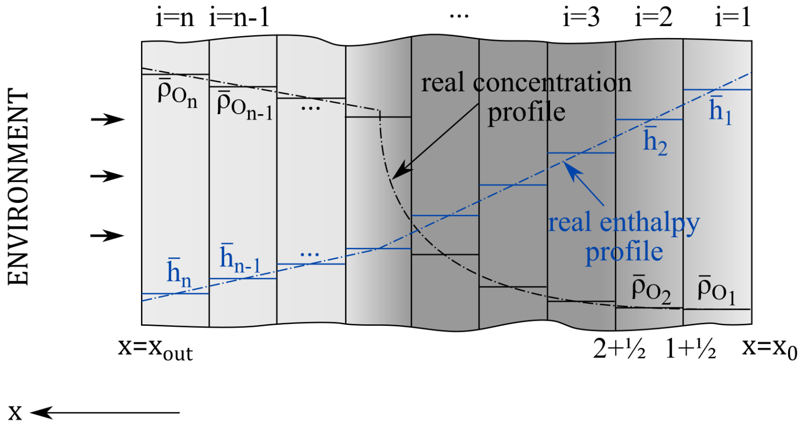
i=n
i=n-1
...
i=3
i=2
i=1
ENVIRONMENT
$\bar{\rho}_{O_n}$
$\bar{\rho}_{O_{n-1}}$
...
real concentration profile
$\bar{h}_1$
$\bar{h}_2$
real enthalpy profile
$\bar{h}_n$
$\bar{h}_{n-1}$
...
$\bar{\rho}_{O_2}$
$\bar{\rho}_{O_1}$
$x=x_{out}$
2+½
1+½
$x=x_0$
x

Figure 7.1.: Sketch of the discretization scheme using a finite volume approach.

In the following sections, such a model is first derived for the case of an isothermal one-phase diffusive mass transfer problem, which is subsequently extended by the capacity to capture multi-phase systems and, later, to include heat transport processes. Once the system of equations is established, the focus is directed to the implementation of the coupling of heat and mass transfer using the physically self-consistent thermodynamic data of the lookup table.

7.1. Mass transport

Single-phase mass transfer

The diffusion equation is spatially discretized using finite volumes V_i:

$$\frac{D}{Dt}\int\limits_{V_i} \rho_{O_i} dV = -\int\limits_{V_i} \nabla \cdot \vec{j}_{O_i} dV, \text{ with } i = 1, ..., n \tag{7.1}$$

The application of Gauss's theorem to Eq. 7.1 allows the substitution of the volume integral on the right-hand side with a surface integral:

$$\int\limits_{V_i} \frac{d}{dt}\rho_{O_i} dV = -\oint\limits_{\partial V_i} \left(\vec{j}_{O_i} \cdot \vec{n}\right) dA \tag{7.2}$$

In one-dimensional space, this surface integral can be expressed by the fluxes evaluated at the left and right cell boundaries, $A_{i-1/2}$ and $A_{i+1/2}$ (similar to Fig. 3.4):

$$\frac{d}{dt}m_{Oi} = A_{i+1/2} D_{Oi+1/2} \left.\frac{d\rho_O}{dx}\right|_{i+1/2} - A_{i-1/2} D_{Oi-1/2} \left.\frac{d\rho_O}{dx}\right|_{i-1/2} \tag{7.3}$$

The obtained equation describes temporal change in the oxygen mass m_{Oi} in a cell i. Divided by the cell volume V_i, it yields the average oxygen partial density $\overline{\rho}_{Oi}$.

The oxygen mass fluxes at the positions of the cell interfaces are calculated using gradients that are approximated by the central difference quotient of first order. Assuming diffusion coefficients that are independent of the oxygen concentration but dependent on the existing phases, this equation can be further simplified:

$$\Delta x_i \frac{d}{dt}\overline{\rho}_{O_i} = D_O \frac{\overline{\rho}_{O_{i+1}} - \overline{\rho}_{O_i}}{x_{i+1} - x_i} - D_O \frac{\overline{\rho}_{O_i} - \overline{\rho}_{O_{i-1}}}{x_i - x_{i-1}} = j_{Oi+1/2} - j_{Oi-1/2} \tag{7.4}$$

In this way, the equation is transformed into an ordinary differential equation that describes diffusive mass transfer in single-phase systems and is suitable for a numerical solution. In the following, all properties denoted by a cell index i are considered cell-averaged bulk properties and hereinafter indicated without bars.

In the case of the zirconium, diffusive mass fluxes can be neglected because their diffusivity compared to the diffusivity of oxygen is negligible. Therefore, the zirconium acts as a host matrix and the zirconium mass of a cell i is assumed to remain unaltered so that there is no separate mass balance for this substance.

$$m_{Zr_i} = const. \tag{7.5}$$

Multi-phase mass transfer

Eq. 7.4 cannot be readily applied to multi-phase systems in which it must be considered that each phase j contributes to the overall concentration profile within its own individual limits of stability, which in turn gives rise to discontinuities in the concentration profiles. This entails that transport properties such as the diffusion coefficient $D_{O_i}^j$ or material properties such as the density ρ_i^j are subject to drastic changes, which depend on the phases present.

In the Zr-O binary phase diagram depicted in Fig. 4.2, there are six phases j (α-Zr, β-Zr, α-ZrO$_2$, β-ZrO$_2$, γ-ZrO$_2$, L). Still assuming isothermal conditions, those phases are separated by sharp interfaces at which their individual concentration profiles merge. In a model that is spatially discretized into finite volumes on a fixed grid, the movement of these phase interfaces cannot be resolved. Consequently, there are multi-phase cells that host a gradual transition from one phase to another. Following the assumption of local thermodynamic equilibrium in each cell, the phases in multi-phase cells assume their saturation limits, as indicated by the equilibrium concentrations $\rho_{O_i}^{j*}$.

$$\rho_{O,i} = \sum_{j=1}^{6} \phi_i^j \rho_{O_i}^{j*}, \text{ with } j = 1, ..., 6 \text{ and } \sum_{j=1}^{6} \phi_i^j = 1 \tag{7.6}$$

In an isothermal model of a binary system, the changing phase volume fraction ϕ_i^j can be used to trace the movement of the phase interface in the spatial domain of a cell i. Then, the oxygen mass flux passing through that virtual phase interface and the change in the volume fractions can be calculated analogously to the procedure for integral models, as described in Section 3.2.

However, the assumption of a sharp phase interface is incompatible with the modeling of temperature transients in binary systems since these cases involve the possible occurrence of two-phase regions. These regions are extended and gradual transitions of two or more phases into each other, which can span over multiple cells. They can result, for example, from heat transfer processes that enforce temperature-related phase transitions, which are faster than those resulting from orderly mass diffusion. To furnish the model with the ability to capture this effect, the volume fraction ϕ_i^j has to be interpreted as a phase's proportion of the cross-sectional area of a cell i, which is available for mass transfer processes:

$$j_{O_{i+1/2}} = \sum_{j=1}^{6} \phi_i^j F_{i+1/2}^j = \sum_{j=1}^{6} \phi_i^j D_O^j \frac{\rho_{O_{i+1}}^j - \rho_{O_i}^j}{x_{i+1} - x_i}, \text{ with } j = 1, ..., 6 \tag{7.7}$$

If sufficiently small cell volumes V_i are used, this solution converges against the solution that includes a tracing method for the phase interface. The computation of the phase saturation limit $\rho_{O_i}^{j*}$ and phase volume fraction ϕ_i^j using a state diagram is explained in Section 7.4.

The occurrence of multi-phase cells is crucial for a spatially discretized model since they assure a smooth transition of the concentration profiles of different phases. When a phase interface and a cell boundary lie on top of each other, phases exist only on one side of the boundary. Therefore, each time one of the two partial oxygen densities that is required to build a concentration gradient from one cell to the other is missing and the fluxes reaching over the boundary cannot be calculated. Hence, the cell boundary becomes a numerically insurmountable obstacle for the mass transfer (see Fig. 7.2 (left)).

Resulting from the oxygen gradient between both adjacent cells, there must be a point in space where each phase reaches its concentration limit. This does not necessarily have to be the equilibrium point of both phases at the same time if, for example, a third intermediate phase is missing. To avoid unphysical results and numerical instabilities of the code, these concentration limits are introduced as virtual partial oxygen densities $\rho_{O_{i,virt.}}^j$ and projected onto the neighboring cell, thereby building a concentration gradient (see Fig. 7.2 (right)).

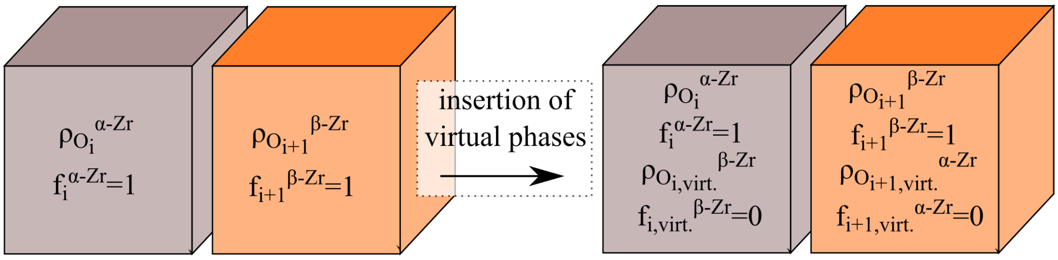

Figure 7.2.: Concept of virtual partial oxygen densities in neighboring cells.

This concept requires a further complement. If the flux passing a cell boundary is calculated at the position of the boundary itself using averaged properties, the flux inevitably comes to a standstill. This is because the concentration of at least one of the two cells will approach its equilibrium concentration and the concentration gradient will, therefore, become zero. Hence, for each cell boundary $(i+{}^1\!/_2)$, a left- and a right-sided flux, $j_{O_{i,i+1/2}}$ and $j_{O_{i+1,i+1/2}}$ are calculated using the properties of the left (i) and right cell $(i+1)$ and, in analogy to the integral model, only the dominant flux is used:

$$j_{O_{i,i+1/2}} = \sum_{j=1}^{6} \left(\phi_i^j D_{O_i}^{j} \frac{\rho_{O_{i+1}}^{j} - \rho_{O_i}^{j}}{x_{i+1} - x_i} \right), \text{ with } j = 1, ..., 6 \tag{7.8}$$

$$j_{O_{i+1,i+1/2}} = \sum_{j=1}^{6} \left(\phi_{i+1}^j D_{O_{i+1}}^{j} \frac{\rho_{O_{i+1}}^{j} - \rho_{O_i}^{j}}{x_{i+1} - x_i} \right), \text{ with } j = 1, ..., 6 \tag{7.9}$$

$$j_{O_{i+1/2}} = \begin{cases} j_{O_{i,i+1/2}}, & \text{if } \left| j_{O_{i,i+1/2}} \right| \geq \left| j_{O_{i+1,i+1/2}} \right| \\ j_{O_{i+1,i+1/2}}, & \text{else} \end{cases} \tag{7.10}$$

In Eq. 7.8 to Eq. 7.10, the use of cell-dependent diffusion coefficients for the same phase, $D_{O_i}^{j}$ and $D_{O_{i+1}}^{j}$, is a preparation for lifting the assumption of isothermal conditions in the following section, which describes the modeling of the heat transfer.

7.2. Heat transport

Heat transfer modeling is based on three pillars. The first pillar is the heat transfer model itself, which captures heat fluxes between the different cells i caused by the global non-equilibrium of temperatures within the spatial definition. The second pillar consists of the boundary conditions, which provide for the heat transfer to the surrounding environment (freely selectable) and the enthalpy required for the dissociation of hydrogen. The third pillar is the coupling to the thermodynamic lookup table, which captures heat effects due to concentration changes (enthalpy of solution), phase changes resulting from chemical reactions (enthalpy of reaction), and phase changes caused by thermal constraints (e.g., enthalpy of fusion or enthalpy of allotropic transformation).

Using the analogy between heat and mass transfer, a solution of the heat equation in the form of an ordinary differential equation is derived using the same scheme as for the single-phase mass transfer:

$$\Delta x_i \frac{d}{dt}\overline{\rho h_i} = \lambda_{i+1/2}\frac{T_{i+1}-T_i}{x_{i+1}-x_i} - \lambda_{i-1/2}\frac{T_i - T_{i-1}}{x_i - x_{i-1}} = q_{i+1/2} - q_{i-1/2} \tag{7.11}$$

The result is an expression stating that the change in the enthalpy per volume $\overline{\rho h_i}$ of a cell i with a length Δx_i is equal to the heat fluxes calculated from the thermal conductivities at the positions of the cell boundaries $\lambda_{i-1/2}$ and $\lambda_{i+1/2}$ multiplied by the respective approximations of the temperature gradients. This is sufficient since the temperature is a continuous function and all phases in a cell are assumed to be instantly in local thermodynamic equilibrium and thus share a common temperature T_i. The thermal conductivities at the positions of the cell boundaries are calculated using the harmonic mean:

$$\lambda_{i+1/2} = \frac{1}{\dfrac{\omega_i}{\lambda_i} + \dfrac{(1-\omega_i)}{\lambda_{i+1}}} \tag{7.12}$$

where ω_i is the relative distance of the center of cell i to the interface $i + 1/2$, which can be expressed as follows:

$$\omega_i = \frac{\Delta x_i}{\Delta x_i + \Delta x_{i+1}} \tag{7.13}$$

The cell-averaged thermal conductivities of each cell λ_i are, in turn, calculated as the harmonic means of the contributions of the different phases' thermal conductivities λ_i^j weighted by their phase volume fractions ϕ_i^j:

$$\lambda_i = \frac{1}{\sum_{j=1}^{6} \frac{\phi_i^j}{\lambda_i^j}}, \text{ with } j = 1, ..., 6 \tag{7.14}$$

7.3. System of equations

The system of ordinary differential equations, which can be formed by combining a mass balance equation (Eq. 7.4 with Eq. 7.8 to 7.10) with a heat balance equation (Eq. 7.11) for each cell i, is capable of describing the heat and mass transfer in a system subject to global imbalances of temperatures and concentrations.

To account for the assumption of the absence of mechanical forces, this system of equations must be extended further. In a system that is subject to temperature fluctuations and chemical transformation processes, the density is not constant. Furthermore, oxygen uptake leads to an increase in mass and, therefore, volume. Under these conditions, a system confined by a fixed geometry would develop mechanical tensions. Accordingly, an algebraic equation for the explicit calculation of the cell extension Δx_i based on the cell total mass m_i and the cell density ρ_i is implemented in the model.

$$\Delta x_i = \frac{m_i}{\rho_i A}, \text{ with } m_i = m_{O_i} + m_{Zr_i} \tag{7.15}$$

Initial conditions and boundary conditions for the outer surfaces of the system of this model can be chosen freely. The model is capable of adjusting to any given configuration as long as it is numerically stable.

7.4. Coupling to the lookup table

The linkage of the heat and mass transport equations and their coupling to the thermodynamic lookup table is realized in strong analogy to the coupling efforts made in the context of the integral model, which were presented in Section 6.3. However, through the assumption of local thermodynamic equilibrium in each cell i and the absence of moving boundaries, a coupling is significantly easier to achieve. The assumption of local thermodynamic equilibrium implies an immediate relaxation of chemical constraints, excluding the occurrence kinetic effects such as undercooling or superheating.

As in the case of the integral model, the thermodynamic state of a cell i with regard to the lookup table is unambiguously defined by its partial oxygen density $\overline{\rho}_{O,i}$ and specific enthalpy $\overline{\rho h}_i$, which can be readily converted into a molar oxygen fraction $\overline{x}_{O,i}$ and molar enthalpy $\overline{h}_{m,i}$. Hence, the same iterative tools that were presented in Section 6.3 are used to determine firstly the bulk temperature $\overline{T}_i$ of each cell i, secondly the phase fractions $\overline{f}_i^j$ of each of the six phases j in each cell i, and thirdly the phase equilibrium concentrations $\rho_{O_i}^{j,*}$ at the cell boundaries of the cell i (again for each of the six phases j).

$$\overline{T_i} = f(\overline{x}_O, \overline{h}_m) \tag{7.16}$$

$$\overline{f}_i^j = f(\overline{x}_{Oi}, \overline{h}_{mi}) \text{ with } j = 1, ..., 6 \text{ and } \sum_{j=1}^{6} \overline{f}_i^j = 1 \tag{7.17}$$

$$\overline{\rho}_{O_i}^{j,*} = f(\overline{x}_{Oi}, \overline{h}_{mi}) \text{ with } j = 1, ..., 6 \tag{7.18}$$

Due to the small scale of each cell, it is assumed that the phase equilibrium concentrations $\rho_{O_i}^{j*}$ at the cell boundaries can be estimated with the help of a cell's bulk temperature. This is also recommended as a way to avoid unphysical results in case the phases of a cell cannot exist at the interface's temperature.

Implementation

A programming flowchart illustrating the coupling of the spatially discretized model to the lookup table and the materials library is presented in Appendix D. As in the case of the advanced integral model, the derived differential algebraic system of equations is solved with the help of the computer software MATLAB (version R2017a) using the solver ode15s.

The use of a spatially discretization scheme to model heat and mass transfer in the case of the high-temperature oxidation of zirconium in steam has certain advantages. Since both concentration and temperature profile are spatially resolved, such a model can capture the formation of extended two-phase regions. It can, therefore, be understood as a more precise solution of the same model physics that the integral model uses. Hence, it is suitable to verify the assumptions made in the context of the integral model.

The obvious disadvantage of this modeling approach is its extreme numerical effort. Due to the fine discretion of space, its system of differential equations is significantly larger than the one of the integral model. Hence, its solution is more time consuming, which hinders its direct implementation into severe accident analysis codes.

8. Verification

Both the integral model and the spatially discretized model, which were presented in Chapters 6 and 7, respectively, must be verified in order to check the physical laws for the representation of heat and mass transport for their correct implementation. For this purpose, this work uses a comparison to analytical solutions of simplified heat or mass transfer problems with moving phase boundaries (here, the «or»is exclusive). Suitable solutions for such so-called two-phase Stefan problems can be found in the literature (see, for example, Dantzig and Rappaz [38]). Analytical solutions for coupled heat and mass transport problems, which include chemical reactions, are not known.

In this chapter, analytical solutions are derived for a two-phase isothermal mass transport problem in a binary system and for a solidification problem in a unary system, following the work of Dantzig and Rappaz [38]. This brief digression is made since the analytical solutions can be obtained through the continuation of the derivation of the parabolic rate equations, which was started in Section 3.1. Furthermore, this process substantiates the understanding of the connection of all diffusion models used in this work. Thereafter, the numerical models are compared to these analytical solutions and, in this way, are verified with the help of two invented model cases.

8.1. Analytical solutions for two-phase Stefan problems

The derivation of an analytical solution for the isothermal mass transport problem shows a strong analogy to the derivation of the parabolic rate laws (see Section 3.1). First, a semi-infinite isothermal medium consisting of metallic zirconium is assumed, which obtains a homogeneous oxygen concentration. This medium is in contact with a steam-containing environment and, therefore, causes the formation of an oxide scale. Therefore, a model with two zones, oxide and metal, which are separated by a sharp phase interface is considered. At this phase boundary, both phases are in local thermodynamic equilibrium. This system is illustrated in Fig. 3.1.

Thus, the analytical solution builds on Eq. 3.2 to Eq. 3.12 from Section 3.1, and it continues at the point where it becomes necessary to determine the constants $\hat{A}_I$ and $\hat{B}_I$ for the oxygen concentration profile of the oxide and the constants $\hat{A}_{II}$ and $\hat{B}_{II}$ for the concentration profile of the metal. To determine $\hat{A}_I$ and $\hat{A}_{II}$, the initial and boundary conditions are inserted into Eq. 3.11 and Eq. 3.12.

$$x = 0 : \rho_{OI}(x,t) = \hat{A}_I + \hat{B}_I erf\left(\frac{x}{2\sqrt{D_{O_I}t}}\right) = \rho_{OI,surf.} \Rightarrow \hat{A}_I = \rho_{OI,surf.} \tag{8.1}$$

$$x \to \infty : \rho_{OII}(x,t) = \hat{A}_{II} - \hat{B}_{II} erfc\left(\frac{x}{2\sqrt{D_{O_{II}}t}}\right) = \rho_{OII,0} \Rightarrow \hat{A}_{II} = \rho_{OII,0} \tag{8.2}$$

At the common interface of both phases, the following equations apply accordingly:

$$x = x^* : \rho_{OI}(x^*,t) = \rho_{OI,surf.} + \hat{B}_I erf\left(\frac{x^*}{2\sqrt{D_{O_I}t}}\right) = \rho_{OI}^* \tag{8.3}$$

$$x = x^* : \rho_{OII}(x^*,t) = \rho_{OII,0} - \hat{B}_{II} erfc\left(\frac{x^*}{2\sqrt{D_{O_{II}}t}}\right) = \rho_{OII}^* \tag{8.4}$$

With the exception of the argument of the error function, all the terms of these equations are constants. Therefore, Eq. 8.3 and Eq. 8.4 can only be satisfied if x^* itself is a function of the square root of time t. For this reason, the movement of the phase interface can be expressed by a factor Ψ that must be multiplied with the square root of time t. This is shown as follows:

$$x^*(t) = 2\Psi\sqrt{D_I t} \tag{8.5}$$

A time derivative of the same equation is:

$$\frac{x^*}{dt} = \Psi\frac{\sqrt{D_I}}{\sqrt{t}} \tag{8.6}$$

In the next step, Eq. 8.5 is used to derive the constants $\hat{B}_I$ and $\hat{B}_{II}$ through the evaluation of the equation of the concentration profile of the oxide (Eq. 8.3) and of the equation of the concentration profile of the metal (Eq. 8.4) at the position of the phase interface:

$$\rho_{OI}(x^*,t) = \rho_{OI,surf.} + \hat{B}_I erf\left(\frac{2\Psi\sqrt{D_{O_I}t}}{2\sqrt{D_{O_{II}}t}}\right) = \rho_{OI}^* \Rightarrow \hat{B}_I = \frac{\rho_{OI}^* - \rho_{OI,surf.}}{erf(\Psi)} \tag{8.7}$$

$$\rho_{OII}(x^*,t) = \rho_{OII,0} - \hat{B}_{II} erfc\left(\frac{2\Psi\sqrt{D_{O_I}t}}{2\sqrt{D_{O_{II}}t}}\right) = \rho_{OII}^* \Rightarrow \hat{B}_{II} = \frac{\rho_{OII,0} - \rho_{OII}^*}{erfc\left(\Psi\sqrt{\frac{D_{O_I}}{D_{O_{II}}}}\right)} \tag{8.8}$$

Thus, the concentration profiles are completely described by the following equations:

$$\rho_{O_I}(x,t) = \rho_{O_{I,surf.}} + \frac{\rho_{O_I}^* - \rho_{O_{I,surf.}}}{erf(\Psi)} erf\left(\frac{x}{2\sqrt{D_{O_I}t}}\right) \tag{8.9}$$

$$\rho_{O_{II}}(x,t) = \rho_{O_{II,0}} - \frac{\rho_{O_{II,0}} - \rho_{O_{II}}^*}{erfc\left(\Psi\sqrt{\frac{D_{O_I}}{D_{O_{II}}}}\right)} erfc\left(\frac{x}{2\sqrt{D_{O_{II}}t}}\right) \tag{8.10}$$

If both equations describing the concentration profiles are inserted into the moving boundary condition (i.e., the Stefan condition shown in Eq. 3.6), the constant Ψ can be determined using an iterative scheme.

$$0 = \left(\rho_{O_I}^* - \rho_{O_{II}}^*\right)\Psi\sqrt{\pi} + \left(\rho_{O_I}^* - \rho_{O_{I,surf.}}\right)\frac{exp\left(-\Psi^2\right)}{erf(\Psi)} - \left(\rho_{O_{II,0}} - \rho_{O_{II}}^*\right)\sqrt{\frac{D_{O_{II}}}{D_{O_I}}}\frac{exp\left(-\Psi^2\frac{D_{O_I}}{D_{O_{II}}}\right)}{erfc\left(\Psi\sqrt{\frac{D_{O_I}}{D_{O_{II}}}}\right)} \tag{8.11}$$

Here, the derivative of the error function must be adhered:

$$\frac{\partial erf(\Psi)}{\partial x} = \frac{2}{\sqrt{\pi}} exp\left(-\Psi^2\right)\frac{\partial\Psi}{\partial x} \tag{8.12}$$

The analytical solution is, therefore, described by the equations of the concentration profiles Eq. 8.9 and Eq. 8.9, in which the iterated solution of Eq. 8.11 is inserted.

In analogy to the analytical solution for the mass transfer problem, the solution for the solidification problem can be derived under similar assumptions. The derivation will be omitted at this point and, instead, reference is made to Dantzig and Rappaz [38]. To describe the temperature profiles, the analytical equations that are required are the following:

$$T_I(x,t) = T_{I,surf.} + \frac{T^* - T_{I,surf.}}{erf(\Psi)} erf\left(\frac{x}{2\sqrt{a_I t}}\right) \tag{8.13}$$

$$T_{II}(x,t) = T_{II,0} - \frac{T_{II,0} - T^*}{erfc\left(\Psi\sqrt{\frac{a_I}{a_{II}}}\right)} erfc\left(\frac{x}{2\sqrt{a_{II}t}}\right) \tag{8.14}$$

where a is the thermal diffusivity. In this case, the proportionality constant Ψ can be calculated using the following expression:

$$0 = \frac{L_f}{c_{p,I}} \Psi \sqrt{\pi} + (T^* - T_{I,surf.}) \frac{exp\left(-\Psi^2\right)}{erf(\Psi)} - (T_{II,0} - T^*) \sqrt{\frac{a_{II}}{a_I}} \frac{exp\left(-\Psi^2 \frac{a_I}{a_{II}}\right)}{erfc\left(\Psi \sqrt{\frac{a_I}{a_{II}}}\right)} \tag{8.15}$$

8.2. Mass transport models

As a first step, the mass transport models of the integral model and the spatially discretized model are to be verified. For this purpose, an invented model case for an isothermal mass transport problem involving a change of phase is precalculated using the analytical solution and, in turn, is simulated using numerical models. As the analytical solution requires the temporal constancy of the material properties, transport properties, and boundary conditions, the materials databases of the numerical models are switched off and the corresponding properties are set as constant in order to ensure comparability.

The test case for the isothermal mass transport problem involving a chemical phase transition builds on the following initial and boundary conditions, which refer to a temperature of $2650\,K$:

$$x_{OI,surf.} = 0.666, \;\; x = 0 \tag{8.16}$$

$$x_{OII,0} = 0.000, \;\; x \rightarrow -\infty \tag{8.17}$$

$$x_{OI}^* = 0.619, \;\; x = x^*(t) \tag{8.18}$$

$$x_{OII}^* = 0.548, \;\; x = x^*(t) \tag{8.19}$$

$$x^*(t = 0) = 0 \tag{8.20}$$

$$x_{OII}(t = 0) = x_{OII,0} \tag{8.21}$$

The modeling is completed by auxiliary information regarding the densities and diffusion coefficients, which are summarized in Table 8.1:

Table 8.1.: Auxiliary input used to verify the mass transfer models.

	Liquid metal	Solid oxide
D_O	$2.79 \cdot 10^{-9}\,\frac{m^2}{s}$	$4.66 \cdot 10^{-8}\,\frac{m^2}{s}$
ρ	$6107\,\frac{kg}{m^3}$	$5780\,\frac{kg}{m^3}$

Since the modeling of semi-infinite geometries is not feasible using the numerical models, the systems' geometries are modeled sufficiently large in order to exclude the occurrence of boundary effects during the simulation time of $2000\,s$.

In Fig. 8.1 the analytical solution (solid lines) and numerical solutions of the integral model (dash-dotted lines) and the spatially discretized model (dashed lines) are compared. In this context, Fig. 8.1 presents the temporal evolution of the oxygen concentration profiles and the movement of the phase interface between oxide and metal. To achieve comparability to the phase diagrams, the concentration profiles are plotted with the help of the oxygen molar fraction x_O instead of the mass concentration ρ_O. This procedure is retained in all subsequent chapters. As can be seen, the solutions of the analytical solution (solid lines) and the spatially discretized model (dashed lines) almost match. Leaps in the concentration profiles indicate the position of the phase interfaces. Since the integral model does not resolve the spatial concentration profile, its solution (dash-dotted lines) only indicates the position of the interface after a certain time and is depicted with the help of vertical lines. As can be seen, both numerical models can reproduce the analytical solution in qualitative and quantitative agreement.

8.3. Heat transport models

In the second step, the heat transport models are verified. In the case of the spatially discretized model, it is possible to verify the equations implemented to simulate the heat transport at their full extent. In contrast, the advanced integral model cannot be verified in this regard since its heat transfer model does not include a moving boundary condition to model's thermally-induced phase changes. Nevertheless, in the further course of this work, its correctness is ensured indirectly by comparison with the verified spatially discretized model.

The model case for the verification of the heat transfer model of the spatially discretized model is a two-phase solidification problem in a unary system. This test case uses the

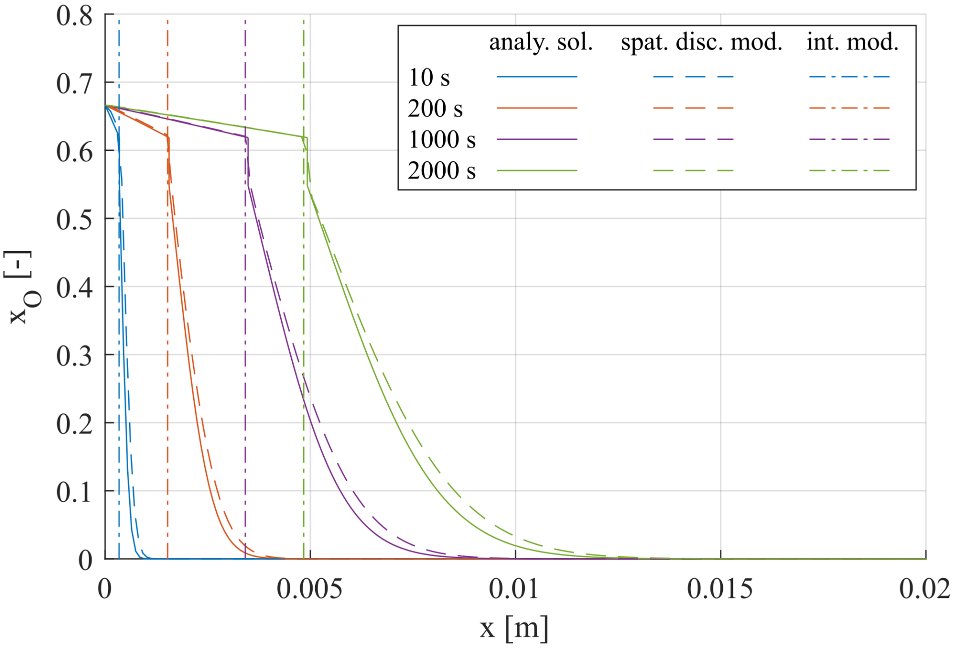

Figure 8.1.: Temporal evolution of oxygen concentration profiles (expressed via the oxygen molar fraction x_O) and movement of the phase interface (oxide-metal) as calculated with the help of an analytical solution, the advanced integral model and the spatially discretized model.

following initial and boundary conditions, which refer to a system consisting of pure zirconium:

$$T_{I,surf.} = 2000\,K,\ \ x = 0 \tag{8.22}$$

$$T_{II,0} = 2300\,K,\ \ x \rightarrow\ -\infty \tag{8.23}$$

$$T_I^* = T_{II}^* = T^* = 2128\,K,\ \ x = x^*(t) \tag{8.24}$$

$$x^*(t=0) = 0 \tag{8.25}$$

$$T_{II}(t=0) = T_{II,0} \tag{8.26}$$

Table 8.1 provides information regarding the densities and thermal conductivities used in these simulations, and which were determined with the aid of the materials and transport properties' database. The table also offers information regarding the heat capacities and the enthalpy of fusion that were extracted from the lookup table, and which were used in the simulations. As in the previous case, all boundary conditions and all material and transport properties were set constant. The simulations were initialized with large zirconium bodies to ensure that no boundary effects occur.

Table 8.2.: Auxiliary input used to verify the heat transfer models.

	Liquid metal	Solid oxide
λ	$36.50\,\frac{W}{mK}$	$36.75\,\frac{W}{mK}$
ρ	$6107\,\frac{kg}{m^3}$	$6192\,\frac{kg}{m^3}$
c_p	$0.463\,\frac{kJ}{kgK}$	$0.379\,\frac{kJ}{kgK}$
ΔH_{fusion}	$228.48\,\frac{kJ}{kg}$	

In Fig. 8.2, the simulation results obtained with the help of the analytical solution (solid line) and by means of the spatially discretized model (dashed lines) are compared. The change in the slope of the temperature profile at $2128\,K$, as observed in the analytical solution, marks the position of the phase interface. As can be seen, the spatially discretized model shows a slight difference in the reproduction of this phase change. This difference results from the interpolation scheme of the lookup table, which stretches this transition over a temperature band of $25\,K$. Nonetheless, qualitative and quantitative agreement can be attested, which means that, consequently, the correct implementation of both the heat and oxygen mass transport equations can be confirmed.

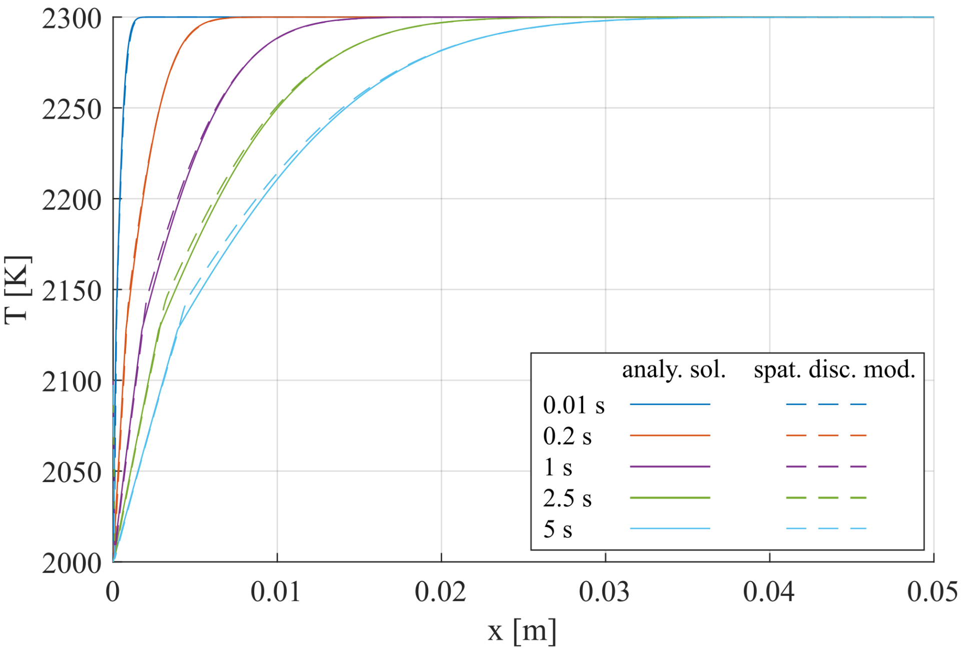

Figure 8.2.: Temporal evolution of temperature profiles and movement of the phase interface (solid-liquid), as calculated with the help of the analytical solution and the spatially discretized model.

8.4. Cell number dependency

In Sections 8.2 and 8.3, the implicit assumption was made that the number of cells in the spatially discretized model is sufficiently large to resolve the heat and mass transport processes correctly. Nevertheless, the use of a spatially discretized model requires an investigation of the dependency of its solution on the spatial resolution. In this way, it is possible to determine the influences of its spatial grid on the temperature and concentration profiles, and a minimum cell number can be defined in order to exclude adverse effects.

To investigative this parameter, an isothermal mass transport problem is considered, the initial and boundary conditions of which resemble the example from Section 8.2 (Eq. 8.16 to Eq. 8.21). However, in this context, a $1\,mm$ thick slab is assumed and the oxidation reaction is followed to a time of $10\,s$, at which the oxidation reaction is almost completed (see Fig. 8.1). The analytical model provides a reference solution. The solution of the spatially discretized model is investigated using spatial grids with 10, 100, and 1000 cells, which correspond to initial cell widths of $100\,\mu m$, $10\,\mu m$, and $1\,\mu m$. The results of the comparison are presented in Fig. 8.3.

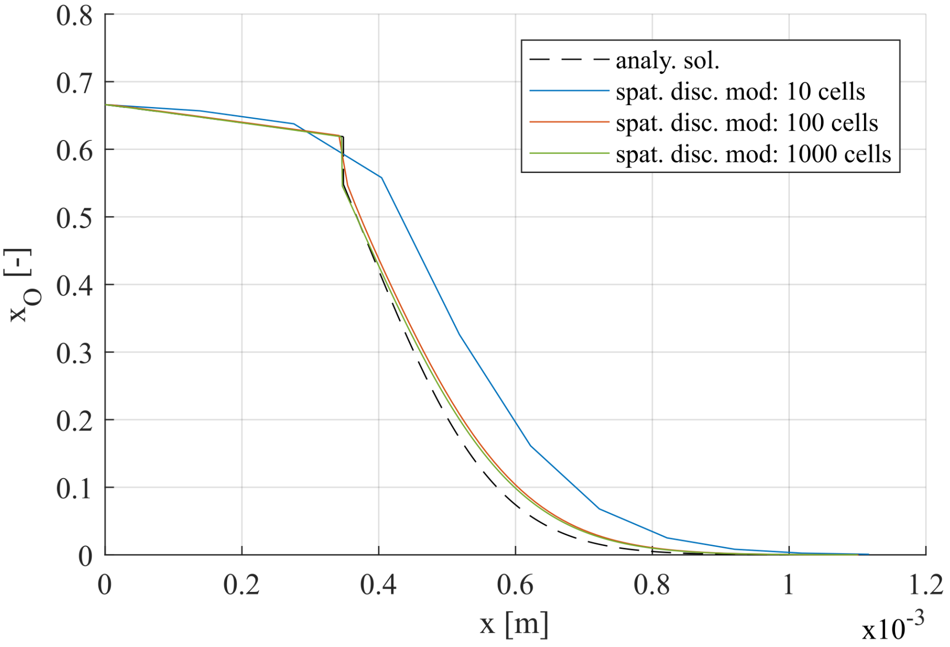

Figure 8.3.: Comparison of simulation results for calculations with the spatially discretized model using different cell numbers.

Fig. 8.3 shows that the solution with 10 cells (blue line) strongly differs from the analytical solution (dashed black line). Hence, this coarse grid is not suitable to map the concentration profile and the position of the phase interface correctly. In contrast, the solutions with 100 and 1000 cells (red and green lines) match the analytical solution well and even converge.

Furthermore, the model with 100 cells calculates the position of the phase interface (as the anchor point of the concentration profile) with an accuracy of $10\,\mu m$, and its concentration profile almost matches the solution obtained with 1000 cells.

After all, it has to be considered that each increase in the number of cells leads to a significant increase in the computation time and amplifies numerical instabilities. Thus, the choice of a reasonable cell number is an optimization problem in which an improved resolution has to be balanced against the abovementioned disadvantages. For the purpose of this thesis, a resolution of $10\,\mu m$ was sufficient to resolve the concentration and temperature profiles, as well as the positions of phase boundaries. Therefore, in the further course of this work, all models are initialized with a cell width of $10\,\mu m$.

9. Model comparisons

Various experiments elucidate the oxygen transport in samples that are made from zirconium and its alloys under isothermal conditions. However, there is a significant lack of single-effect experiments that provide simultaneous insight into the oxygen transport and its related heat effects under temperature transient conditions (see Chapter 3.3). Hence, to test the capabilities of the advanced integral model presented in this work and to demonstrate the advances achieved, the model must be compared with other numerical models.

In this chapter, the proposed advanced integral model (see Chapter 6 is compared to models from the literature, as well as models currently implemented in severe accident analysis codes. In the first section, a simple test case with clearly defined initial and boundary conditions is precalculated with the help of the spatially discretized model, enabling the solution to be used as a reference in a subsequent model comparison. Without the disturbing influences of other models, general differences in the solutions of the different approaches can be clearly identified. The second section of this chapter uses the real output from a simulation in ATHLET-CD in order to supply the advanced integral model with time-varying boundary conditions and, in this way, to simulate its implementation into a severe accident code. The secondary aim of this test is to compare the advanced integral model to the parabolic rate equation-based model implemented in the ATHLET-CD oxidation model. Once the equality of the advanced integral model compared to state-of-the-art modeling approaches has been demonstrated, the next chapter, Chapter 10, demonstrates its capabilities. Noteworthily, these go beyond the current state of the art, especially in terms of the model's ability to capture thermally-induced phase changes.

9.1. Comparison to models from the literature

The first comparison builds on two modeling approaches available from the literature, both of which are suitable for an application in severe accident analysis codes. The first is a model based on parabolic rate equations, which is described in Appendix A. This model assumes a uniform temperature within the sample and is extended by a simple energy balance in order to ensure a temperature feedback. Its approach resembles the state of the art in the modeling of oxygen transport in severe accident analysis codes. The second model is a modified version of the integral approach developed by Veshchunov et al. [7], the key features of which were presented in Section 3.2. It is an integral model applicable to predefined phase transitions and, therefore, to limited temperature ranges, whose thermodynamic data is supplied in the form of constants and equations. Both models are incapable of simulating thermally-induced phase transitions.

Model case

The test case designed for the first model comparison is inspired by experimental results indicating that the late quenching of degraded core structures is associated with a sharp increase in hydrogen and heat generation (see, for example, QUENCH-09 [54]). This effect is caused by the dissolution of the oxide scale under steam-starved conditions, which entails the loss of its protective function [19]. Today's severe accident analysis codes, which commonly rely on oxidation models based on parabolic rate equations, struggle to reproduce this phenomenon.

The test system consists of a slab with a thickness of $1\,mm$, the body of which consists of oxygen-free zirconium, and which is covered by an oxide scale of $10\,\mu m$ consisting of $ZrO_{1.86}$. This slab is one-sidedly exposed to the environment, the varying steam content of which causes the sequence of three phases defined by changing boundary conditions for the oxygen transport:

Phase 1: $0\,s$ to $60\,s$: Unlimited steam supply (Dirichlet condition: stoichiometric ZrO_2 at oxide's surface)

Phase 2: $60\,s$ to $600\,s$: Full cut of the steam supply (Neumann condition: no further oxygen uptake)

Phase 3: $600\,s$ to $900\,s$: Unlimited steam supply (Dirichlet condition: stoichiometric ZrO_2 at oxide's surface)

Initially, both the slab and the environment are at a temperature of $1873\,K$. During the whole test, the environment's temperature remains constant at $1873\,K$, meaning that it takes the effect of an unlimited heat sink. The heat transfer coefficient between the slab and environment is set constantly to $1000\,\frac{W}{m^2K}$. The chemical dissolution of water vapor into oxygen and hydrogen is regarded as another heat sink. An unscaled depiction of this model system is given in Fig. 9.1.

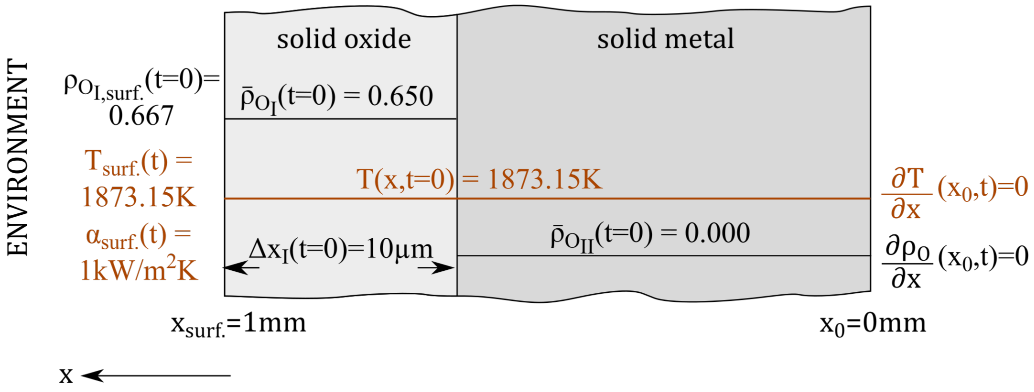
ENVIRONMENT
solid oxide
solid metal
$\rho_{O_{I,surf.}}(t=0)=$ 0.667
$\bar{\rho}_{O_I}(t=0) = 0.650$
$T_{surf.}(t) =$ 1873.15K
$T(x,t=0) = 1873.15K$
$\alpha_{surf.}(t) =$ 1kW/m²K
$\Delta x_I(t=0)=10\mu m$
$\bar{\rho}_{O_{II}}(t=0) = 0.000$
$\frac{\partial T}{\partial x}(x_0,t)=0$
$\frac{\partial \rho_O}{\partial x}(x_0,t)=0$
$x_{surf.}$=1mm
x_0=0mm
x

Figure 9.1.: Unscaled sketch of the model system with initial and boundary conditions at $t = 0$.

Model test

Fig. 9.2 shows the spatial profile and temporal development of the oxygen molar fraction, as obtained using the spatially discretized model (100 cells). The oxidation in phase 1 leads to the formation of three distinct phases, which are separated by sharp interfaces defined by leaps in the concentration profile. Those phases are the oxidic scale (β-ZrO$_2$ and γ-ZrO$_2$), metallic α-Zr, and metallic β-Zr. Consistent with the related parabolic kinetics, the oxidation rate decreases with time as the thickness of the oxide increases. The mass gain results in an extension of the slab's thickness. The molar oxygen fraction x_O at the location $x = 0$ begins to increase from the outset ($t = 0\,s$), which means that the assumption of a semi-infinite body of virgin zirconium, as used in a parabolic rate equations, would immediately be violated. With the change to steam-starved conditions in phase 2, the previously formed oxide scale recedes and even vanishes at approximately 590 s. From that point on, metallic α-Zr is exposed to the ambient. Simultaneously, the mass transport between α-Zr and β-Zr resumes and results in the consumption of the β-Zr phase. In phase 3, the restarted oxidation leads to a sharp increase in oxygen uptake and the formation of a fresh oxide scale. The β-Zr phase is completely consumed after approximately 890 s.

Fig. 9.3 presents the corresponding temporal evolution of the temperature profile. To begin with, its most striking feature, which is the spatial temperature differences within the sample, are generally found to be less than 5 K. Due to the high oxidation rate at the start of phase 1, the temperature profile exhibits a sharp temperature peak of 2084 K at 5 s. From that point on, the gradual decrease of oxygen uptake leads to a decrease in temperature. With the discontinuation of oxygen uptake in phase 2, the temperature rapidly drops but remains slightly higher than the ambient level. This effect can be

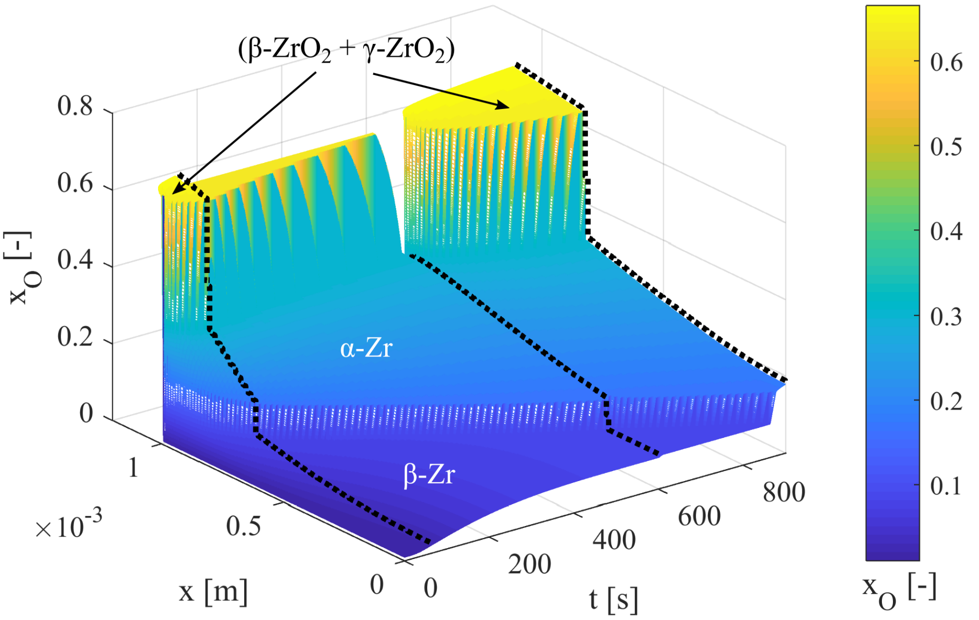

Figure 9.2.: Temporal evolution of the concentration profile (expressed via the oxygen molar fraction x_O), as calculated using the spatially discretized model.

explained by the continuing oxygen transport within the sample. In phase 3, the restarted oxidation causes another 2001 K peak in the temperature profile at 603 s.

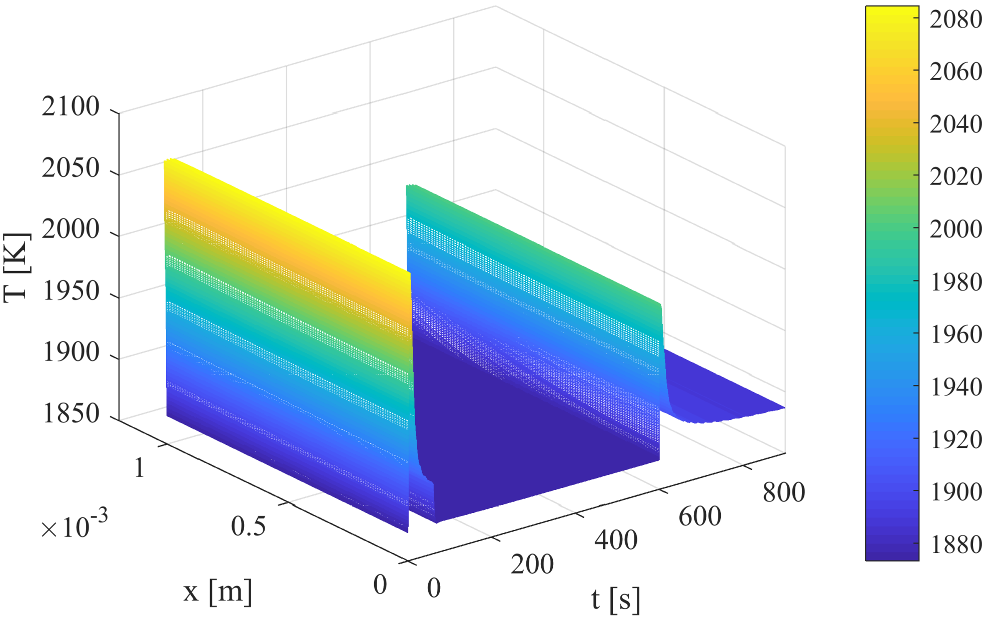

Figure 9.3.: Temporal evolution of the temperature profile as calculated using the spatially discretized model.

Fig. 9.4 shows a comparison of the aforementioned modeling approaches with regard to the spatial and temporal expansion of the different phases resulting from the oxygen transport. Fig. 9.5 and Fig. 9.6 illustrate the corresponding temperature changes. Since the spatial temperature gradients in the 1 mm slab have been found to be negligible, each model is presented with an average temperature. For the sake of clarity, Fig. 9.5 zooms in on the temperature peak at the beginning of phase 1 and Fig. 9.6 at the beginning of phase 3. Fig. 9.7 shows the integral of hydrogen generation as a measure of the total oxygen uptake of the sample.

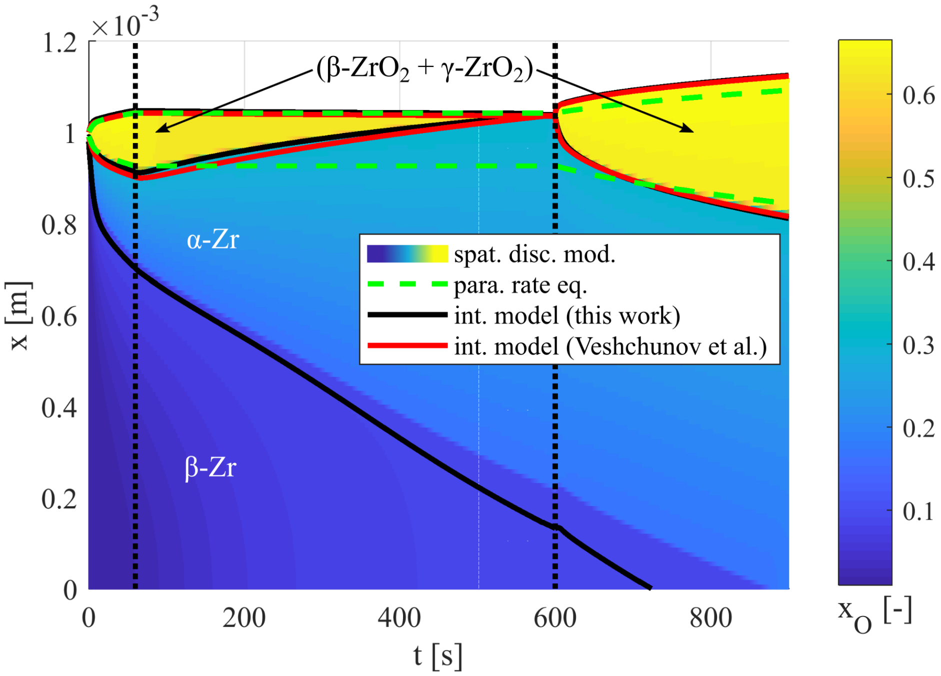

Figure 9.4.: Comparison of the progression of phase interfaces, as calculated by means of different models from the literature.

The simulation results obtained with the model based on parabolic rate equations (dashed green lines) match those of the spatially discretized model regarding the formation of the oxidic scale in phase 1. Both solutions also converge concerning the overall evolution of the temperature in phase 1, despite the fact that the peak value of the model, which is based on parabolic rate equations, is significantly higher (2138 K at 5 s). Since rate equations are incapable of capturing steam-starved conditions, the chemical reaction must be assumed to be on hold in phase 2. Hence, the thickness of the oxide scale remains constant and the temperature drops rapidly to the ambient level. In phase 3, the chemical reaction ties up on its level at the end of phase 1, whereby the unaltered presence of the thick oxide scale causes a retardation of the oxygen uptake. Therefore, the oxidic scale subsequently becomes comparably slow, and a temperature peak does not evolve. Along the same lines, a sharp increase in the hydrogen mass is not predicted by the model based on parabolic rate equations. As a result, from phase 3 onward, the hydrogen mass is significantly lower than the mass predicted by the spatially discretized one-dimensional model (see Fig. 9.7).

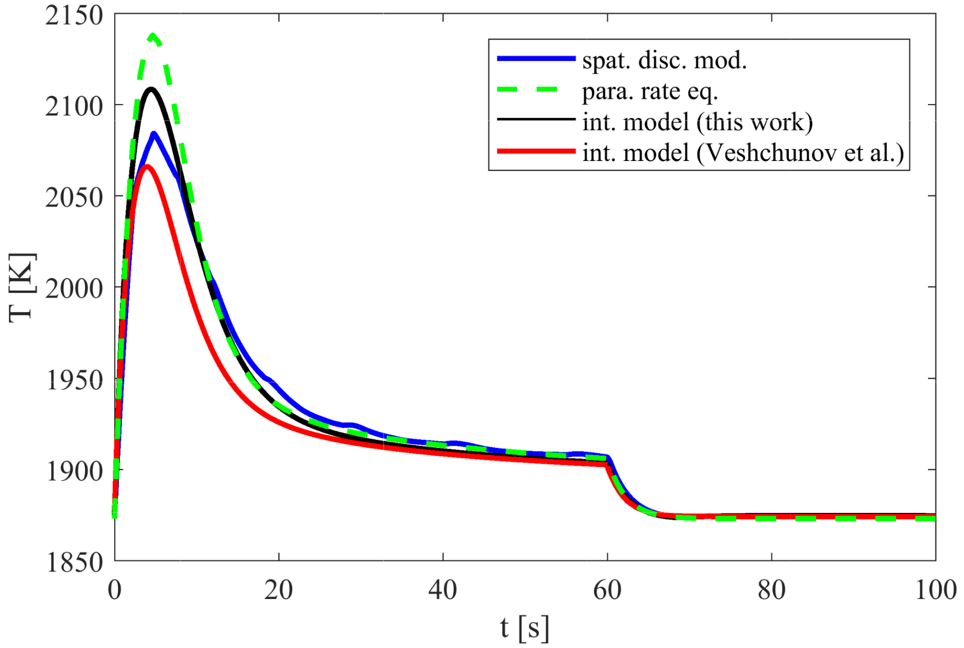

Figure 9.5.: Comparison of the temperatures (sample-averaged), as calculated by means of different models from the literature for the time between 0 s and 100 s.

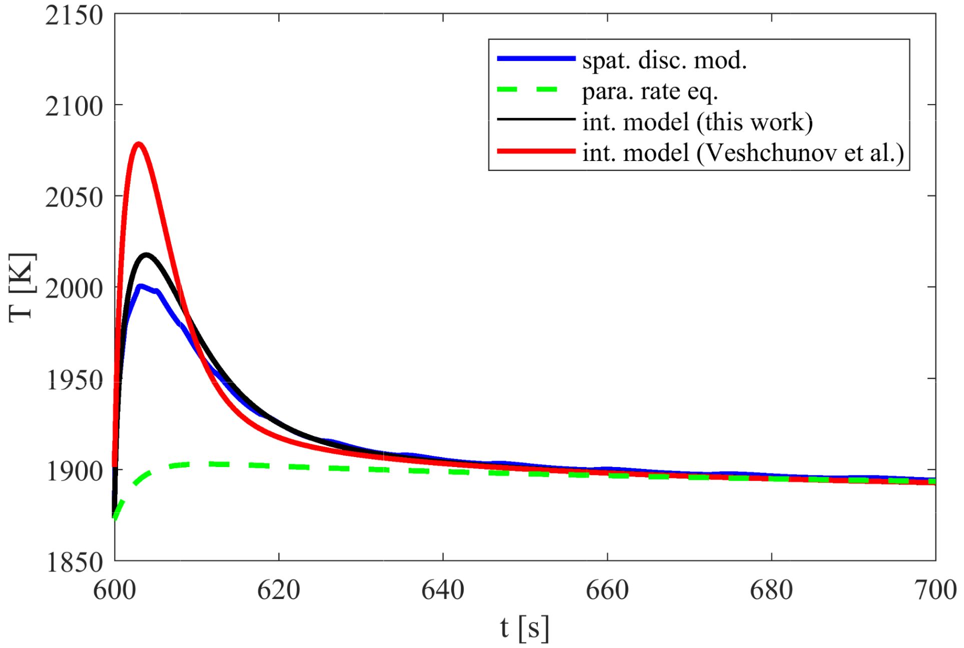

Figure 9.6.: Comparison of the temperatures (sample-averaged), as calculated by means of different models from the literature for the time between 600 s and 700 s.

Throughout all phases of the model case, the results obtained with the advanced integral model (solid black lines) regarding both the growth and shrinkage of the oxide scale are in agreement with the solution of the spatially discretized model (note that the oxide

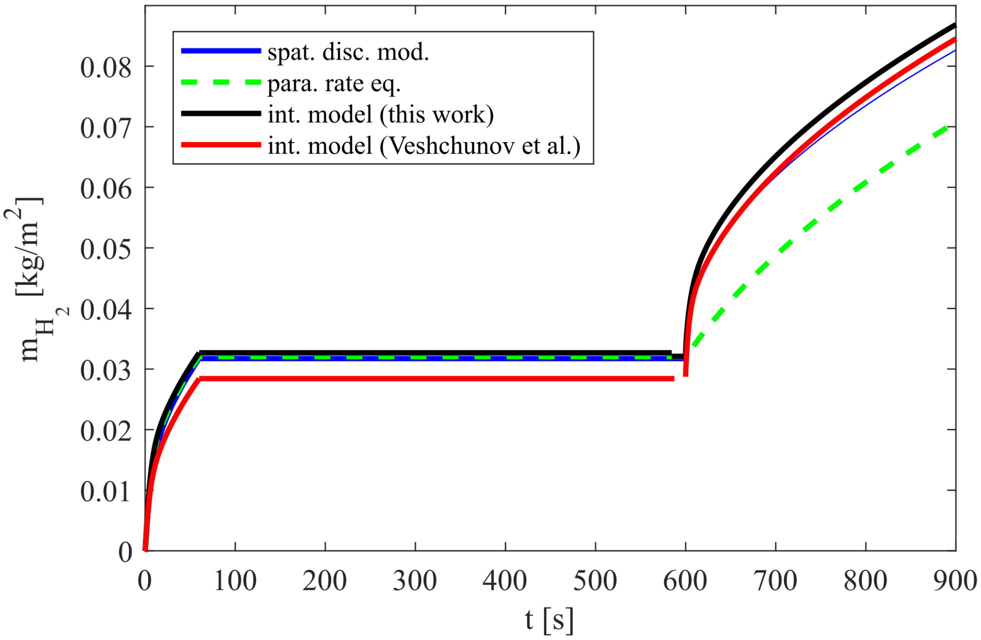

Figure 9.7.: Comparison of the simulation results regarding the total oxygen uptake expressed via the generated hydrogen mass.

scale in phase 3 has been initialized with a thickness of $2\,\mu m$ in both integral models). Quantitative differences are only observed regarding the consumption of the β-Zr phase by α-Zr, whose completion is predicted in a shorter time ($723\,s$). The temporal temperature profile matches qualitatively. The maximum temperature value in phase 1 lies between the solutions of the spatially discretized model and the model based on rate equations ($2109\,K$ at $4\,s$). The peak temperature in phase 3 ($2018\,K$ at $604\,s$) is close to the solution obtained with the spatially discretized model. Analogously, the sharp increase in hydrogen generation is captured in strong resemblance to the reference solution.

The integral model from the literature (red lines) captures both the growth and shrinkage of the oxide equally effectively, but it summarizes α-Zr and β-Zr into a single zone. The temperature evolution also matches qualitatively. Here, the differences mainly relate to the peak temperatures. The value for phase 1 ($2066\,K$ at $4\,s$) is the lowest of all values calculated for this phase. In contrast, the value for phase 3 ($2079\,K$ at $603\,s$) is the highest, and different from any other model, even higher than the model's prediction for phase 1. The hydrogen mass calculated for phases 1 and 2 is slightly lower than in the other models, which is an indicator for a lower total oxygen uptake. Nevertheless, the sudden increase in hydrogen generation at the beginning of phase 3 is captured in accordance with the spatially discretized model and the advanced integral model developed in this work.

All models are in relative agreement concerning both the progress of the chemically-induced phase transitions and thermal kinetics in the first stage of the model case. The model based on parabolic rate laws, however, lacks the capability to account for the retreat of the oxide under the condition of steam starvation, which is a weakness intrinsic to its approach. Therefore, it would provide imprecise results from the start of phase 2 onward, and most importantly, would not indicate the strengthening in the chemical reaction at the beginning of phase 3. Both integral models remedy this effect and agree well with the spatially discretized model regarding the simulated evolution of phases over the full sequence of test phases. Hence, the model comparison vividly demonstrates the strengths of the integral approach, which delivers more precise results compared to parabolic rate equations whilst requiring significantly less computational resources than the spatially discretized model. Under the given test conditions, both the integral model from literature and the proposed advanced integral model would provide similar results. However, it should again be emphasized that the model from the literature cannot simulate thermally-induced phase transitions.

9.2. Comparison to models implemented into ATHLET-CD

In the previous section, a comparison was presented of models from the literature and the model developed within the framework of this thesis. For the sake of clarity, the initial and boundary conditions chosen for this comparison have been simple. In this section, such a comparison is drawn on the basis of a more complex model case, which simulates an application of the advanced integral model to a severe accident analysis code. For this purpose, the simulation results of an exemplary severe accident are used, which were calculated by Trometer [55] with the accident analysis code ATHLET-CD, and which are readily available. These simulation results offer an insight into the temporal development of important environmental parameters in the course of an exemplary accident. Therefore, it is possible to use these parameters as boundary conditions for the advanced integral model in order to investigate its response to complex, transient boundary conditions.

To facilitate this comparison, a two-step method is deployed. In the first step, the oxidation reaction is recalculated with the aid of a model, which, like the oxidation models in ATHLET-CD, is based on a parabolic rate approach. However, it uses a considerably simplified heat transfer model (see Appendix A). In turn, these calculation are used to define a reference state for the further investigation. In the second step, the oxidation reaction is simulated by means of the advanced integral model and the spatially discretized model, which also make use of the aforementioned simplified heat transfer model. As a consequence of this unification process, differences in the simulation results can be identified that result exclusively from the conceptually different approaches used to model the chemical processes.

The aim of this section is to quantify these differences in simulations with complex and temporally volatile boundary conditions. In this context, the spatial extension of the different phases is the primary investigation parameter. In addition, the temporal development of the total oxygen uptake, here expressed via the integral of the formed hydrogen mass, and the temporal evolution of the cladding tube temperatures are investigated.

Description of modeling in ATHLET-CD and model case

The data basis for the following investigation consists of existing simulation results from an example accident, which was calculated using the accident analysis code ATHLET-CD (version 3.0A) by Trometer [55]. A comprehensive description of the severe accident analysis code ATHLET-CD and of the model case, hereinafter referred to as «base case», is given in [55]. At this point, only a brief overview over the general aspects of the modeling in ATHLET-CD, the assumed accident conditions, and its temporal evolution is to be given.

In ATHLET-CD, larger space units and structures are subdivided into smaller geometric units known as «nodes», which is a common approach for severe accident analysis codes. In the work of Trometer [55], the essentially cylindrical core of a pressurized water reactor is radially divided into six concentric rings, so-called «core channels» (outermost core radius: $2.03\,m$). The physical and chemical processes in these core channels are modeled with the help of representative fuel elements and cooling channels, whose interactions are scaled up to represent the corresponding geometric region of the core. To improve the resolution of local effects, each core and cooling channel is further subdivided into smaller substructures in the axial direction. In Trometer [55], the $4.428\,m$ long fuel rods are divided axially into 22 nodes, while the $6.375\,m$ long cooling channels are divided axially into 26 nodes.

In ATHLET-CD, the oxidation of the cladding tubes of fuel and control rods is modeled using a parabolic rate approach. Trometer [55] selected the correlation of Cathcart and Pawel for the temperature range from $1273\,K$ to $1800\,K$, as well as the correlation of Urbanic and Heidrick between $1900\,K$ and $2100\,K$. Between $1800\,K$ and $1900\,K$, the oxidation rates are interpolated, while beyond $2100\,K$, they are extrapolated. In her input, Trometer further specified that a slowdown of the oxidation reaction due to a limited steam availability does not occur until the relative steam fraction is less than $10\,\%$. Furthermore, it should be noted that in ATHLET-CD, the modeling of the oxidation reaction in a node is stopped as soon the melting of the cladding material sets in, and the subsequent oxidation of liquid phases is not considered. Regarding the melting of the cladding tube material, it is specified that α-Zr melts at $2250\,K$, β-Zr at $2033\,K$, and oxidic material at $2600\,K$. Concentration-dependent changes in the melting points are not considered.

The severe accident simulated by Trometer [55] is a medium-sized loss-of-coolant accident (MBLOCA), which develops into a beyond-design-basis accident due to an extremely unfavorable concatenation of system failures. The event is caused by a $200\,cm^2$ leak in the hot leg of the primary cooling circuit of a pressurized water reactor near the surge line of the pressurizer. As a result, the entire coolant inventory of the pressurizer is immediately emptied into the leak and the water supply via the pressurizer's spray line becomes ineffective. Subsequently, the emergency systems of the reactor start to inject water via high and low pressure emergency cooling systems and from the hydro-accumulators (availability: $50\,\%$) into the primary cooling circuit. It is assumed that these systems function properly until their water reservoirs are exhausted. Subsequently, a failure of sump cooling is assumed so that the water that is lost through the leak cannot return to the cooling circuit. Regarding the secondary cooling circuit, it is assumed that the cooling of the steam generators fails as well, so that the ultimate heat sink is no longer effective. As a result, the core is completely cut from coolant and no heat sink is available in the long term.

Due to the multiple failures of diversified safety systems that feature in this scenario, it is unlikely to occur in the real-world and exceeds the scenarios considered in the German Risk Study B in terms of their severity [56]. However, it favors a very rapid onset of the high-temperature oxidation of zirconium and core melting. Therefore, it is especially suitable for the intended comparison of different oxidation models. In the scenario, the following key events occur:

- $53\,min$ ($3157\,s$) after break opening: onset of core uncovery
- $90\,min$ ($5410\,s$)after break opening: start of zirconium oxidation
- $99\,min$ ($5951\,s$) after break opening: start of core melting
- $144\,min$ ($8669\,s$) after break opening: core uncovery is completed

For the comparative investigation of the oxidation models, two nodes were extracted from the simulation output of the base case. The first case describes the complete oxidation of the cladding tube material in one node, whereas the second case illuminates the partial oxidation of the fuel rod cladding tube in another node, which includes a temporary phase of steam starvation and ends with its melting.

Input, pre-oxidation, and simplified heat transfer model

To achieve the high comparability of the simulations based on the individual modeling approaches, which contrast significantly, it is necessary to provide uniform inputs regarding the material and transport properties. A uniform simplified heat transfer model is also required, which uses the simulation results of the base case as boundary conditions.

The input for the simulations is defined based on the descriptions given in Chapters 4 and 5. Consistent with Trometer's use of parabolic rate constants from Urbanic and Heidrick in [28], a diffusion coefficient from [6] is used, which emulates their kinetics.

In ATHLET-CD, the oxidation model is started as soon as cladding tube temperatures exceed 1000 °C. The lookup table, however, can only be used to simulate oxidation processes at temperatures greater than 1525 °C (see Chapter 4). Therefore, all simulations must be initialized in such a way that identical conditions for the oxygen uptake prevail when they are started at 1525 °C. Therefore, a pre-oxidation phase is stipulated, which simulates the oxidation under isothermal conditions at 1525 °C until the oxide layer thickness equals the solution of the base case at the exact moment that the temperature condition of 1525 °C is reached.

A direct reproduction of the heat transfer model from ATHLET-CD is not possible due to its complexity. Therefore, a simplified heat transfer model was developed, which is coupled to all models in almost identical form and provides them with the environmental parameters of the base case as boundary conditions. This simplified model considers the following heat sinks and sources:

- Radial heat exchange with the coolant flowing in the cooling channels (input: heat transfer coefficients and coolant temperature)
- Radial heat exchange with the directly neighboring node via thermal radiation (input: temperature of the neighboring node)
- Radial heat exchange with the fuel (as the source of decay heat) via heat conduction (input: fuel temperature, decay heat power)
- Axial heat exchange of the cladding tube material with the nodes above and below via heat conduction (input: cladding tube temperatures of the neighboring nodes)
- Axial heat exchange of the fuel with the nodes above and below via heat conduction (input: fuel temperatures of neighboring nodes)

9.2.1. Case 1: Oxidation

As the first model case, the simulation results of a node in the innermost and, thus, the central core channel at the lowest axial position of the active core height are used (radial 1, axial 2). Due to its low position in the reactor pressure vessel, the cladding tube material in this node is covered by water for a long time and only exposed to the steam-containing environment at a relatively late stage of the accident. Hence, its oxidation starts at $157\,min$ and is completed at $170\,min$. During the entire oxidation period, the relative steam availability in this node is 100 %. Therefore, the oxidation process in this node represents the core application of oxidation models based on parabolic rate approaches.

Fig. 9.8 shows the cladding tube temperature (dashed red line), as calculated by Trometer [55] with ATHLET-CD from the point in time when it first exceeds 1525 °C ($9723\,s$) until it falls to temperatures less than 1525 °C again ($10544\,s$).

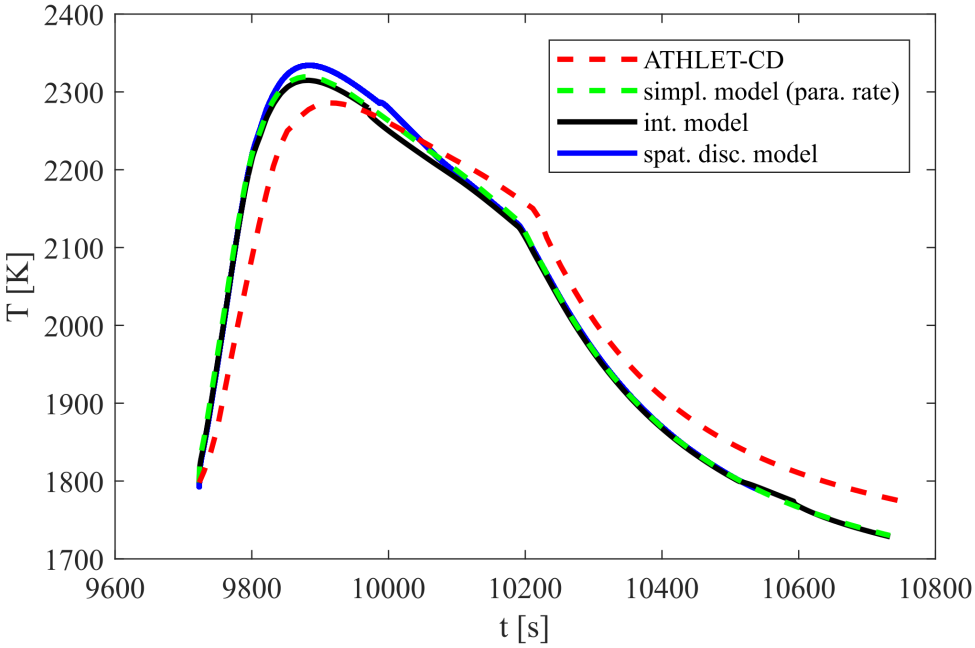

Figure 9.8.: Comparison of cladding temperatures, as calculated by means of different models (case 1).

Fig. 9.9 depicts the corresponding temporal development of the oxide scale of the fuel rod cladding tube in this node (dashed red line). At $9723\,s$, when the temperature first reaches 1525 °C, the outer $0.0754\,mm$ of the initially $0.63\,mm$ thick cladding tube has already been consumed by the oxidation reaction. A depiction of the inner oxide scale is omitted because its thickness remains constant at less than $0.008\,mm$. Therefore, a permanent leakage of steam into the cladding tube, which is facilitated by mechanical damage, can be excluded. Consequently, the internal cladding oxidation is neglected in the following considerations.

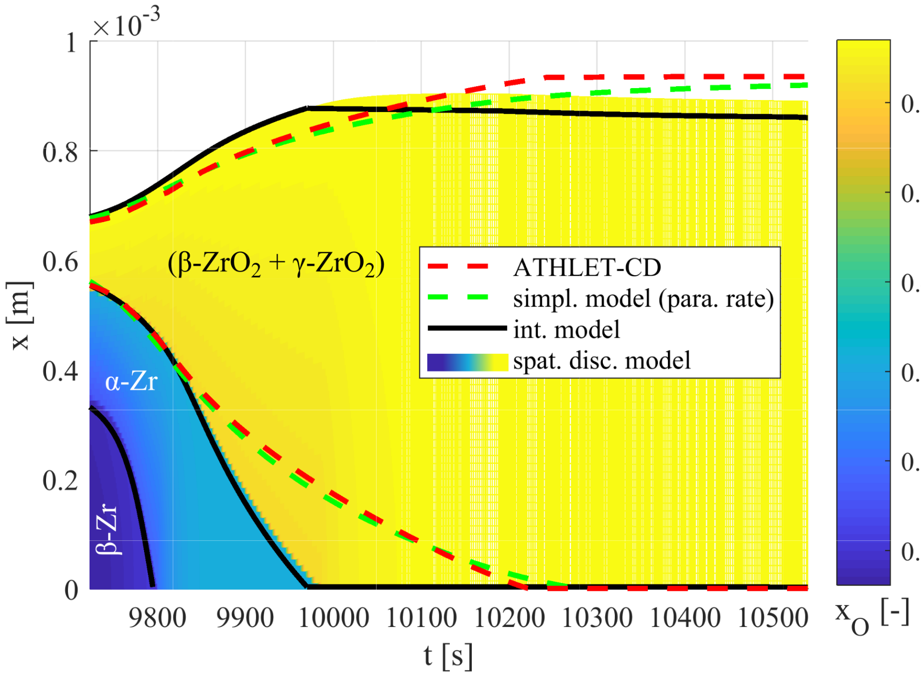

Figure 9.9.: Comparison of the progression of phase interfaces, as calculated by means of different models (case 1).

In the first step of the model comparison, the solution obtained with ATHLET-CD is compared to the simplified model described in Appendix A, which is also based on a parabolic rate approach. Fig. 9.8 shows that the temperature curve of the simplified solution (solid black line) follows the solution of the base case (dashed red line) qualitatively. However, the simplified model predicts a more rapid heating of the cladding tube that culminates in a cladding tube temperature of 2324 K already at 9880 s (compared to 2286 K at 9910 s). Despite the differences in the temperatures in the early phase of the simulation, the solutions initially agree well in terms of oxide layer thickness. From approximately 9900 s onward, an acceleration of the growth of the layer thickness in the solution of ATHLET-CD can be observed, which is not reproduced in the simplified model. Resultantly, the original solution leads to the complete consumption of the metal after 10240 s, which is around 300 s faster than in the simplified model given in Appendix A.

In the second step of the model comparison, the solution of the simplified model is compared to the solutions of the spatially discretized model (100 cells) and the advanced integral model. To emulate an identical progress of the oxidation at the start of the simulations at 1525 °C, both models start with a phase of pre-oxidation under isothermal conditions until 0.0754 mm of the base material is consumed by the chemical reaction. Following this, the models are restarted with the complex boundary conditions specified by the base case.

Fig. 9.8 shows that the solutions of both models deliver quantitatively similar results with respect to the temporal development of the cladding tube temperatures. Only the peak temperatures differ slightly. Larger differences between the modeling approaches can be observed with regard to the spatial expansion of the oxide layer, as shown in Fig. 9.9. Both the spatially discretized model and the integral model calculate a conclusion of the oxidation reaction already after approximately 9980 s, which is around twice as fast as the simplified model and the model in ATHLET-CD. Since the temperatures are reproduced well, this mismatch can be attributed to the difference in the kinetic parameters, the parabolic rate constants, and the diffusion coefficients. A parameter tuning for the unification of both solutions has been dispensed with at this point because the result of the comparison remains unaffected in its core statement. This statement is that the models developed in the course of this work can simulate the oxidation reaction even under the influence of complex boundary conditions supplied by other models (e.g., thermo-hydraulic models) of severe accident analysis codes.

9.2.2. Case 2: Steam starvation

The second test case builds on the sequence of events that can be observed in a node in the central core channel on an axial position that is close to core center (radial 1, axial 9). Due to its simulated, elevated position in the reactor pressure vessel, the coolant level in this node drops significantly earlier than in the previous case. As a result, cladding tube temperatures already exceed 1525 °C after approximately 121 min.

Fig. 9.10 depicts the cladding tube temperature as calculated using ATHLET-CD (dashed red line) from 7261 s until the partially oxidized cladding material starts to melt at 7483 s.

Fig. 9.11 presents the corresponding temporal development of the oxide layer thickness. At 7261 s, the outer 0.0342 mm of the initially 0.63 mm thick cladding tube is oxidized. As in the previous case, an oxidation of the inner cladding tube does not occur. Furthermore, the node's cladding tube material is oxidized in two temporally intermittent phases from 7261 s to 7293 s and from 7432 s to 7483 s. In these phases, steam availability is permanently above 10 %, which means that the threshold for steam depletion of ATHLET-CD does not fall short. Between these phases, the node is completely closed off from further steam supply (7432 s to 7483 s), which has severe effects on both cooling and oxidation. Thus, this node presents an example for ambient conditions in which integral models offer significant advantages over models based on parabolic rate approaches (see Section 9.1).

Again, in the first step of the model comparison, the original solution obtained with ATHLET-CD is compared with the solution of the simplified model, which is similarly

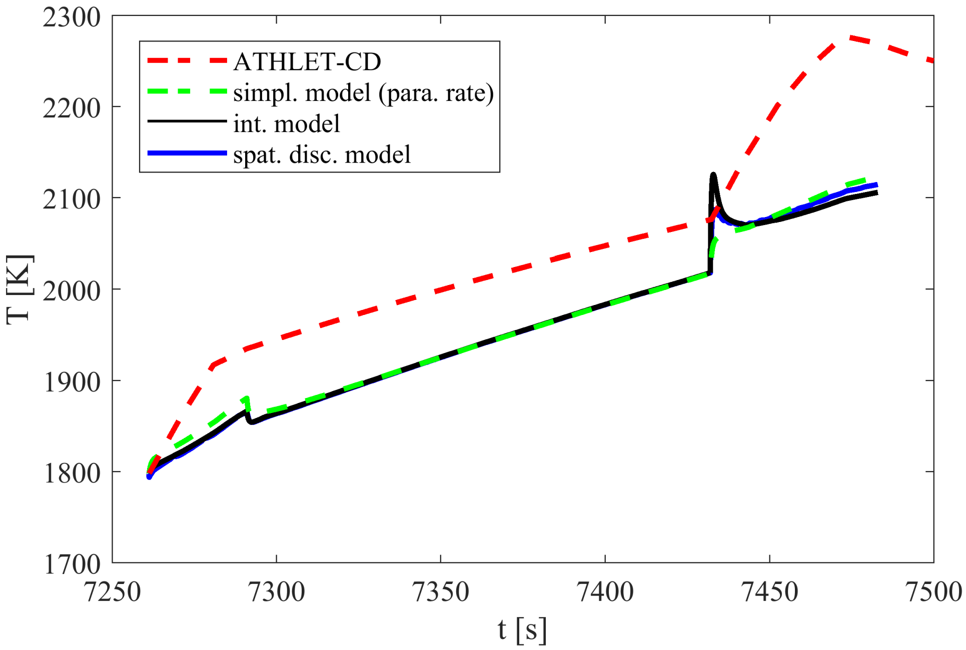

Figure 9.10.: Comparison of cladding temperatures, as calculated by means of different models (case 2).

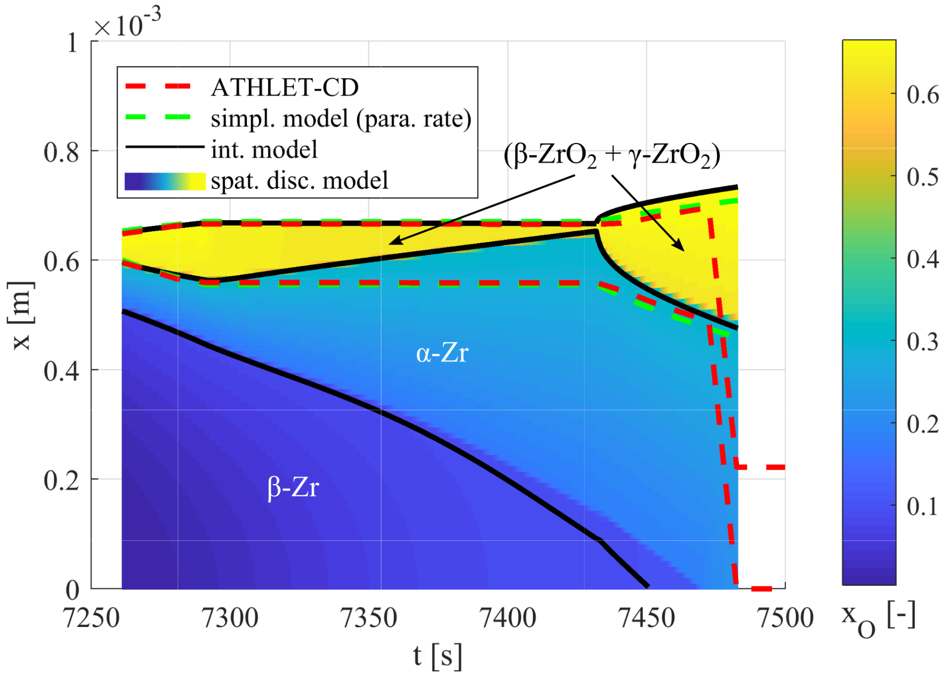

Figure 9.11.: Comparison of the progression of phase interfaces, as calculated by means of different models (case 2).

based on parabolic rate approaches. Fig. 9.10 shows that simplified model predicts a significantly lower heating of the cladding tube than the original solution of the base case. Moreover, the simulation with the simplified model indicates a temperature reduction in connection with the steam-starved conditions between $7432\,s$ and $7483\,s$, which the original solution does not show. Thus, in this test case, the simplified model can reproduce the temporal development of the cladding tube temperatures of the solution from ATHLET-CD only to a limited extent. Nonetheless, the growth in oxide layer thickness is reproduced in qualitative agreement (see Fig. 9.11; error $< 12.8\,\%$). Since the oxidation reaction is well predicted, it is possible to conclude that temperature differences are solely caused by the simplified heat transfer model, which uses a reduced set of input parameters. Therefore, comparability of the solution of the simplified model (reference solution) to the solutions of the advanced integral model and spatially discretized models is still given.

The second step of the model comparison demonstrates that the simplified model predicts a slightly elevated and faster heating of the cladding tube in the first oxidizing phase compared to the spatially discretized model and the advanced integral model, the solutions for which almost match (see Fig. 9.10). Their solutions also imply significantly lower local temperature maxima of $1881\,K$ at $7291\,s$ (instead of $1935\,K$ at $7291\,s$). With the change in steam-starved conditions, the temperature first drops slightly in all models, but then increases again, supported only by the heat provided through the boundary conditions. Significant differences between the three models can be observed following the resumption of oxidizing conditions ($7432\,s$). At this point, the solution, which is based on parabolic rate approaches, shows no local temperature peak, whereas the solution of integral model ($2126\,K$), as well as the solution of the spatially discretized model, exhibit this phenomenon ($2087\,K$).

In Fig. 9.11, the solutions of all models agree qualitatively on the progress of the oxidation front in the first oxidizing phase from $7261\,s$ to $7293\,s$. With the change to steam-starved conditions, only the advanced integral model follows the solution of the spatially discretized model and predicts a retreat of the oxide scale. In contrast, both the original solution and the simplified oxidation model fail to account for that effect. Likewise, only the integral model is capable of reproducing the reinforced growth rate of the oxide layer as soon as the oxidizing conditions are reestablished (at $7432\,s$), which the solution of the spatially discretized model shows.

By chance, the final thickness of the oxide layer (at $7483\,s$), as calculated using the models based on parabolic rate equations, is identical to the solution of the advanced integral model and the spatially discretized model. Hence, it is necessary to analyze differences in the total extent of the oxygen uptake in greater depth because they result from the use of different oxidation models. In analogy to Section 9.1, this is achieved via the comparison of hydrogen generation, as shown in Fig. 9.12. Both the spatially discretized model (blue line) and the integral model (black line) show that the resumption of oxidation leads to a sudden increase in the hydrogen generation, which doubles the hydrogen mass produced so far within $5\,s$. This doubling is not reproduced by the simplified model (dashed green line), which is based on a parabolic rate approach, and so this mass consistently misses in the further progress of the simulation.

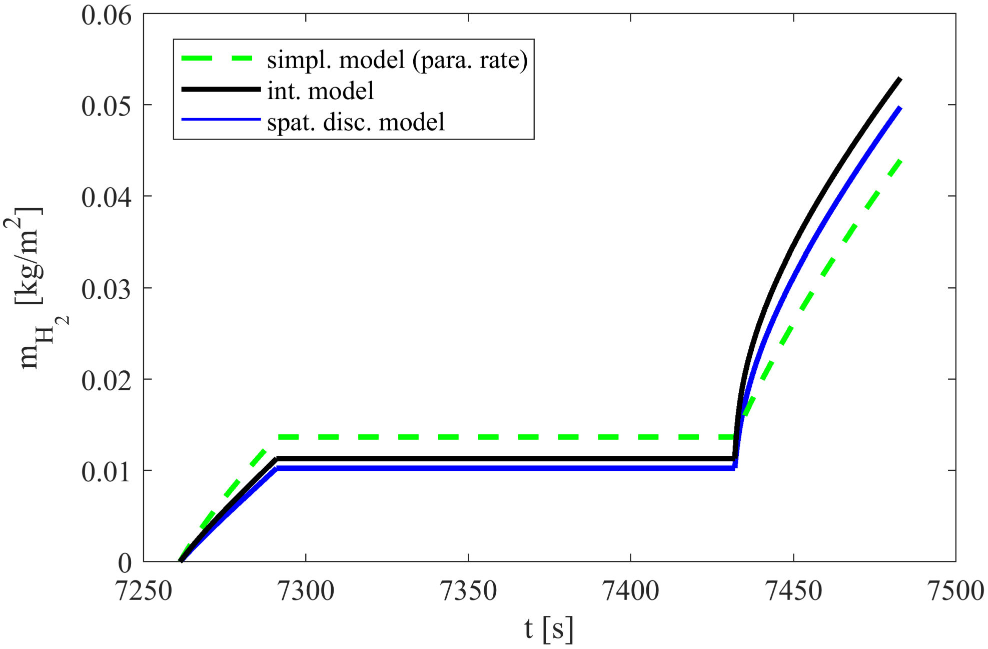

Figure 9.12.: Comparison of the simulation results regarding the total oxygen uptake expressed via the generated hydrogen mass.

In conclusion, the advanced integral model developed in the course of this work can follow the oxidation reaction even under the influence of complex boundary conditions coming from other physical models of severe accident analysis codes. In this context, the advanced integral model further shows the ability to reproduce peaks of heat and hydrogen generation after temporary phases of steam starvation in good agreement with the spatially discretized model. This characteristic is the crucial difference to the models based on parabolic rate approaches, which are commonly used in today's severe accident analysis codes.

10. Model tests including thermally-induced phase changes

In the previous chapter, the integral model was compared to existing oxidation models from the literature, as well as those that reflect the state of the art in severe accident analysis codes. In this context, the integral model's ability to model chemically-induced phase changes under variable and, to some extent, complex material and thermal boundary conditions was investigated. However, this tests assumed the absence of thermally-induced phase changes.

In this chapter, the advanced integral model's ability to describe those thermally-induced phase changes is tested. This task lies beyond the scope of applying the existing oxidation models and, therefore, is an expression of the advances made. In this context, it is to be determined whether the assumptions of the advanced integral model affect the simulation results (see Section 6.3). This concerns the following:

- Neglection of two-phase transition zones between adjacent single-phase zones
- Consequential modeling of mass transport with virtual, sharp phase boundaries
- Estimation of phase equilibrium concentrations based on bulk temperatures
- Modeling of heat transport with simple heat balances
- Modeling of thermally-induced phase changes by adjusting phase fractions within zones

Due to the lack of experimental data, as well as the absence of comparable models in the literature, simulations with the advanced integral model are again compared to simulations of the spatially discretized model, which is not subject to those assumptions.

Method of investigation

Methodologically, it is expedient to investigate the reproduction of phase changes that are imposed on a model system by external thermal constraints. In preparation for these investigations, the results of Trometer's simulation with ATHLET-CD [55], which were used in Section 9.2, were analyzed with regard to the magnitude and frequency of the occurrence of temporal temperature changes in the cladding tube material. Hence, for all 132 nodes of the core region, time steps were identified in which the calculated cladding tube temperatures exceed 1000 °C and, therefore, favor the high-temperature oxidation of zirconium in steam-containing environments. Using this information, temporal temperature changes from one time step of the output to another were calculated ($\Delta t = 10\,s$, thus averaged). The obtained data were divided into classes and plotted as a histogram, as shown in Fig. 10.1.

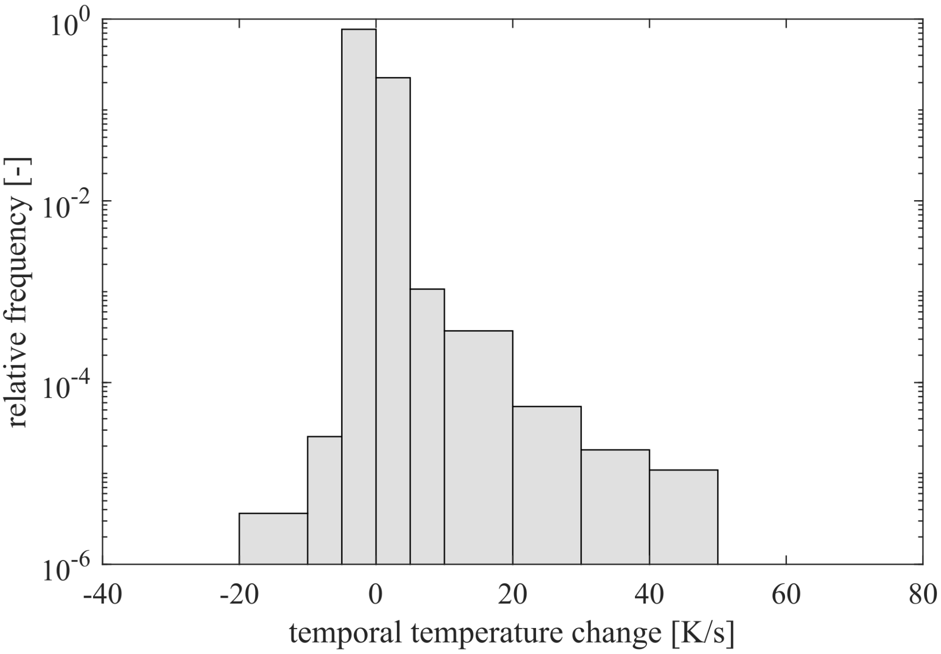

Figure 10.1.: Histogram of temporal temperature changes in the cladding tube material in the base case.

Fig. 10.1 shows that 77.2 % of the temporal temperature changes are in the class from $0\,K/s$ to $-5\,K/s$ and another 22.6 % in the class from $0\,K/s$ to $+5\,K/s$. In 99.95 % of the cases, the temperature changes are between $-10\,K/s$ and $+10\,K/s$. A minimum value of $-11.9\,K/s$ and a maximum value of $+46.9\,K/s$ were determined as the strongest heating and cooling rates. For the sake of completeness, it should be mentioned that the highest cladding tube temperature in the output is 2402.8 °C, which exceeds the melting point of α-Zr yet is still less than the melting temperature γ-ZrO_2 (i.e., 2710 °C).

The data from Trometer's base case [55] provide an approximate indication of the temperature changes that oxidation models in severe accident analysis codes must resolve. In the following, this information is used as a guideline to construct model cases that, in turn, are applied to investigate the advanced integral model's behavior in terms of resolving thermally-induced phase transitions compared to the solution of the spatially discretized model.

Model case

As an example, a $1\,mm$ thick slab consisting of pure zirconium is considered, which is close to the geometry of cladding tubes. It is assumed that this slab is surrounded by an environment in which the steam content is sufficiently high to cause the permanent formation of stoichiometric zirconium dioxide on the slab's surface. After an initial isothermal pre-oxidation phase, oxidation occurs under the influence of various temperature transients. These transients are caused by continuously changing the ambient temperatures imprinted on the material system by a radiation term. In addition, the heat from the oxidation reaction and the energy required for the dissociation of the water vapor at the surface of the slab (into hydrogen and oxygen) are considered. The side of the slab that is averted from the steam-containing environment is simulated by reflecting boundary conditions.

Consistent with the analysis of the temperature changes in the base case, seven model cases are examined in which the ambient temperature is subject to positive transients ($+5\,K/s$, $+10\,K/s$, $+30\,K/s$, and $+60\,K/s$) and negative transients ($-5\,K/s$, $-10\,K/s$, and $-30\,K/s$). The trivial case $0\,K/s$ corresponds to isothermal conditions and, therefore, is not discussed here. Simulations with positive temperature transients are preceded by an isothermal pre-oxidation phase of $100\,s$ at 1525 °C and subsequently continued under transient conditions until the system is completely melted. Negative transients are initialized with an isothermal pre-oxidation phase of $10\,s$ at 2500 °C and followed up until the cladding tube temperature is equal to 1525 °C. In this case, the pre-oxidation time is shorter because the chemical reaction is considerably faster at higher temperatures. The starting temperature of 2500 °C is chosen to avoid temperature escalations that go beyond the melting point of zirconia at the start of the simulations.

The ability of the advanced integral model to reproduce thermally-induced phase changes is assessed on the basis of several parameters. Priority is given to the spatial manifestation of the different phases and, therefore, their emergence and disappearance in accordance with the solution of the spatially discretized model. Additionally, the oxygen uptake is integrated over time and converted into a corresponding hydrogen mass, which is a measure for the absolute extent of the chemical reaction that has occurred up to a certain point in time. Since the temperatures of the simulated slabs follow the external constraints to a high degree, an explicit investigation of this parameter is omitted.

10.1. Positive temporal temperature transients

Transient $+5\,K/s$

The first investigated model case is the high-temperature oxidation of the test system superimposed by a positive temperature transient of $+5\,K/s$. In this context, Fig. 10.2 compares the solution of the spatially discretized model (100 cells) and the solution of the advanced integral model regarding the temporal evolution of the different thermodynamic phases over time. Here, the solution of the spatially discretized model is depicted with a color code, which assigns a color to each cell depending on the phase(s) present (α-Zr: yellow, β-Zr: orange, oxide (β-ZrO_2 and γ-ZrO_2): blue, L: green, two phases: grey). Accordingly, phase interfaces are indicated by locations in which the color of the cells changes from one to another. Fig. 10.2 also presents the positions of the phase interfaces from the simulation with the advanced integral model (solid black lines).

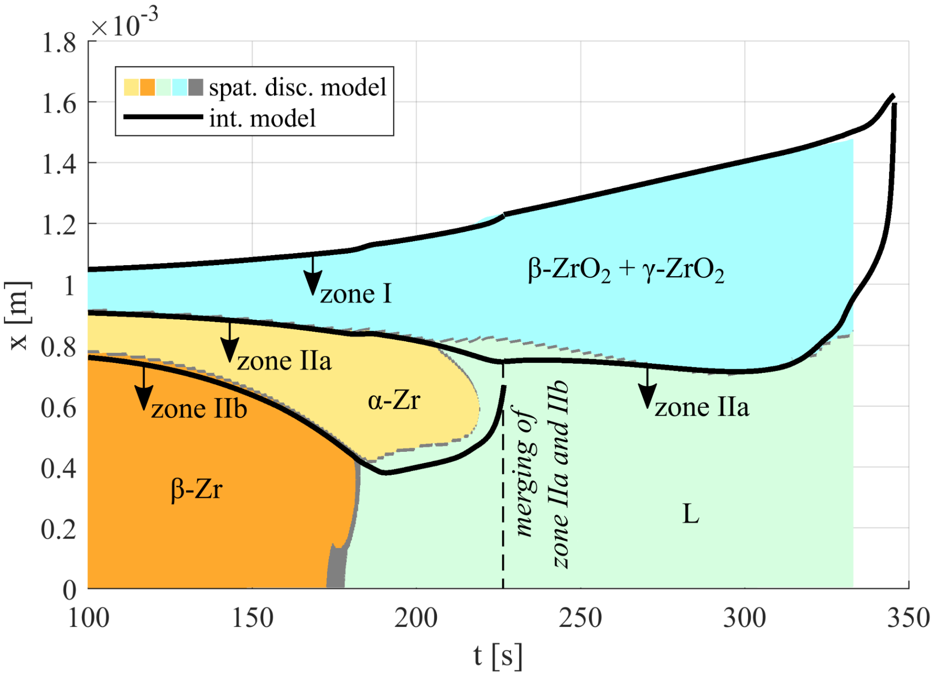

Figure 10.2.: Temporal evolution of the expansion of phases with an imprinted transient of $+5\,K/s$.

In the advanced integral model, thermodynamic distinct phases are summarized into zones separated by virtually sharp phase interfaces (see Chapter 6). Fig. 10.2 shows only the phase interfaces (solid black lines) defining the boundaries of those zones (black arrows). However, it does not indicate the phases that are summarized into a respective zone. Therefore, this information is complemented by Fig. 10.3, which presents the phase fractions of each zone in the advanced integral model over time.

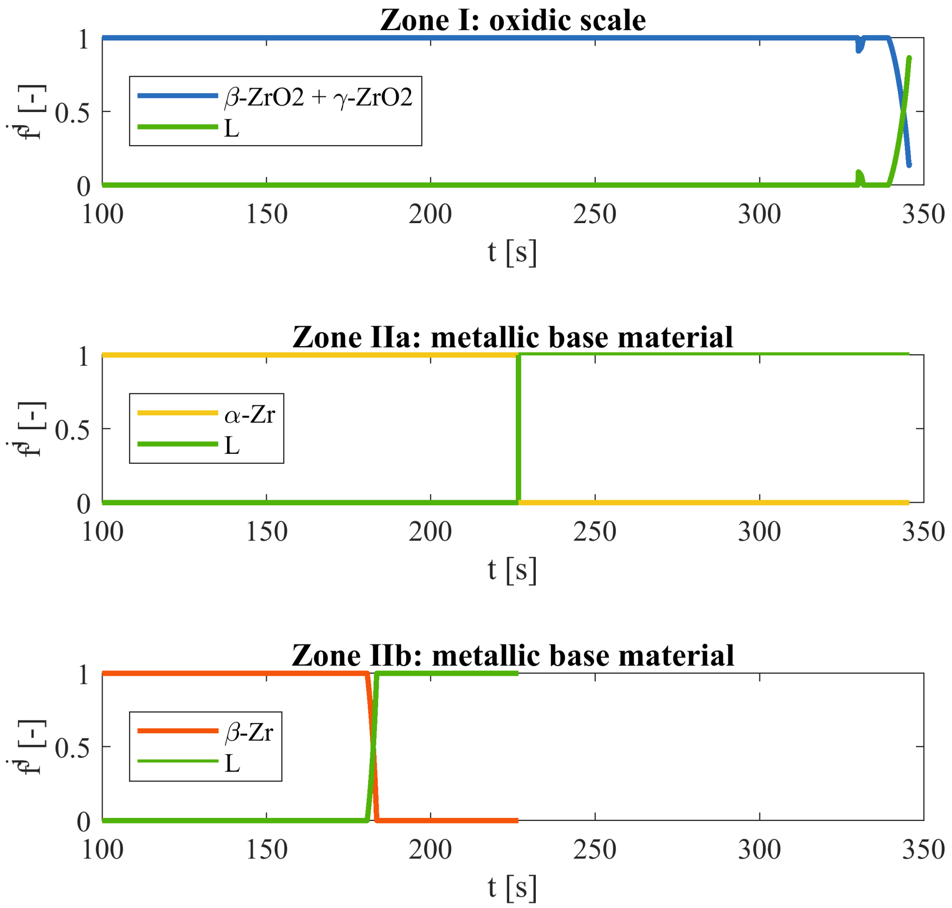
Zone I: oxidic scale

Zone IIa: metallic base material

Zone IIb: metallic base material

Figure 10.3.: Phase fractions of the initially three distinct zones in the integral model. At $220\,s$ zone IIa melts and merges with zone IIb (case: $+5\,K/s$).

After the completion of the isothermal pre-oxidation phase at $100\,s$ (i.e., immediately before the start of the transient), the solution of the spatially discretized model shows three distinct phases: an oxidic scale consisting of β-ZrO$_2$ and γ-ZrO$_2$, a layer of metallic α-Zr, and the metallic base material β-Zr (see Fig. 10.2). The advanced integral model likewise predicts three distinct zones, which match the solution of the spatially discretized model in both the positions of the phase interfaces (Fig. 10.2) and the phases present (Fig. 10.3).

From $100\,s$ to $173\,s$, both models are relatively consistent in terms of the growth of the oxide layer and of the metallic α-Zr phase (see Fig. 10.2). At $173\,s$, the spatially discretized model predicts the onset of the melting of the metallic β-Zr phase, which is completed at $180\,s$ (see Fig. 10.2). The advanced integral model treats thermally-induced phase transitions via changing phase fractions of its zones. Accordingly, Fig. 10.3 (zone IIb) shows that the phase fraction of the β-Zr phase in the advanced integral model starts to decrease from $100\,\%$ at $180\,s$ to $0\,\%$ at $183\,s$. Simultaneously, the phase fraction of the liquid phase (L) increases from $0\,\%$ to $100\,\%$. In both models, after the melting of the β-Zr phase, the movement of the phase interface between α-Zr and L is first slowed down and, in turn, reversed. In the solution of the spatially discretized model, a second liquid phase appears at the phase interface between α-Zr and oxidic ZrO_2 at $200\,s$. In the same model, α-Zr is completely melted after $220\,s$ so that both liquid phases merge. The integral model does not consider this second liquid phase because it would cause two simulation stops within $75\,K$, thus influencing its numerical stability. Consequently, there is a deviation of the solutions at this point with respect to oxide layer thickness. Despite this difference, the solution of the advanced integral model indicates that the melting of the α-Zr phase is completed after $227\,s$ (see Fig. 10.3: zone IIa). Therefore, this is only $7\,s$ later compared to the result in the spatially discretized model. After the completion of the melting of the α-Zr zone, two liquid zones exist in the advanced integral model. Consequently, assuming an ideal and instantaneous mixing process, the integral model merges the two liquid zones that originate from both the molten β-Zr (Fig. 10.3: zone IIb) and the molten α-Zr (Fig. 10.3: zone IIa). After that event, the solutions of the spatially discretized model and the advanced integral model again align. At approximately $320\,s$, the dissolution of the oxide accelerates rapidly in both numerical oxidation models. Due to this acceleration, the solution of the spatially discretized model becomes numerically unstable and stops at $333\,s$. Intensive efforts to stabilize the solution by varying solvers, error tolerances, and spatial grids were unsuccessful. The simulation with the integral model, which is more stable, stops with the completion of the melting of the oxide at $347\,s$.

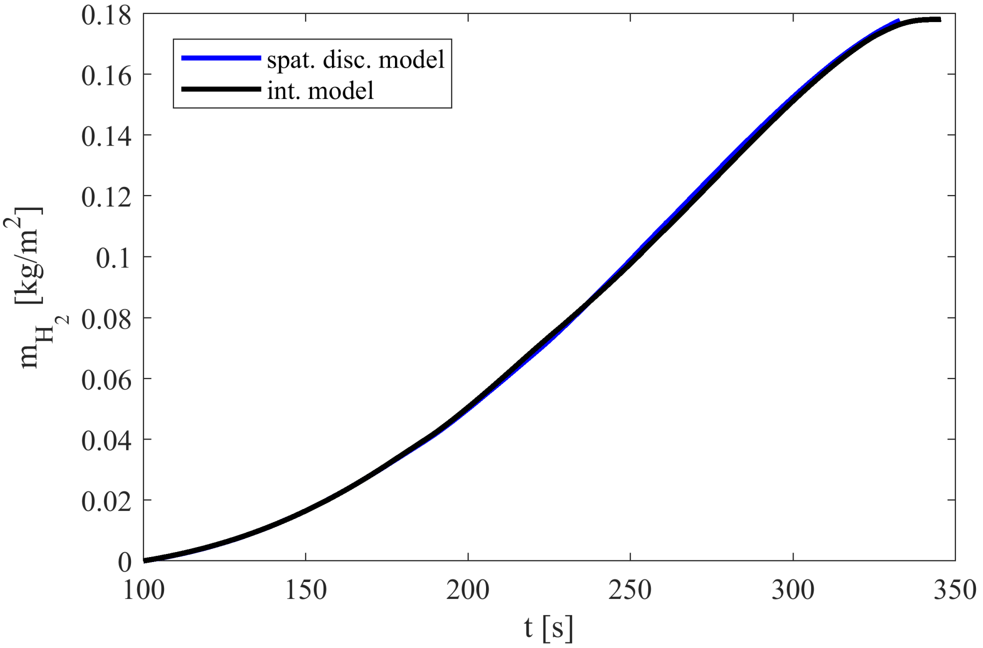

Figure 10.4.: Integral of hydrogen generation for the model case with an imprinted transient of $+5\,K/s$.

Fig. 10.4 shows the temporal development of hydrogen formation. Here, the solutions of the spatially discretized model and the integral model are depicted with a blue line and a black line, respectively. It can be noticed that, despite differences in the positions of the phase interfaces in both solutions, the total extent of the chemical reaction in both simulations matches.

In summary, it can be stated that the advanced integral model's assumption to neglect two-phase zones between adjacent single-phase zones does not have a negative influence in this model test ($+5\,K/s$). During the melting of the β-Zr phase, spatially extended two-phase regions consisting of β-Zr and L are observed temporarily. The advanced integral model's novel method of treating thermally-induced phase changes via the phase fractions on the level of the zones, and without a second moving boundary condition, can simulate this behavior. The simulation with the spatially discretized model does not give an indication of the permanent occurrence of multi-phase zones at the phase interfaces, which move due to mass transfer processes, meaning that these interfaces remain sharp. Neglecting the second liquid phase has only a temporary negative effect on the simulation results. Considering the total duration of the transient of approximately $247\,s$, there is only a small deviation regarding the points in time at which key events relating to thermally-induced phase transitions start or end. Despite minor differences regarding the positions of the phase interfaces, the estimation of hydrogen formation is consistent. In conclusion, the results of the comparison verify the suitability of the advanced integral model's new method to resolve thermally-induced phase changes accompanying the high-temperature steam oxidation of zirconium alloys. In this context, the integral model provides a solution that is in good agreement with the solution of a spatially discretized model, while requiring substantially less computational effort.

Transients $+10\,K/s$, $+30\,K/s$, and $+60\,K/s$

With a relative frequency of only around 0.15 %, changes in the cladding tube temperatures are greater than $+5\,K/s$ in the base case.

The results of the numerical experiment with a transient of $+10\,K/s$ match those of the previous experiment with a transient of $+5\,K/s$. Consequently, this model test is not described in detail. A minor deviation in the simulation with $+10\,K/s$ is the slight overestimation of the hydrogen mass by the integral model of 2.9 % at the end of the simulation. Consequently, all findings regarding the transient of $+5\,K/s$ can be directly transferred to the transient of $+10\,K/s$. Figures of these simulations suitable for the comparison of both modeling approaches can be found in Appendix E.

Fig. 10.5 shows the spatial evolution of the different phases over time for a transient, which is caused by a change in the ambient temperature of $+30\,K/s$. Fig. 10.6 complements information regarding the phases present in the various zones of the advanced integral model.

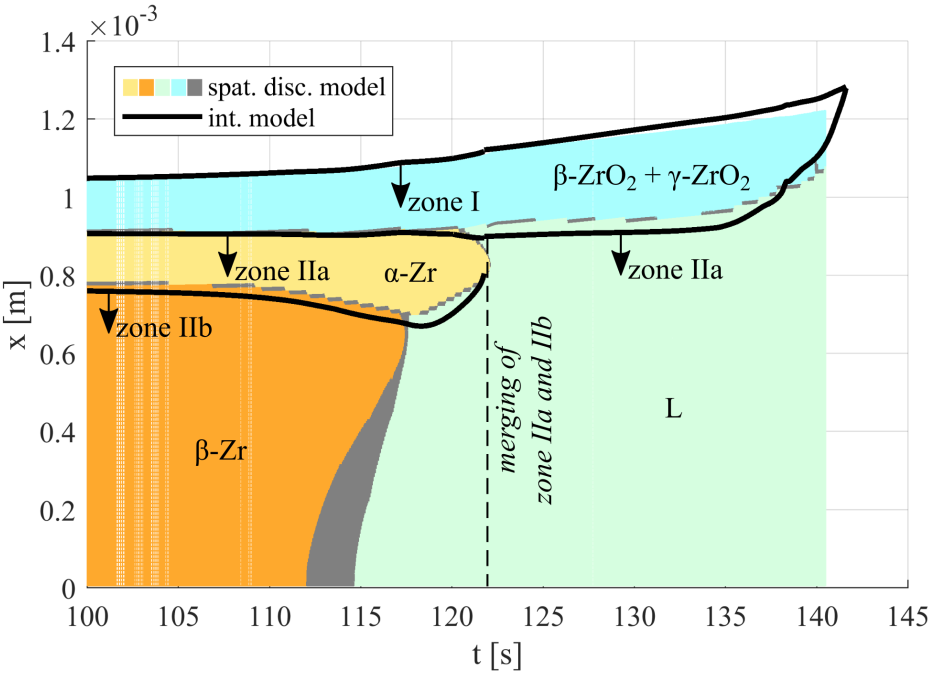

Figure 10.5.: Temporal evolution of the expansion of phases with an imprinted transient of $+30\,K/s$.

The oxidation reaction that is subject to a transient of $+30\,K/s$ follows the same scheme as for the transient of $+5\,K/s$ (compare Fig. 10.2 and Fig. 10.5). From the start of the simulation ($+30\,K/s$), the solution of the integral model matches the solution of the spatially discretized model. However, the thickness of the α-Zr layer is slightly overestimated after the pre-oxidation phase. In the spatially discretized model, melting of the β-Zr phase sets in at $112\,s$ and is completed at $117\,s$ (see Fig. 10.5). In the advanced integral model, this event occurs from $113\,s$ to $117\,s$ (see Fig. 10.6: zone IIb). In the spatially discretized model, and as in the previous case, a second liquid phase occurs at the interface between the oxide scale and the α-Zr layer at $120\,s$, which is not resolved by the advanced integral model. In the simulation with the spatially discretized model, as well as in the simulation with the integral model, the dissolution of the metallic α-Zr phase is completed after $122\,s$. After the melting of the metallic phases, the thickness of the oxide layer is slightly larger in the simulation with the integral model than in the simulation with the spatially discretized model. At $140.5\,s$, the simulation with the spatially discretized model stops due to the substantial acceleration of the oxide layer's dissolution. This acceleration does not affect the solution with the integral model, which calculates the completion of the melting process for a time of $141.6\,s$.

Fig. 10.7 presents the integral of hydrogen generation for the model case with an imprinted transient of $+30\,K/s$. In the solutions of the advanced integral model and the spatially

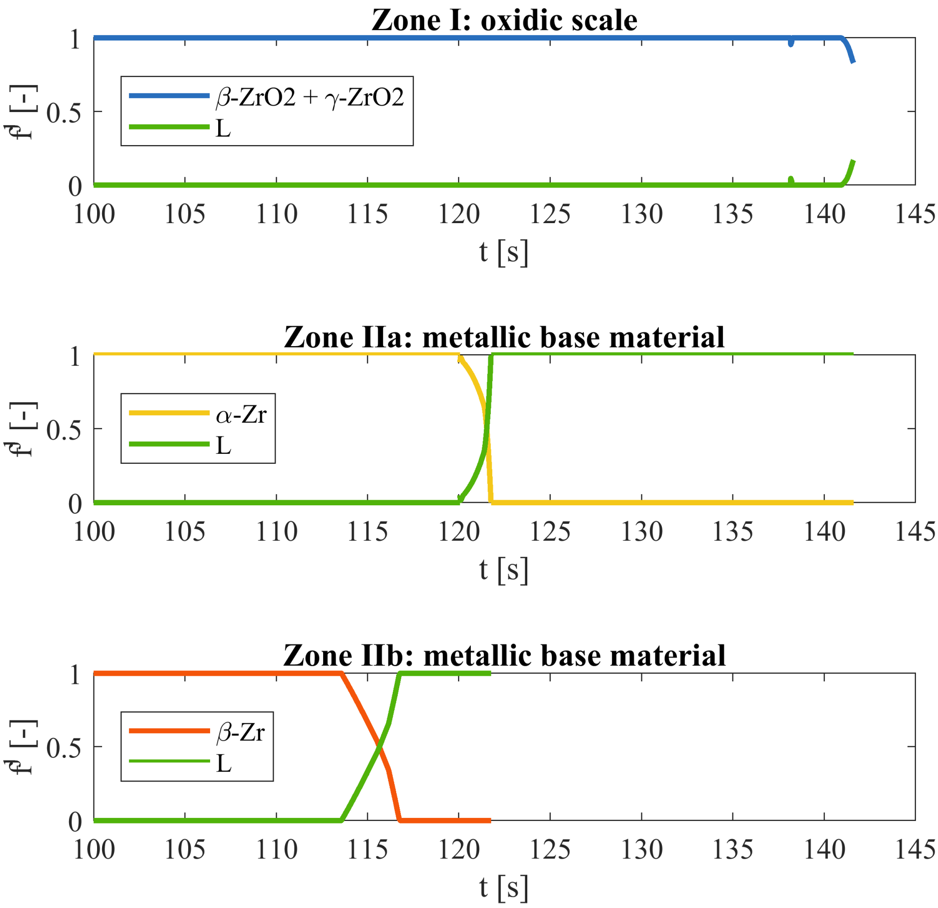

Figure 10.6.: Phase fractions of the initially three distinct zones in the integral model. At $122\,s$, zone IIa melts and merges with zone IIb (case: $+30\,K/s$).

discretized model, the hydrogen masses differ by 14.7 % at the end of the simulation (see Fig. 10.7).

In this test case, the advanced integral model's assumption to neglect two-phase transition zones between single-phase zones again has no negative influence. By contrast, the comparison of both models supports the suitability of the advanced integral model's new approach to assume virtually sharp phase interfaces and to resolve thermally-induced phase changes on the level of the zones (phase fractions). The differences in both solutions, which result from neglecting the emergence of a second liquid phase in the advanced integral model, are further reduced in the case of this transient ($+30\,K/s$). Considering the short duration of the transient in this model case (i.e., $42\,s$), the deviation of the points in time at which key phenomena set in or end almost vanishes. Although that the simulation with the spatially discretized model stops before the system is completely melted, there is a reasonable assurance that differences in the point in time between both models will show an error of less than $5\,s$. Since severe accident analysis codes are usually applied to simulate accident progression on much larger time scales, it is reasonable to assume that

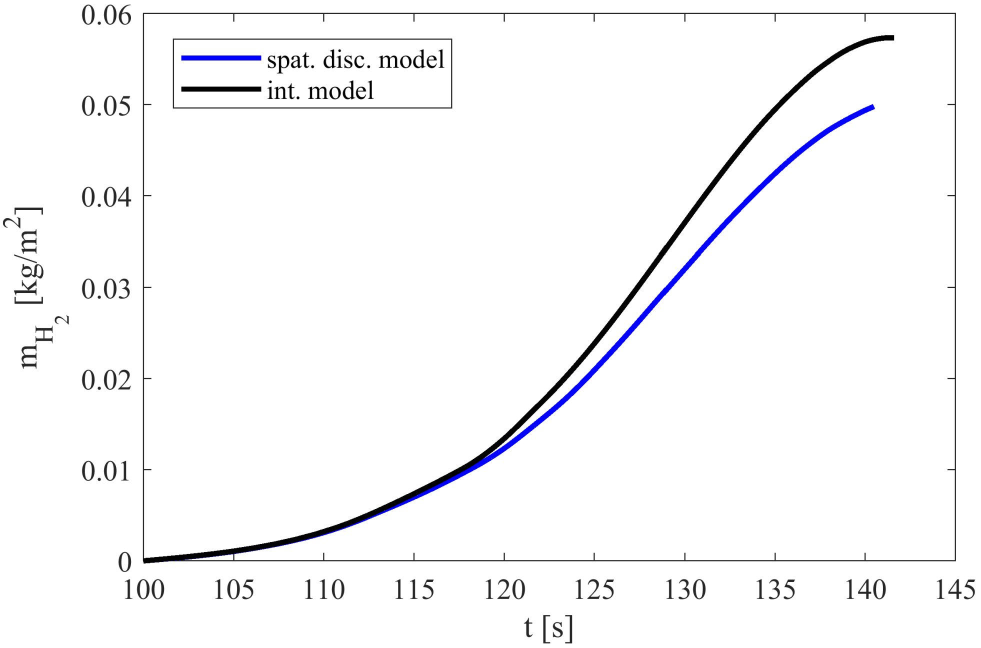

Figure 10.7.: Integral of hydrogen generation for the model case with an imprinted transient of $+30\,K/s$.

those differences have little influence on their solutions. Therefore, it is clear that the advanced integral model can reproduce the results of the spatially discretized model even for such a fast, positive temperature transient.

The solutions of the spatially discretized model and the integral model for a transient of $+60\,K/s$ show strong similarities to the case of a transient of $+30\,K/s$. Due to this strong resemblance, a detailed description of this case is again omitted. It is only noted that hydrogen generation in the integral model is overestimated by 21.7 % at the end of the simulation. The figures for the simulation results of the $+60\,K/s$ transient are given in Appendix E.

10.2. Negative temporal temperature transients

Transient $-5\,K/s$

The next test case assumes a decrease in the ambient temperature by $-5\,K/s$. Fig. 10.8 shows the temporally changing spatial extensions of the different phases as they have been calculated using both the spatially discretized model and the advanced integral model.

Fig. 10.9 supplements information about the phases present in the various zones of the advanced integral model.

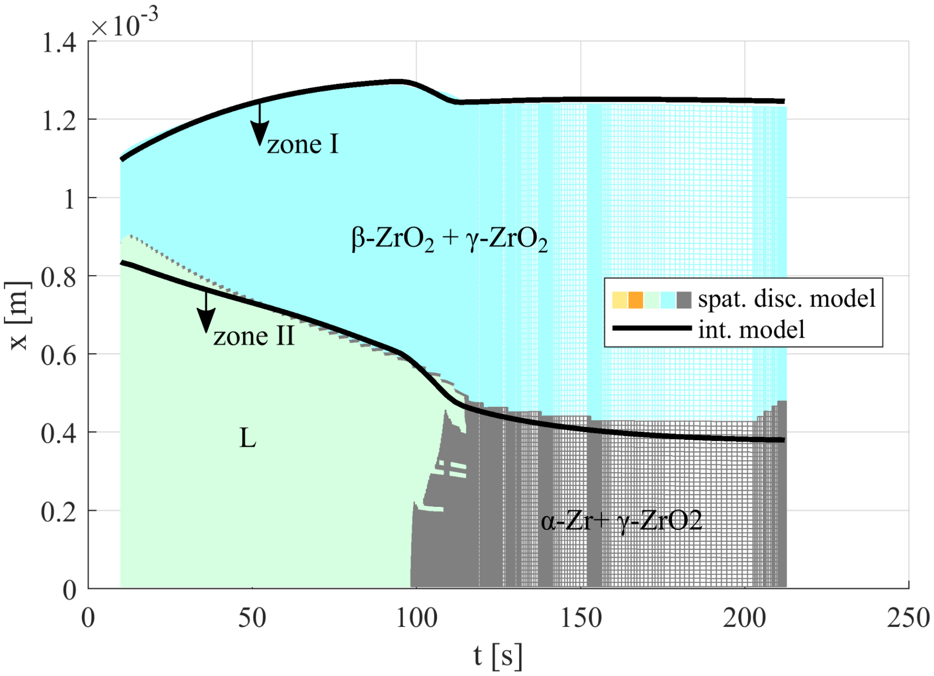

Figure 10.8.: Temporal evolution of the expansion of phases with an imprinted transient of $-5\,K/s$.

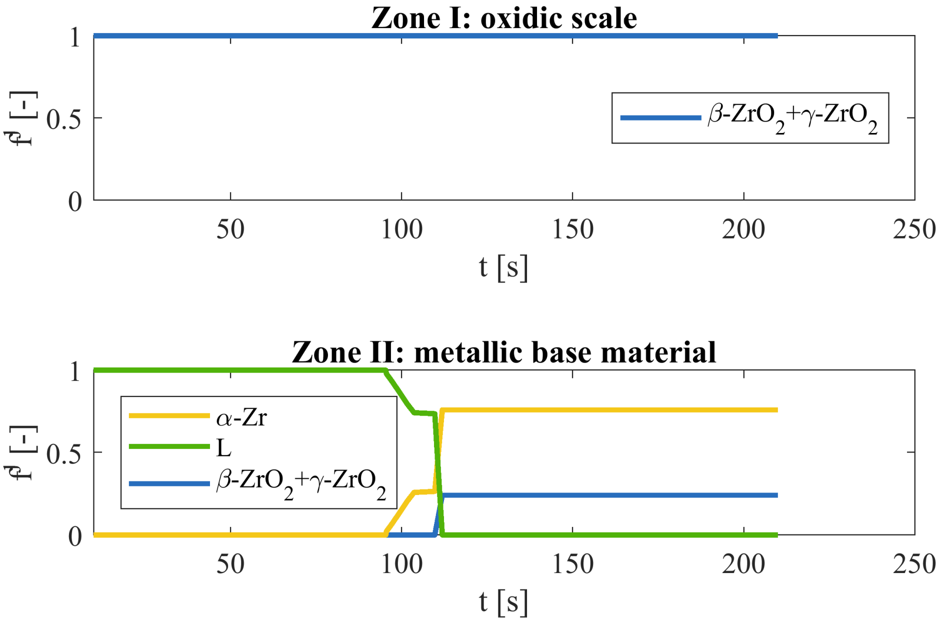

Figure 10.9.: Phase fractions of the two distinct zones in the integral model (case: $-5\,K/s$).

After the completion of the isothermal pre-oxidation phase of $10\,s$ at 2500 °C, two distinct phases are formed in the simulation with the spatially discretized model: first, a solid oxidic phase consisting of γ-ZrO$_2$; and second, a liquid phase (L). The integral model likewise predicts two zones consisting of these phases (see Fig. 10.9). However, based on the comparison of the positions of the phase interfaces between oxide and liquid, it is clear that both solutions already differ at the end of the pre-oxidation phase. Thus, from the start of the transient, the extension of the oxide layer in the solution of the spatially discretized model and in the solution of the integral model differ by 24.4 %.

Fig. 10.8 shows that in both models, the oxide layer continues to grow with a sharp phase interface right from the start of the simulation and, thus, with the change from isothermal conditions to a negative temperature transient. Moreover, both solutions converge within the first 43 s of the transient. In the spatially discretized model, the solidification of the liquid phase begins after 98 s and is completed at 115 s. The solid that is formed in this process is a mixture of α-Zr and γ-ZrO_2. The solidification manifests by a reduction of the outer dimension, which is attributable to the increase in density.[1] The integral model calculates the onset of the solidification for a time of 96 s and, thus, only 2 s earlier than the spatially discretized model. In the integral model, this solidified phase is also a mixture of α-Zr and γ-ZrO_2. Both the continuously decreasing temperature and the increasing thickness of the oxide increasingly inhibit the chemical reactions in both models, thereby significantly reducing the growth rate of the oxide. Both simulations stop after 212 s upon reaching a cladding tube temperature of 1525 °C. At the end of the simulations, the thickness of the oxide layer in the solution of the integral model is only 5.0 % larger than in the solution of the spatially discretized model.

Fig. 10.10 illustrates the calculations of the formation of hydrogen gas as functions of simulation time. As can be seen, solutions of the integral model and the reference solution differ by 9.4 % at 212 s.

Regarding the aim of the investigation, it can be stated that the advanced integral model's neglect of two-phase transition zones between adjacent single-phase regions again has no negative influence on the simulations with a cooling rate of $-5\,K/s$. The same applies to the difference regarding the thickness of the oxide layer after the pre-oxidation phase. The solidification time in both models almost matches, the phases formed during the solidification process are identical, and the difference in the hydrogen generation masses can be regarded as minor. Therefore, in this test case ($-5\,K/s$), the integral model can be regarded as having a good ability to simulate the phase transitions.

---

[1] Mechanical tensions and resulting macroscopic defects of the scale (cracks) are neglected.

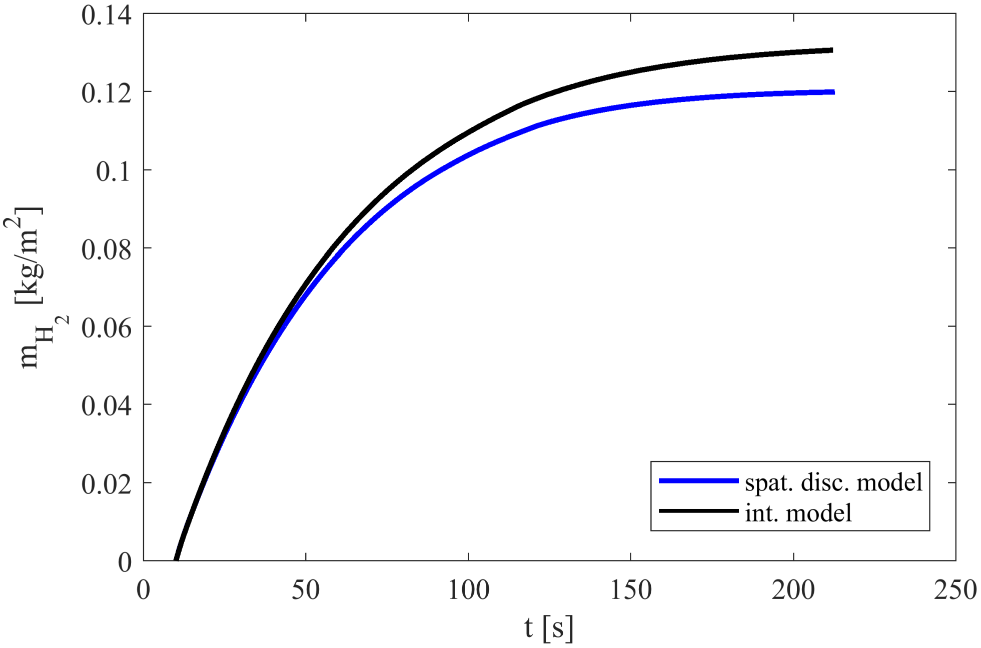

Figure 10.10.: Integral of hydrogen generation for the model case with an imprinted transient of $-5\,K/s$.

Transients $-10\,K/s$ and $-30\,K/s$

The results of the simulation with a cooling rate of $-10\,K/s$ follow the descriptions given for the $-5\,K/s$ case. Therefore, a detailed analysis of this model case is omitted. However, it is to be stated that in this test case ($-10\,K/s$), the difference regarding the thickness of the oxide layer after the pre-oxidation phase disappears after the completion of solidification, and that, consequently, the solutions of the spatially discretized model and the integral model coincide regarding the position of the phase interface between oxide and metal. The overestimation of hydrogen formation is also reduced to 9.1 %. The figures describing this simulation are given in Appendix E.

The tendency towards a better agreement of the simulation results of both models continues when the ambient temperature is decreased by $-30\,K/s$. In this context, Fig. 10.11 depicts the spatial extensions of the different phases in the simulations with the spatially discretized model and the advanced integral model. In addition, Fig. 10.12 presents the phase fractions of the zones in the advanced integral model.

Fig. 10.11 shows that the solution of the integral model again approaches the solution of the spatially discretized model once the transient is started. Consequently, the positions of the solid-liquid interface in both solutions are in agreement after approximately $25\,s$. A difference between the two solutions is the composition of the solidified phase. According

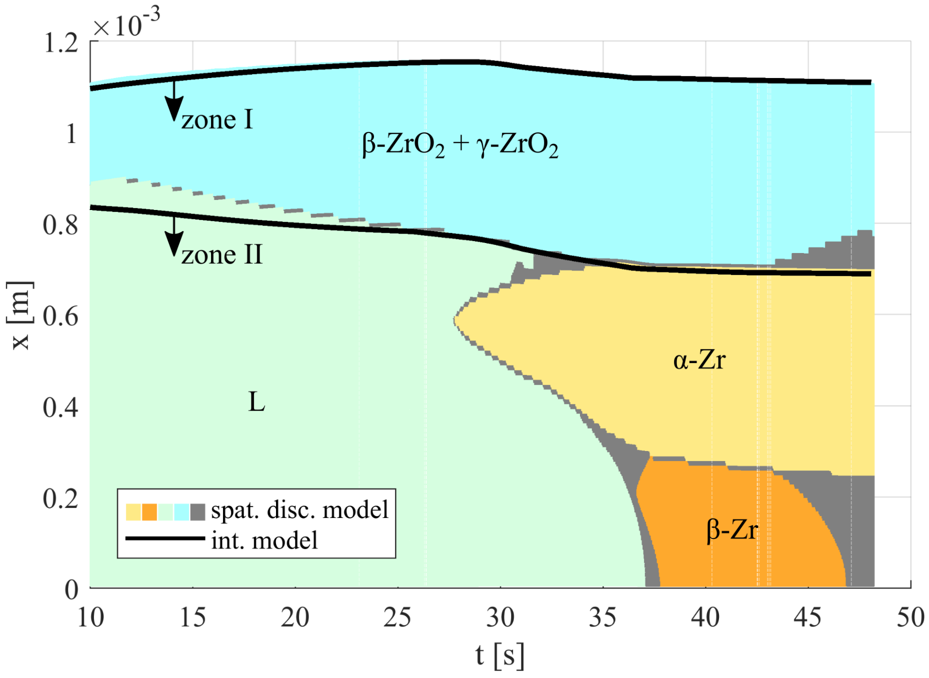

Figure 10.11.: Temporal evolution of the expansion of phases with an imprinted transient of $-30\,K/s$.

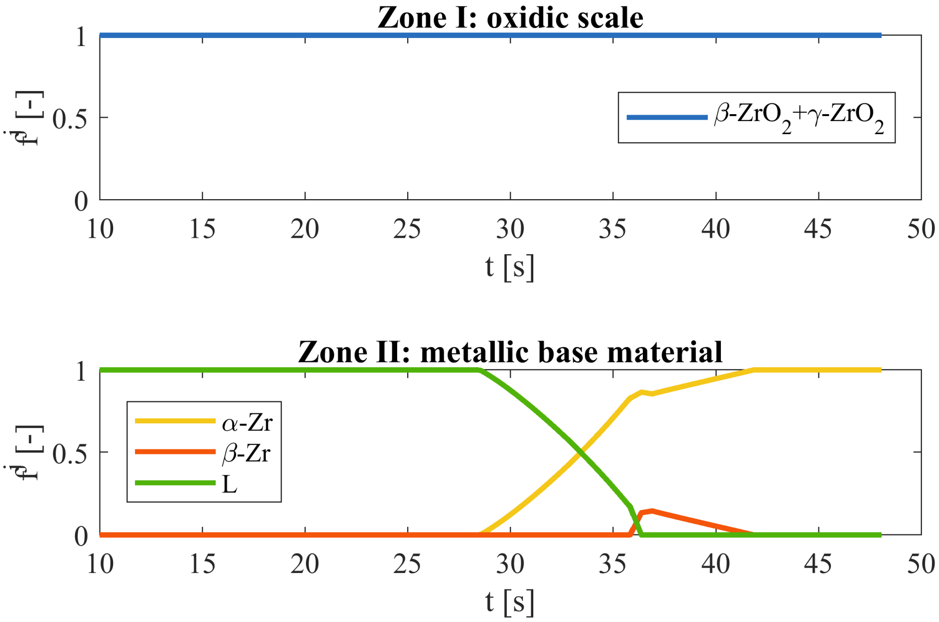

Figure 10.12.: Phase fractions of the two distinct zones in the integral model (case: $-30\,K/s$).

to the spatially discretized model, the first liquid solidifies as α-Zr after $28\,s$. Furthermore, a second spatially separated metallic phase, β-Zr, is formed after $37\,s$. In turn, this β-Zr turns into a mixture of α- and β-Zr after a further transition between $44\,s$ and $47\,s$. In the advanced integral model, this phase change is simulated differently. Here, the solidification turns the liquid zone into a mixture of α- and β-Zr, which later transforms into α-Zr (see Fig. 10.12). In Fig. 10.13, this transformation process is plotted on the binary Zr-O phase diagram, which accounts for this different result. As can be seen, the average oxygen concentration of the solidifying liquid phase in the advanced integral model is above the stability limit of β-Zr, so that the model does not stop to introduce an additional zone containing pure β-Zr.

The temporal development of the hydrogen mass formed in the course of the chemical reaction is plotted in Fig. 10.14. Here, the hydrogen mass calculated using the integral model is 6.5 % higher than in the solution of the spatially discretized model.

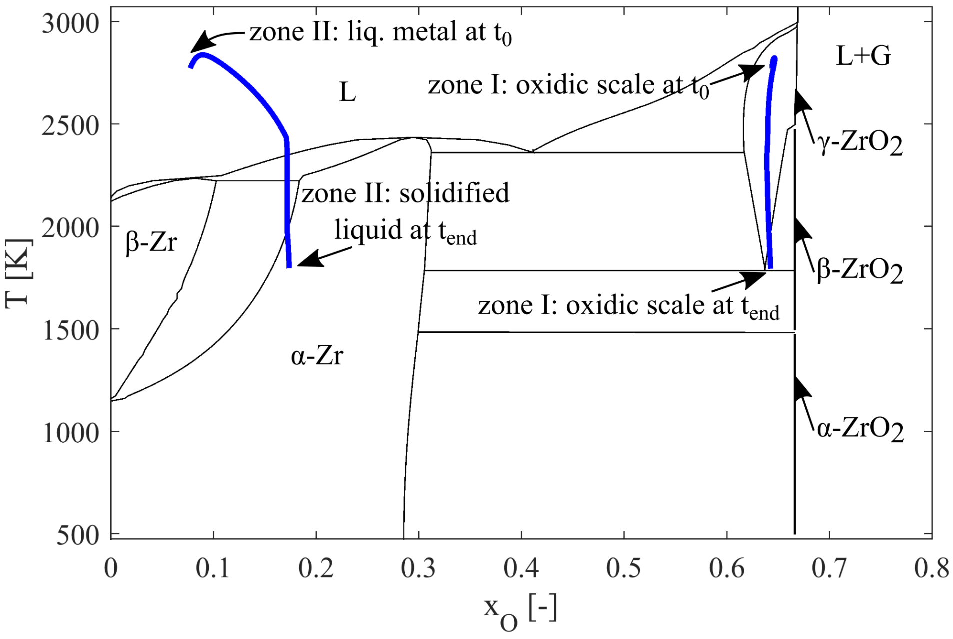

Figure 10.13.: Path of the phase change processes, as calculated using the advanced integral model illustrated in the Zr-O phase diagram.

The simulations with a temporal change in ambient temperature at a rate of $-30\,K/s$ allow the following conclusions to be drawn regarding the integrated model's ability to reproduce thermally-induced phase changes that are consistent with the spatially discretized model. The different spatial extension of the oxide layer after the pre-oxidation phase has no negative influence on the outcome of the advanced integral model's simulation. The onset of the solidification almost coincides, although the formation of the solidified metallic phases is not reproduced identically. The deviation of both solutions regarding the hydrogen mass generated due to the oxidation reaction is further reduced in this test case with a cooling rate of $-30\,K/s$. In summary, the advanced integral model demonstrates a good ability to reflect the thermally-induced phase changes in this test. Its simulation is relatively consistent with the solution of the numerically expensive spatially discretized oxidation model based on a finite volume approach.

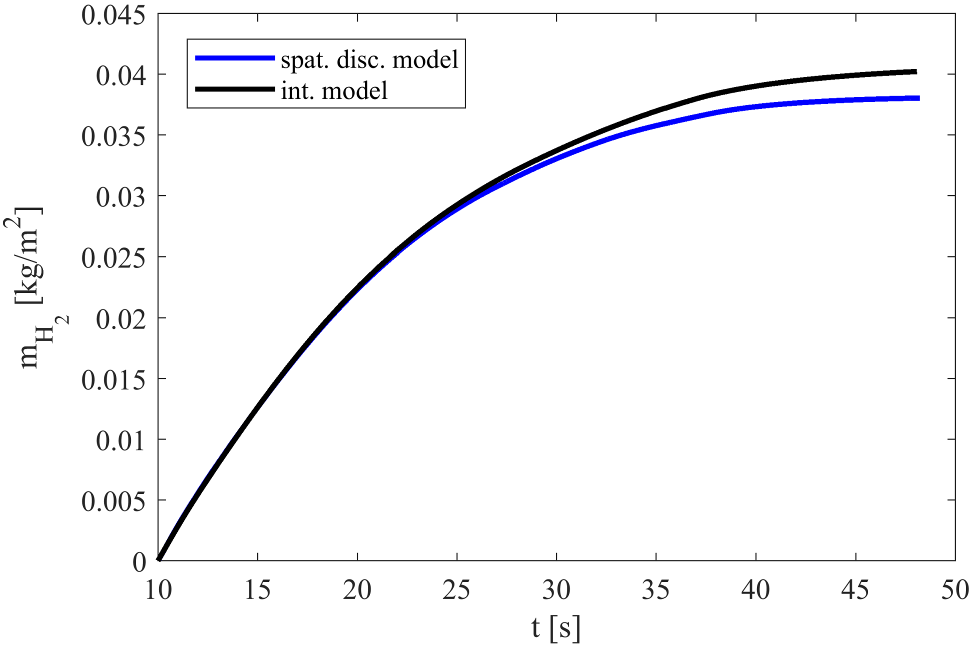

Figure 10.14.: Integral of hydrogen generation for the model case with an imprinted transient of $-30\,K/s$.

10.3. Assessment of results

This work aims at the development of a modern model for the high-temperature oxidation of zirconium in steam for severe accident analysis codes. In particular, the thesis seeks to overcome the limitations of the models used in this context today while still guaranteeing the unchanged, fast execution of these codes. Among the other deficiencies delineated in Chapter 3 and demonstrated in Chapter 9, simple oxidation models based on parabolic rate equations and integral models from literature are incapable of covering thermally-induced phase changes. In this context, this chapter sought to demonstrate the advanced integral model's ability to simulate the thermally-induced phase changes that accompany the high-temperature oxidation of zirconium in steam.

For most of the temporal temperature changes occurring in the base case, particularly the cases of $\pm 5\,K/s$ (99.8 %) and $\pm 10\,K/s$ (99.95 %), the integral model achieves a good qualitative and quantitative reproduction of the solution of the spatially discretized model, whereby it is accompanied by significant savings in terms of computing time. This applies to both the spatial extensions of different phases and to the total oxygen uptake. No negative effects can be found, which result from the neglection of two-phase areas between adjacent single-phase zones and the associated assumption of virtual, sharp phase interfaces. Furthermore, no significant deterioration can be detected that is caused by the treatment of temperature-induced phase transitions with changing phase fractions instead of moving boundaries, either by the modeling of the heat transport with simple heat balances or by the estimation of phase equilibrium concentrations based on bulk temperatures.

For particularly strong and positive temperature changes that are greater than $+10\,K/s$, the oxygen transport between the liquid phase and the solid oxide layer increases with an increase in temperature. This results in intensified deviations of the solutions of both models regarding the thickness of the oxide layer and the generation of hydrogen gas. This is the point at which the advantages of spatially resolved temperature and concentration profiles in the discretized model become apparent. However, due to the rare occurrence of such strong temperature changes in the base case ($< 0.1\,\%$), the influence of this error on the model's predictions is estimated to be low. In the case of solidification problems with cooling rates equal to or greater than $-10\,K/s$, the solutions of both models bear a strong resemblance. When fast transients have to be modeled, the formation of distinct metallic phases (β-Zr and α-Zr) as individual zones might not always be resolved. Due to the limited data that are available to describe the material and transport properties of β-Zr and α-Zr as individual phases, this error is considered to have a minor influence on the simulation results.

In summary, it can be stated that the advanced integral model developed in this work can simulate thermally-induced phase changes. To a large extent, the proposed model can reproduce the solution of a spatially discretized model while requiring significantly less computational resources. Hence, the advanced integral model meets the aims defined in Section 3.4 and, furthermore, shows the potential to improve the modeling of the high-temperature zirconium oxidation in severe accident analysis codes.

11. Summary and outlook

The continuous development of severe accident analysis codes is a central pillar of the research on nuclear safety. These codes allow the evaluation and optimization of present and future reactor designs, as well as the development of new accident management and mitigation measures. However, within these codes, the physical detail of the models for simulation of the high-temperature oxidation of zirconium in steam is increasingly falling behind other physical models, thus contributing significantly to the uncertainty of the codes today. Although there is an urgent need for the further development of advanced oxidation models, corresponding actions have come to a standstill in recent years.

This thesis addressed this issue and presented a method for the advanced modeling of the high-temperature oxidation of zirconium in steam, exploiting physically self-consistent thermodynamic data. At this point, important key features, considerations, and findings of this work are summarized and an outlook for the further development of the applied methods is given.

Summary

Based on an analysis of the state of the art, this thesis summarized the limitations of commonly used oxidation models, identified suitable starting points for their further development, and defined a corresponding development goal. It was found that the underlying assumptions of parabolic rate approaches lead to intrinsic limitations in the related oxidation models, which prevent their further development. Although today's integral models are not subject to those assumptions, they are still incapable of simulating thermally-induced phase changes. Nonetheless, integral models were identified as a reasonable starting point for a coupled heat and mass transport model that describes the high-temperature steam oxidation of zirconium. Furthermore, it was found that such a model could profit from its coupling to a lookup table, which provides physically self-consistent thermodynamic data. An additional review of the existing literature revealed a lack of experimental data suitable for the validation of an advanced integral model. Therefore, the need to develop another model – specifically, a spatially discretized model – has become apparent in order to provide a reference solution for tests of the advanced integral model.

Physical self-consistent thermodynamic data were successfully supplied with the help of the NUCLEA database and the software NucleaToolbox. The resulting lookup table was coupled to a fast-running interpolation algorithm. Based on a comparison to binary Zr-O phase diagrams from the literature, it was shown that the lookup table represents the state of the art. Moreover, the lookup table not only contains information about the concentration- and temperature-dependent formation of different phases, but also offers information on the urgently needed enthalpy differences of contrasting equilibrium states. Hence, for the first time, cumbersome descriptions of the various chemical heat sources and sinks, as found in models from the literature, are rendered obsolete. A disadvantage of this lookup table is its treatment of the substoichiometry of the oxides below 1525 °C, which contradicts experimental observations. Due to this deficit, it was necessary for the time being to define a lower threshold for the applicability of the oxidation model. However, if the thermodynamic databases are revised in the future, the lookup table can easily be recalculated and replaced using the computer scripts developed in the framework of this thesis.

A module was created that provides the oxidation models with temperature-dependent values for different material and transport properties. In this context, it was found that the availability of reliable information on the required material and transport properties is limited (especially for high temperatures) and requires further investigation from materials scientists. Hence, preparations were made that allow an update of this module in accordance with the advancement of the state of the art.

Starting from an isothermal approach, an integral model was extended by energy balances in order to implicitly capture chemical and thermal heat sinks and sources through the exploitation of the thermodynamic lookup table. In this model, chemically induced phase changes are simulated with the help of moving boundary conditions, while thermal phase transitions are included via the adjustment of the zones' phase fractions. The resulting capability to capture both chemically- and thermally-induced phase transitions is the decisive feature, which distinguishes this new advanced integral model from other integral models described in the literature.

The assumptions that had to be made in developing the advanced integral model cannot be further assessed from a theoretical viewpoint, but experimental data suitable for validation purposes is not available. Therefore, an additional spatially discretized model was developed, which requires neither the assumption of concentration and temperature profiles nor a moving boundary condition. As such, the spatially discretized model offers a high-quality reference solution. Its novel consideration of the oxygen transport on the level of distinct phases and its coupling to a thermodynamic lookup table is an innovative feature in the modeling of zirconium oxidation that has not been published before.

Verification of the advanced integral model and the spatially discretized model was conducted based on analytical solutions of Stefan problems. Using the same procedure, further investigations addressed the cell number dependency of the spatially discretized model.

Important findings resulted from the comparison of the models developed in this thesis with the oxidation models published elsewhere in the literature. It was demonstrated that approaches based on parabolic rate equations are incapable of modeling the regression of oxide layers under steam-starved conditions. Therefore, they fail to reproduce strengthened oxidation reactions after temporary phases of steam starvation, which can cause sudden peaks in the generation of hydrogen and heat. Integral models, by contrast, cover those phenomena with the same high precision that spatially discretized models obtain while requiring substantially less computation time. The distinct advantage of the advanced model of this work compared to the integral models from the literature is its high flexibility. This was achieved through its concept of capturing heat contributions from chemical reactions implicitly via its lookup table. Test cases created with the help of simulation results of an exemplary nuclear transient, which was simulated with the computer code ATHLET-CD, demonstrated the advanced integral model's high numerical stability when supplied with boundary conditions that are subject to considerable temporal fluctuation. Thus, it was concluded that this work's novel approach both meets and surpasses the capabilities of existing modeling approaches.

In the final stage of this thesis, the most important feature of the advanced integral model, its ability to model thermally-induced phase changes, was tested. For this purpose, model cases were designed in which external constraints enforced temporal temperature transients. In this regard, it was demonstrated that the integral model can reproduce solutions of the spatially discretized model in qualitative and quantitative agreement. Significant effects of the simplifications made within the framework of the development of the advanced integral model, which may severely affect the simulations, were also ruled out. Therefore, the advanced integral model presented here is the first model of its kind that is capable of including thermally-induced phase changes.

As a result of this work, an advanced integral model is available that simulates the high-temperature oxidation of zirconium in steam as a coupled heat and mass transport problem. For the first time, this model considers chemical and thermal heat sinks and sources implicitly through the exploitation of physically self-consistent thermodynamic data. Furthermore, it can capture both chemically- and thermally-induced phase changes, which is a novelty in the modeling with integral models. Consequently, this advanced approach overcomes the limitations of the commonly applied parabolic rate approaches and supersedes the capabilities of existing integral models. In this way, it achieves the urgently required capability of following the oxidation reaction through different phases of core degradation, starting from the classic oxidation of cladding tube surfaces, through the melting and chemical dissolution processes (oxidization of partially oxidized melts), and ending with the solidification and oxidation of crusts. Therefore, its improved prediction of heat and hydrogen generation is associated with the potential to reduce the uncertainty of today's severe accident analysis codes by providing thermo-hydraulic models with a better, high-quality input.

Outlook

This work stops at the point where the theoretical and numerical development of the advanced integral model is completed. It is obvious that the next development step must be its direct implementation into a severe accident analysis code. The integral approach is known to be compatible with mechanistic computer codes. Since the model presented in this thesis must be coupled to the thermodynamic lookup table using numerically inexpensive interpolation schemes, its computational cost remains largely unaffected. Hence, in terms of a next step, the advanced integral model can be implemented (e.g., into ATHLET-CD) in order to systematically investigate differences in simulation results resulting from the upgrade of the oxidation model. Such an investigation is of the utmost importance because it will finally help to quantify the negative impacts of oxidation models, which are based on parabolic rate equations, and the improvements that a change to an integral model brings.

Promising possibilities for the further improvement of severe accident analysis codes are associated with the continued development of the models developed in this thesis, as well as a generalization of the applied methods. An extension of the advanced integral model for the modeling of temperature transient processes in the ternary U-Zr-O system is conceivable. In this context, the application of an isothermal integral model in combination with a lookup table for the simulation of chemical dissolution processes in the U-Zr-O system has already been demonstrated [33]. From that experience, it is anticipated that the use of a lookup table comprising physically self-consistent thermodynamic data will prove particularly useful in order to describe the complex phase transitions and heat effects of the diverse chemical reactions in this ternary system. At this point, another extension of the model to include iron (Fe) cannot be recommended because the thermodynamic databases of this complex quaternary system are now less developed. It may also be useful to enhance the approach's applicability to systems with larger dimensions ($> 1\,cm$) using enhanced transport models, which are not only based on diffusive but also convective transport mechanisms. Such an integral model covering the U-Zr-O system could significantly improve the modeling of late phase core degradation processes. This is because it would be able to capture fuel-cladding interactions resolved with regard to their concentration- and temperature-dependent melting and solidification points, and to model the oxidation of melts, crusts, and debris under various ambient conditions.

Bibliography

[1] J.P. Abriata, J. Garces, and R. Versaci. The O-Zr (oxygen-zirconium) system. *Bulletin of Alloy Phase Diagrams*, 7(2):116–124, 1986.

[2] Power Reactor Information System (PRIS) - China - Taishan-1. International Atomic Energy Agency (IAEA), Vienna (Austria). Website: https://pris.iaea.org/PRIS/CountryStatistics/ReactorDetails.aspx?current=918; accessed 19. April 2020.

[3] M. Shinya. Estimation of current status inside RPV and PCV at fukushima daiichi NPS, 2017. Tokyo Electric Power Company Holdings, Incorporated (TEPCO), Tokyo (Japan).

[4] D. Jacquemain, G. Cenerino, E. Corenwinder, F.and Raimond, A. Bentaib, H. Bonneville, B. Clement, M. Cranga, F. Fichot, V. Koundy, et al. Nuclear power reactor core melt accidents. current state of knowledge. Technical report, Institut de Radioprotection et de Sûreté Nucléaire (IRSN), Fontenay-aux-Roses (France), 2015.

[5] G. Schanz. Recommendations and supporting information on the choice of zirconium oxidation models in severe accident codes. Technical report, Forschungszentraum Karlsruhe, Karlsruhe (Germany), 2003.

[6] D.R. Olander. Materials chemistry and transport modeling for severe accident analyses in light-water reactors I: external cladding oxidation. *Nuclear Engineering and Design*, 148(2-3):253–271, 1994.

[7] M.S. Veshchunov, A.V. Boldyrev, V.E. Shestak, and K. Mueller. Analysis of molten pool physico-chemical interactions and interpretation of the Phebus FP tests observations. *Nuclear Engineering and Design*, 238(7):1728–1742, 2008.

[8] M. Billone, Y. Yan, T. Burtseva, and R. Daum. Cladding embrittlement during postulated loss-of-coolant accidents. Technical report, Argonne National Lab. (ANL), Argonne, IL (United States), 2008.

[9] P.-Y. Chevalier and E. Fischer. Thermodynamic modelling of the O–U–Zr system. *Journal of nuclear materials*, 257(3):213–255, 1998.

[10] P.-Y. Chevalier, E. Fischer, and B. Cheynet. Progress in the thermodynamic modelling of the O–U–Zr ternary system. *Calphad*, 28(1):15–40, 2004.

[11] A.W. Lemmon Jr. Studies relating to the reaction between zirconium and water at high temperatures. Technical report, Battelle Memorial Inst., Columbus, Ohio (United States), 1957.

[12] F.C. Iglesias, S. Sagat, and H.E. Sills. High temperature oxidation of zircaloy. *Res. Mechanica*, 17(2):125–143, 1986.

[13] W.A. Bostrom. The high temperature oxidation of zircaloy in water. Technical report, Westinghouse Electric Corp. Atomic Power Div., Pittsburgh (United States), 1954.

[14] R.E. Bedworth and N.B. Pilling. The oxidation of metals at high temperatures. *J. Inst. Met.*, 29(3):529–582, 1923.

[15] D.R. Olander. The distribution in space and time of the heat of reaction during oxidation of zircaloy and its effect on corrosion kinetics. Technical report, Lawrence Berkeley National Laboratory (LBNL), Berkelay, CA (United States), 1983.

[16] M. Ševeček, A. Gurgen, A. Seshadri, Y. Che, M. Wagih, B. Phillips, V. Champagne, and K. Shirvan. Development of Cr cold spray–coated fuel cladding with enhanced accident tolerance. *Nuclear Engineering and Technology*, 50(2):229–236, 2018.

[17] H.M. Chung and G.R. Thomas. High-temperature oxidation of zircaloy in hydrogen-steam mixtures. In *Zirconium in the Nuclear Industry*. ASTM International, 1984.

[18] M. Moalem and D.R. Olander. Oxidation of zircaloy by steam. *Journal of Nuclear Materials*, 182:170–194, 1991.

[19] J. Stuckert and M.S. Veshchunov. Behaviour of oxide layer of zirconium-based fuel rod cladding under steam starvation conditions. Technical report, Forschungszentraum Kalrsuhe (FZKA), Karlsruhe (Germany), 2008.

[20] P.J. Hayward and I.M. George. Dissolution of ZrO_2 in molten zircaloy-4. *Journal of nuclear materials*, 265(1-2):69–77, 1999.

[21] E. Hillner, D.G. Franklin, and J.D. Smee. Long-term corrosion of zircaloy before and after irradiation. *Journal of Nuclear Materials*, 278(2):334 – 345, 2000.

[22] V. Bobkov, L. Fokin, E. Petrov, V. Popov, V. Rumiantsev, and A. Savvatimsky. Thermophysical properties of materials for nuclear engineering: a tutorial and collection of data. Technical report, Internaional Atomic Energy Agency (IAEA), Vienna (Austria), 2008.

[23] K.E. Gilchrist. Thermal property measurements on zircaloy-2 and associated oxide layers up to 1200 °C. *Journal of Nuclear Materials*, 62(2-3):257–264, 1976.

[24] A.V. Berdyshev and M.S. Veshchunov. Model for high-temperature oxidation of Zr cladding in steam under fast transient conditions. Technical report, Nuclear Safety Institute of the Russian Academy of Sciences (IBRAE RAS), 2007.

[25] P. Hofmann, J. Stuckert, A. Miassoedov, M.S. Veshchunov, AV Berdyshev, and AV Boldyrev. ZrO_2 dissolution by molten zircaloy and cladding oxide shell failure. new experimental results and modelling. Technical report, Forschungszentrum Karlsruhe (FZKA), Karlsruhe (Germany), 1999.

[26] L. Baker Jr. and L.C. Just. Studies of metal-water reactions at high temperatures. III. Experimental and theoretical studies of the zirconium-water reaction. Technical report, Argonne National Lab. (ANL), Argonne, IL (United States), 1962.

[27] J.T. Prater and E.L. Courtright. Oxidation of zircaloy-4 in steam at 1300 to 2400 °C. In *Zirconium in the Nuclear Industry*. ASTM International, 1987.

[28] V.F. Urbanic and T.R. Heidrick. High-temperature oxidation of zircaloy-2 and zircaloy-4 in steam. *Journal of nuclear materials*, 75(2):251–261, 1978.

[29] R.E. Pawel, J.V. Cathcart, and R.A. McKee. The kinetics of oxidation of zircaloy-4 in steam at high temperatures. *Journal of the Electrochemical Society*, 126(7):1105–1111, 1979.

[30] F.C. Iglesias, B.J. Lewis, C. Desgranges, and C. Toffolon. Clad-coolant chemical interaction. Technical report, Nuclear Energy Agency (NEA), Paris (France), 2015.

[31] M.S. Veshchunov, J. Stuckert, and A.V. Berdyshev. Modelling of Zr-O and U-Zr-O melts oxidation and new crucible tests. Technical report, Forschungszentrum Karlsurhe (FZKA), Karlsruhe (Germany), 2002.

[32] K. Mueller, A.V. Goryachev, V.P. Smirnov, A.M. Svyatkin, J. Stuckert, M.S. Veshchunov, and A.V. Berdyshev. Simultaneous dissolution of UO_2 and ZrO_2 by molten zircaloy. new experiments and modelling. Technical report, Forschungszentrum Karlsruhe (FZKA), Karlsruhe (Germany), 2004.

[33] C. Nigbur, M. Buck, and J. Starflinger. Modelling of the oxidation of mixtures of fuel and zirconium based on the integral diffusion approach. In *Proceedings of the 12th International Topical Meeting on Nuclear Reactor Thermal-Hydraulics, Operations and Safety - NUTHOS-12*. CNS, October 2018.

[34] F.C. Iglesias, D.B. Duncan, S. Sagat, and H.E. Sills. Verification of the FROM model for zircaloy oxidation during high temperature transients. *Journal of Nuclear Materials*, 130:36–44, 1985.

[35] A. Benuzzi and D. Magallon. FARO LWR programme base case test L-11 quick look report. Technical report, Joint Research Centre Ispra (JRC), Ispra (Italy), 1994.

[36] L. Manickam, Q. Guo, A. Komlev, W. Ma, and S. Bechta. Oxidation of molten zirconium droplets in water. *Nuclear Engineering and Design*, 354, 2019.

[37] N. Saunders and A.P. Miodownik. *CALPHAD (Calculation of Phase Diagrams): A Comprehensive Guide*, volume 1 of *Pergamon Materials Series*. Pergamon, 1998.

[38] J.A. Dantzig and M. Rappaz. *Solidification*. Engineering Sciences - Materials. EPFL Press, Lausanne, 1. edition, 2009.

[39] A.T. Dinsdale. SGTE data for pure elements. *Calphad*, 15(4):317 – 425, 1991.

[40] B. Piar. Numerical computation of phase equilibria: NucleaToolbox. Institut de Radioprotection et de Sûreté Nucléaire (IRSN), Fontenay-aux-Roses (France), 2019.

[41] R.P. Elliott. *Constitution of binary alloys, First supplement (1965)*. New York, McGraw-Hill, 1965.

[42] S. Leistikow, G. Schanz, and H. v. Berg. Kinetik und Morphologie der isothermen Dampf-Oxidation von Zircaloy 4 bei 700-1200 °C. Technical report, Kernforschungszentrum Karlsruhe (KfK), Karlsruhe (Germany), 1978.

[43] R.E. Pawel. Oxygen diffusion in the oxide and alpha phases during reaction of zircaloy-4 with steam from 1000 ° to 1500 °C. *Journal of the Electrochemical Society*, 126(7):1111–1118, 1979.

[44] P. Hofmann, H.J. Neitzel, and E.A. Garcia. Chemical interactions of zircaloy-4 tubing with UO_2 fuel and oxygen at temperatures between 900 and $2000°C$ (experiments and PECLOX code). pt. 1-3. Technical report, Kernforschungszentrum Karlsruhe (KfK), Karlsruhe (Germany), 1988.

[45] R.E. Pawel, R.A. Perkins, R.A. McKee, J.V. Cathcart, G.J. Yurek, and R.E. Druschel. Diffusion of oxygen in beta-zircaloy and the high temperature zircaloy-steam reaction. In *Zirconium in the Nuclear Industry*. ASTM International, 1977.

[46] Y.E. Kim, J.W. Park, and J. Cleveland. Thermophysical properties database of materials for light water and heavy water reactors. Technical report, 2006.

[47] L.R. Bunnell and J.T. Prater. Viscosity of zirconium-uranium oxide Zr-UO_2 mixtures at 1800 to 2100 °C. Technical report, Pacific Northwest Lab., Richland, WA (United States), 1986.

[48] P.F. Paradis, T. Ishikawa, and S. Yoda. Non-contact measurements of surface tension and viscosity of niobium, zirconium, and titanium using an electrostatic levitation furnace. *International journal of thermophysics*, 23(3):825–842, 2002.

[49] S. Nazaré, G. Ondracek, and B. Schulz. Properties of light water reactor core melts. *Nuclear Technology*, 32(3):239–246, 1977.

[50] E.N. da C. Andrade. XLI. A theory of the viscosity of liquids. Part I. *The London, Edinburgh, and Dublin Philosophical Magazine and Journal of Science*, 17(112):497–511, 1934.

[51] L.J. Siefken, E.W. Coryell, E.A. Harvego, and J.K. Hohorst. *SCDAP/RELAP5/MOD 3.3 code manual, MATPRO - A library of materials properties for light water reactor accident analysis*. Idaho National Engineering and Environmental Laboratory, Idaho Falls, ID (United States), 2001.

[52] H.P. Wang, S.J. Yang, L. Hu, and B. Wei. Molecular dynamics prediction and experimental evidence for density of normal and metastable liquid zirconium. *Chemical Physics Letters*, 653:112–116, 2016.

[53] T. Kondo, H. Muta, K. Kurosaki, F. Kargl, A. Yamaji, M. Furuya, and Y. Ohishi. Density and viscosity of liquid ZrO_2 measured by aerodynamic levitation technique. *Heliyon*, 5(7), 2019.

[54] C. Homann, W. Hering, and G. Schanz. Analysis and comparison of experimental data of bundle tests QUENCH-07 to QUENCH-09 about B4C control rod behaviour. Technical report, Forschungszentrum Karlsruhe (FZKA), Karlsruhe (Germany), 2006.

[55] A. Trometer. *Investigations on the flooding behaviour of a partially degraded reactor core.* PhD thesis, Institute of Nuclear Technology and Energy Systems, University of Stuttgart, Stuttgart (Germany), 2016.

[56] Deutsche Risikostudie Kernkraftwerke, Phase B. Technical report, Gesellschaft für Reakorsicherheit (GRS), Cologne (Germany), 1990.

A. Oxidation model based on parabolic rate equations

Today's severe accident analysis codes commonly apply oxidation models that are based on parabolic rate equations. The progress achieved by the development of the advanced integral model in this work is therefore evaluated by comparing it to such a model. In this light, this section introduces a straightforward state-of-the-art oxidation model that is based on parabolic rate equations, following the descriptions of Olander in [15].

As described in Section 3.1, parabolic rate equations, which express the increase in the oxygen mass with the help of a rate constant k_τ, can be used to determine the time- and temperature-dependent rate of oxygen uptake.

$$\frac{dm_O}{dt} = \frac{k_\tau}{2\sqrt{t}} \tag{A.1}$$

Knowing the rate of oxygen uptake, it is possible to calculate the heat and hydrogen generation of the chemical reaction based on Eq. 1.1. Such a procedure underlies the assumption of an immediate chemical conversion of the absorbed oxygen into stoichiometric ZrO_2.

Parabolic rate approaches are designed for isothermal conditions, and they are only valid under the assumption that the rate constants remain unchanged. In other words, they build from the assumption that the inhibition of oxygen uptake can be expressed solely by the growth of the oxide layer, which is proportional the square root of time (parabolic kinetics). However, this assumption does not hold under temperature transient conditions since, in this context, the rate constant changes over time ($k_\tau(T)$). Hence, a description of the oxygen uptake solely based on Eq. A.1 is unsuitable for temperature transient conditions and requires further extension.

This challenge can be addressed as follows. In analogy to Eq. A.1, the velocity of the phase interface between oxide and metal $\frac{ds_{ox}}{dt}$ is formulated as a differential equation that is based on the rate constant for the oxide layer thickness k_{ox}.

$$\frac{ds_{ox}}{dt} = \frac{k_{ox}(T)}{2\sqrt{t}} \tag{A.2}$$

Now, its integral provides detailed information about the thickness of the oxide layer $s_{ox}(t)$ at time t. This information again allows the introduction of a new time variable u, which is a virtual time at which the oxide layer thickness, which is now present, would have been achieved with the current (yet changing) parabolic rate constant $k_{ox}(T)$. As a result, the inhibiting effect of the oxide scale can be taken into account. This concept essentially follows Olander [15], but it is executed differently. The time variable u can also be used to model systems that already obtain an oxide scale at the start of a simulation (e.g., due to a pre-oxidization phase) (see Chapter 9).

$$u = \left(\frac{s_{ox}}{k_{ox}}\right)^2 \tag{A.3}$$

Accordingly, both Eq. A.1 and Eq. A.2 are implemented with the time variable u instead of the physical time t and, consequently, require a numerical solution.

$$\frac{dm_O}{dt} = \frac{k_\tau(T)}{2\sqrt{u}} \tag{A.4}$$

$$\frac{ds_{ox}}{dt} = \frac{k_{ox}(T)}{2\sqrt{u}} \tag{A.5}$$

Applying Eq. 1.1, the release of hydrogen and heat can be calculated directly from the rate of the oxygen uptake with the help of Eq. 3.17 and Eq. 3.18. To track temperature changes that have been implicitly assumed so far, the system of differential equations is supplemented by an energy balance, which assumes a homogeneous temperature within the model system.

$$\frac{dT}{dt} = C(Q_R - Q_{env.}), \text{ with } Q_R = \frac{\Delta H_R}{M_{O_2}} \frac{k_\tau(T)}{2\sqrt{u}} \tag{A.6}$$

where the variable Q_R is the heat resulting from the chemical reactions (oxidation of zirconium, dissociation of steam); C is a (constant) factor for the conversion of the heat contributions into a temperature change, which is based on the density ρ, the heat capacity c_p, and the volume of the model system; and $Q_{env.}$ summarizes the heat contributions influencing the model system through its boundary conditions, such as heat transfer processes due to conduction (nuclear fuel), convection (reactor coolant) or radiation (other core structures).

Hence, the full oxidation model that is based on parabolic rate equations, and which is used in this work, builds on Eq. A.3, Eq. A.4, Eq. A.5, and Eq. A.6.

B. Modeling heat effects without thermodynamic computer codes

With oxidation as a multi-step process in mind, Olander [15] developed an elaborate approach to model the heat effects of the high-temperature zirconium oxidation in steam based on parabolic rate laws and their accompanying assumptions. The model builds on the layered structure of the phases in an isothermal oxidation process that proceeds under ideal oxidizing conditions, similar to the illustration in Fig. 3.1. Typically for this approach, Olander [15] assumed only two phases (the metallic zirconium and the oxidic zirconia) and did not distinguish between different allotropes. The key element of his model, in contrast to the model presented in Appendix A, relates to the breaking down of the oxidation into individual partial reactions.

Olander's [15] model is based on a thorough consideration of the chemical partial reactions. At the surface, the oxide layer is in direct contact with steam so that stoichiometric zirconia ZrO_2 is produced. Within the oxide scale, it is assumed that the oxygen concentration decreases linearly towards the phase interface of oxide and metal. Thus, the average stoichiometry of the oxide is $ZrO_{2-1/2x}$, which remains unchanged. At the phase interface, it is assumed that substoichiometric zirconia ZrO_{2-x} is in local thermodynamic equilibrium with oxygen-saturated metallic zirconium ZrO_y. Accordingly, a stoichiometric quantity of (2-x-y) oxygen must be supplied to convert metal into oxide. The base material is pure zirconium (Zr). The stoichiometric parameters x and y can be provided with the aid of temperature-dependent state equations that reflect the slopes of the α-Zr and β-ZrO_2 phase boundaries in a binary Zr-O phase diagram.

Oxygen transfer between the aforementioned phases is described using parabolic rate laws. The oxygen flux entering the system at the gas-oxide interface $\dot{N}_\tau$ is expressed with the help of the rate constant k_τ. The oxygen flux $\dot{N}_{ox}$ that causes the shift of the phase boundary is calculated with the help of the rate constant k_{ox}.[1] The difference in both fluxes $\dot{N}_\tau$ and $\dot{N}_{ox}$ is caused by the diffusion of oxygen from the oxide to the metal, which does not cause an immediate progression of the interface but contributes to the oxygen concentration of the metallic base material. Since there is no corresponding parabolic rate constant for this quantity, $\dot{N}_{met}$ must be calculated from the fluxes $\dot{N}_{\tau}$ and $\dot{N}_{ox}$ and considerations regarding the stoichiometry.

---

[1] k_τ has the dimension mass per square root of time, k_{ox} of a length per square root of time. Therefore, both must be converted first.

$$\dot{N}_{met} = \dot{N}_{\tau} - (2 - \frac{1}{2}x - y)\dot{N}_{ox} \tag{B.1}$$

The difference of $1/2\,x$ is the share that has to remain in the oxide to sustain its average oxygen concentration during growth.

In the next step of his considerations, Olander [15] assigned an enthalpy balance to each step of the chemical conversion. The multiplication of the oxygen fluxes with these enthalpy contributions results in expressions for the heat sources of the partial reactions. At the phase boundary of gas and oxide, the enthalpy of water vapor formation $\Delta H^0_{f,H_2O,g}$ is increased for its dissociation. At the same location, the oxygen enters the solid solution, whereby the enthalpy of the solution of the oxygen in the oxide $\Delta\overline{H}_{ox}$ is released. Since concentration profiles are not tracked, a bulk-averaged value for the enthalpy of the solution is used.

$$\dot{Q}_{g-ox} = \dot{N}_{\tau}\left(\Delta H^0_{f,H_2O,g} - \Delta\overline{H}_{ox}\right) \tag{B.2}$$

At the same phase interface, oxygen diffuses from the oxide to the metal, whereby the enthalpy of the solution of oxygen in the oxide $\Delta\overline{H}_{ox}$ must be increased, and the enthalpy of the solution of oxygen in the metal $\Delta\overline{H}_{met}$ is released.

$$\dot{Q}_{ox-met,I} = \dot{N}_{met}\left(\Delta\overline{H}_{ox} - \Delta\overline{H}_{met}\right) \tag{B.3}$$

At the inner phase boundary, the progressing conversion of metal into oxide also releases some reaction enthalpy ΔH_R. In turn, the enthalpy of the solution of oxygen in the oxide $\Delta\overline{H}_{ox}$ must be increased for the converted part.

$$\dot{Q}_{ox-met,II} = \dot{N}_{ox}\left((2 - x - y)\overline{\Delta H_{ox}} - \Delta H_R\right) \tag{B.4}$$

The corresponding heat of the reaction can be deduced from the following relationship:

$$\Delta H^0_{f,ZrO_2,s} = x\Delta\overline{H}_{ox} + \Delta H_R + y\Delta\overline{H}_{met} \tag{B.5}$$

The required values of the different enthalpies are supplied as constants, which can be found in [15]. In the further course of his work, all partial reactions were summarized in a single energy balance and combined with the assumption of a uniform temperature within the sample. Due to this process, the spatial resolution of the oxidation process vanishes and, despite the considerable detour, one finally returns to the trivial approach.

Olander [15] himself stated that the energy releases calculated using his model deviate from the trivial approach only by 3 % on average, if applied in a temperature range between 1500 K and 1900 K. Against the background of its underlying assumptions and the uncertainties of the required parameters, especially regarding the enthalpies of solution, it is not possible to assess the extent to which the approach is an actual improvement.

Nevertheless, Olander's [15] model has strong significance in the history of models for the high-temperature oxidation of zirconium in steam. This is due to Olander's resourceful considerations regarding the calculation of the spatial evolution of the reaction heat, which can be used as a substitute for precise thermodynamic data. The integral model developed by Veshchunov et al. [7] exploits this feature.

C. Elaborate concentration profiles for integral models

The use of simplified linear profile assumptions in combination with an integral model, as presented in Eq. 3.23, can lead to false results, especially when it is necessary to model the reflective boundary conditions or semi-infinite extensions of a zone. A solution is given by more complex concentration profiles that can be derived from parabolic functions (z = zone):

$$\rho_{O_z}(x) = a_2 x^2 + a_1 x + a_0 \tag{C.1}$$

Using the known boundary conditions, it is possible to derive a parabolic concentration profile. In the case of a semi-infinite medium, the concentrations at the phase interface and the position of the vertex, as well as the gradient at the position of the vertex, are known beforehand.

$$\rho_{O_z}(x = x^*) = \rho_{O_z}^* \tag{C.2}$$

$$\rho_{O_z}(x = x_v) = \rho_{O_{z,0}} \tag{C.3}$$

$$\left.\frac{d\rho_{O_z}}{dx}\right|_{x=x_v} = 0 \tag{C.4}$$

With the help of these points, three equations can be formed that allow the determination of the three unknown factors a_2, a_1, and a_0:

$$a_2 = -\frac{\rho_{O_{z,0}} - \rho_{O_z}^*}{x_v^2 - 2x_v x^* + x^{*2}} \tag{C.5}$$

$$a_1 = \frac{\left(2\rho_{O_{z,0}} - 2\rho_{O_z}^*\right) x_v}{x_v^2 - 2x_v x^* + x^{*2}} \tag{C.6}$$

$$a_0 = \frac{\rho_{O_z}^* x_v^2 - 2\rho_{O_{z,0}} x_v x^* + \rho_{O_{z,0}} x^{*2}}{x_v^2 - 2x_v x^* + x^{*2}} \tag{C.7}$$

Hence, the only remaining unknown is the position of the vertex x_v. The integral of this function $\rho_{O_z}(x)$ must match the total oxygen mass of the zone, so that the following equation can be formulated:

$$\int_{x_v}^{x^*} \rho_O(x)dx = \frac{\left(2\rho_{O_{z,0}} + \rho_{O_z^*}\right)x_v - \left(2\rho_{O_{z,0}} + \rho_{O_z^*}\right)x^*}{3} \overset{!}{=} \overline{\rho}_{O_z}\Delta x_z \tag{C.8}$$

In turn, this equation can be solved to obtain the position of the vertex x_v depending on the position of the zone's outer boundary $x_{z,0}$, where the boundary condition of the finite medium is assumed:

$$x_v = -\frac{\left(2\rho_{O_{z,0}} - 3\overline{\rho}_{O_z} + \rho_{O_z^*}\right)x^* + \left(3\overline{\rho}_{O_z} - 3\rho_{O_{z,0}}\right)x_{z,0}}{\rho_{O_{z,0}} - \rho_{O_z^*}} \tag{C.9}$$

Subsequently, the concentration gradient at the interface can be derived via the derivation of the function $\rho_{O_z}(x)$ at the position of the interface x^*.

$$\left.\frac{d\rho_O}{dx}\right|_{x=x^*} = 2a_2x + a_1 = \frac{2\rho_{O_{z,0}} - 2\rho_{O_z^*}}{x_v - x^*} \tag{C.10}$$

As soon as the position of the vertex x_v reaches the zone's outer boundary $x_{z,0}$, which leads to saturation effects occur, a simulation assuming a semi-infinite medium must be stopped.

If the concentration profile in a finite zone is to be modeled with a parabolic profile, the rising concentration at the boundary $\rho_{O_{z,fin}}$ has to be calculated from that point in time onward, when the position of the vertex x_v reaches the system's outer dimension $x_{z,0}$. In this case, the following three points on the parabola are known:

$$\rho_{O_z}(x = x^*) = \rho_{O_z^*} \tag{C.11}$$

$$\rho_{O_z}(x = x_{z,0}) = \rho_{O_{z,fin}} \tag{C.12}$$

$$\left.\frac{d\rho_{O_z}}{dx}\right|_{x=x_{z,0}} = 0 \tag{C.13}$$

The corresponding factors of the parabolic function a_2, a_1, and a_0 can be calculated as follows:

$$a_2 = -\frac{\rho_{O_{z,fin}} - \rho_{O_z^*}}{x^{*2} - 2x^*x_{z,0} + x_{z,0}^2} \tag{C.14}$$

$$a_1 = \frac{\left(2\rho_{O_{z,fin}} - 2\rho_{O_z^*}\right)x_v}{x^{*2} - 2x^*x_{z,0} + x_{z,0}^2} \tag{C.15}$$

$$a_0 = \frac{\rho_{O z,fin} x^{*2} - 2\rho_{O z,fin} x^* x_{z,0} + \rho_{O z}^* x_v^2}{x^{*2} - 2x^* x_{z,0} + x_{z,0}^2} \tag{C.16}$$

Again, the integral of the parabolic function describing the concentration profile $\rho_O(x)$ must be equal to the zone's oxygen mass:

$$\int\limits_{x_{z,0}}^{x^*} \rho_O(x) dx = \frac{\left(2\rho_{O z,fin} + \rho_{O z}^*\right) x^* - \left(2\rho_{O z,fin} + \rho_{O z}^*\right) x_{z,0}}{3} \overset{!}{=} \overline{\rho}_{O z} \Delta x_z \tag{C.17}$$

In the following step, the oxygen concentration at the boundary $\rho_{O z,fin}$ can be calculated:

$$\rho_{O z,fin} = \frac{3\overline{\rho}_{O z} - \rho_{O z}^*}{2} \tag{C.18}$$

With the information about the oxygen concentration at the boundary $\rho_{z,fin}$ and the derivative of the parabolic function describing the oxygen concentration profile $\rho_O(x)$ at hand, the concentration gradient at the phase interface can be calculated:

$$\left.\frac{d\rho_O}{dx}\right|_{x=x^*} = 2a_2 x + a_1 = -\frac{2\rho_{O z,fin} - 2\rho_{O z}^*}{x^* - x_{z,0}} \tag{C.19}$$

It is also possible to apply this development scheme to other configurations of zones and boundary conditions.

D. Programming flowcharts

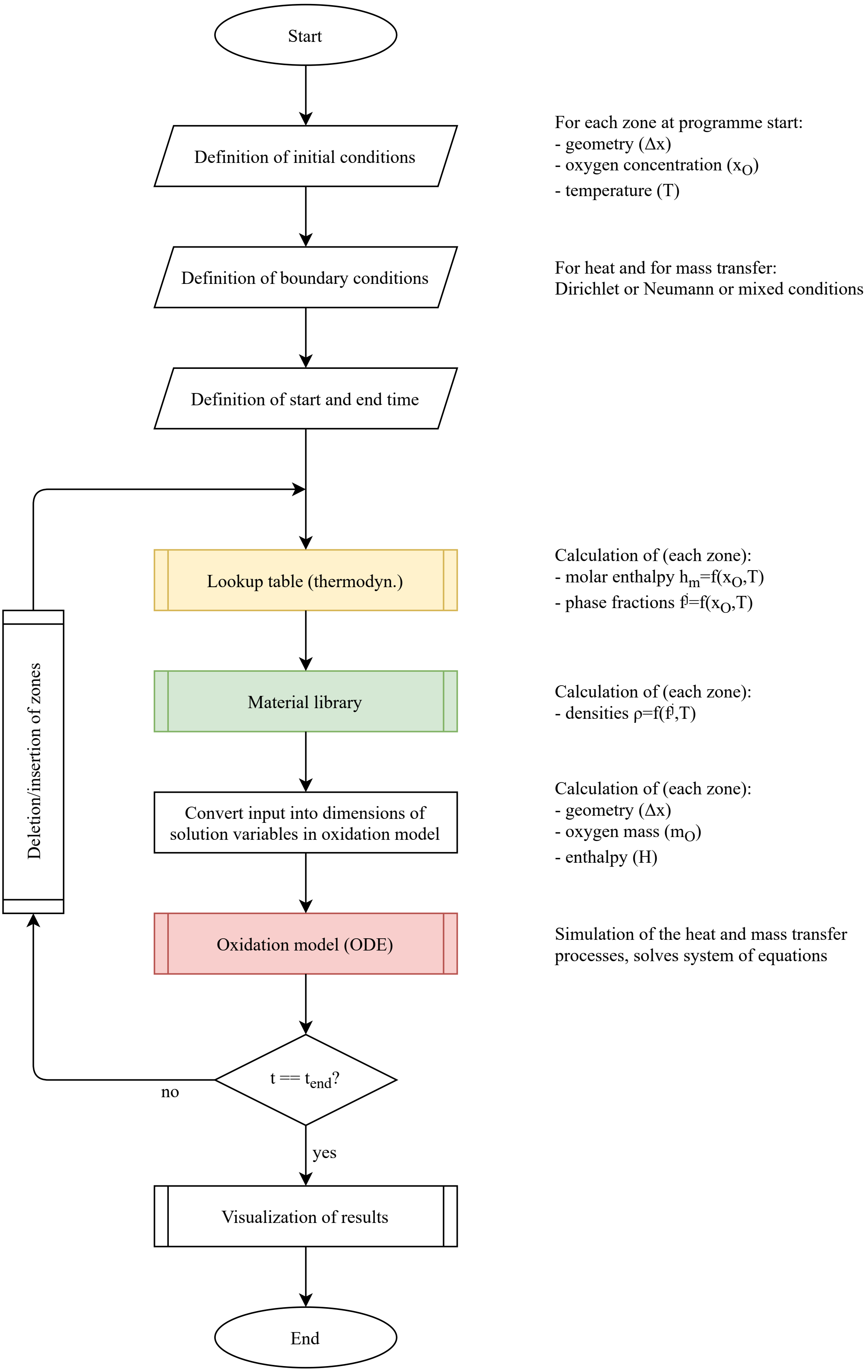
Start
Definition of initial conditions
For each zone at programme start:
- geometry (Δx)
- oxygen concentration (x_O)
- temperature (T)
Definition of boundary conditions
For heat and for mass transfer:
Dirichlet or Neumann or mixed conditions
Definition of start and end time
Lookup table (thermodyn.)
Calculation of (each zone):
- molar enthalpy h_m=f(x_O,T)
- phase fractions f^j=f(x_O,T)
Material library
Calculation of (each zone):
- densities ρ=f(f^j,T)
Convert input into dimensions of solution variables in oxidation model
Calculation of (each zone):
- geometry (Δx)
- oxygen mass (m_O)
- enthalpy (H)
Oxidation model (ODE)
Simulation of the heat and mass transfer processes, solves system of equations
Deletion/insertion of zones
$t == t_{end}$?
no
yes
Visualization of results
End

Figure D.1.: Programming flowchart of the script for the initialization of the advanced integral model.

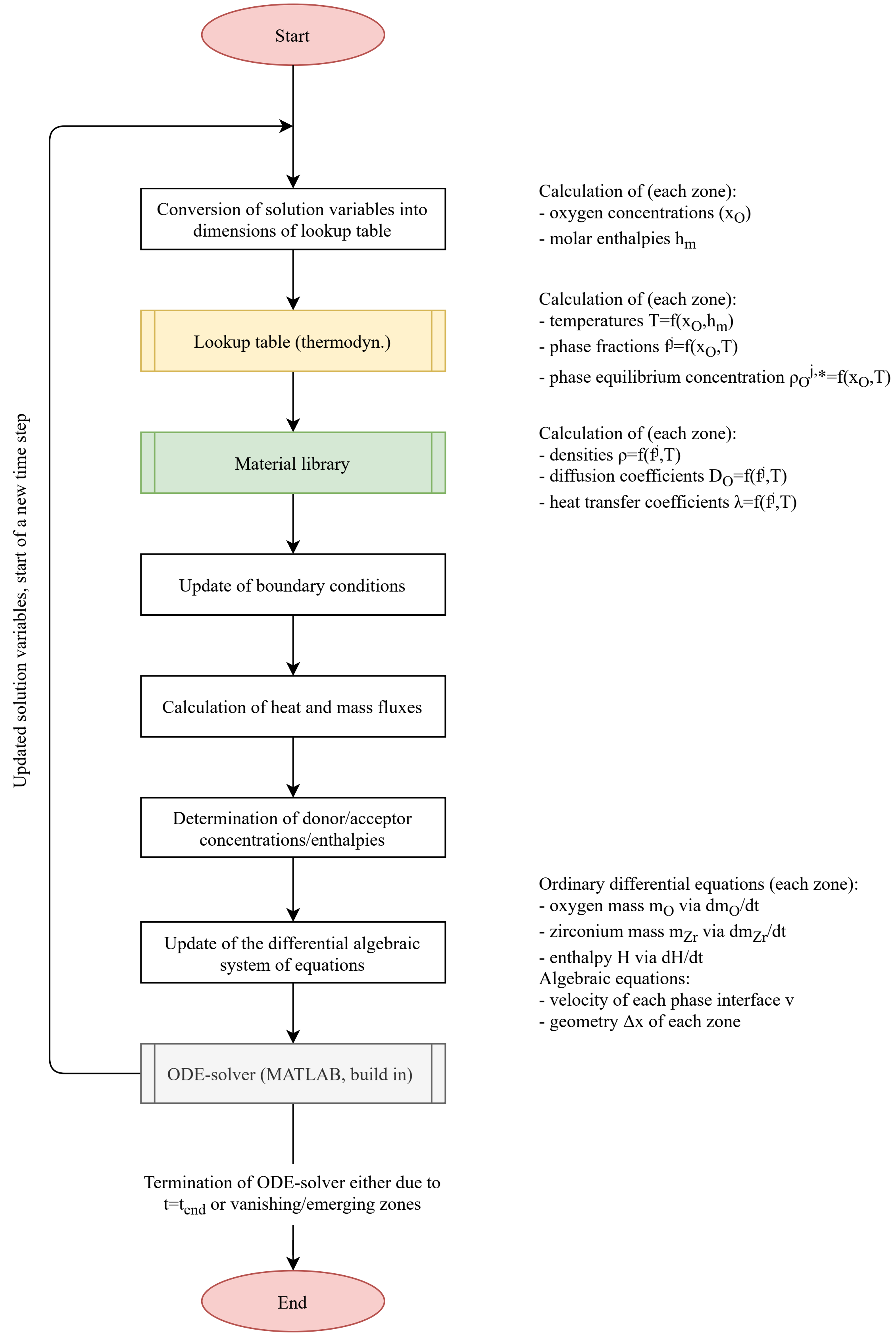
Start
Updated solution variables, start of a new time step
Conversion of solution variables into dimensions of lookup table
Calculation of (each zone):
- oxygen concentrations (x_O)
- molar enthalpies h_m
Lookup table (thermodyn.)
Calculation of (each zone):
- temperatures $T=f(x_O,h_m)$
- phase fractions $f^j=f(x_O,T)$
- phase equilibrium concentration $\rho_O^{j,*}=f(x_O,T)$
Material library
Calculation of (each zone):
- densities $\rho=f(f^j,T)$
- diffusion coefficients $D_O=f(f^j,T)$
- heat transfer coefficients $\lambda=f(f^j,T)$
Update of boundary conditions
Calculation of heat and mass fluxes
Determination of donor/acceptor concentrations/enthalpies
Update of the differential algebraic system of equations
Ordinary differential equations (each zone):
- oxygen mass m_O via dm_O/dt
- zirconium mass m_{Zr} via dm_{Zr}/dt
- enthalpy H via dH/dt
Algebraic equations:
- velocity of each phase interface v
- geometry Δx of each zone
ODE-solver (MATLAB, build in)
Termination of ODE-solver either due to $t=t_{end}$ or vanishing/emerging zones
End

Figure D.2.: Programming flowchart of the oxidation model of the advanced integral model.

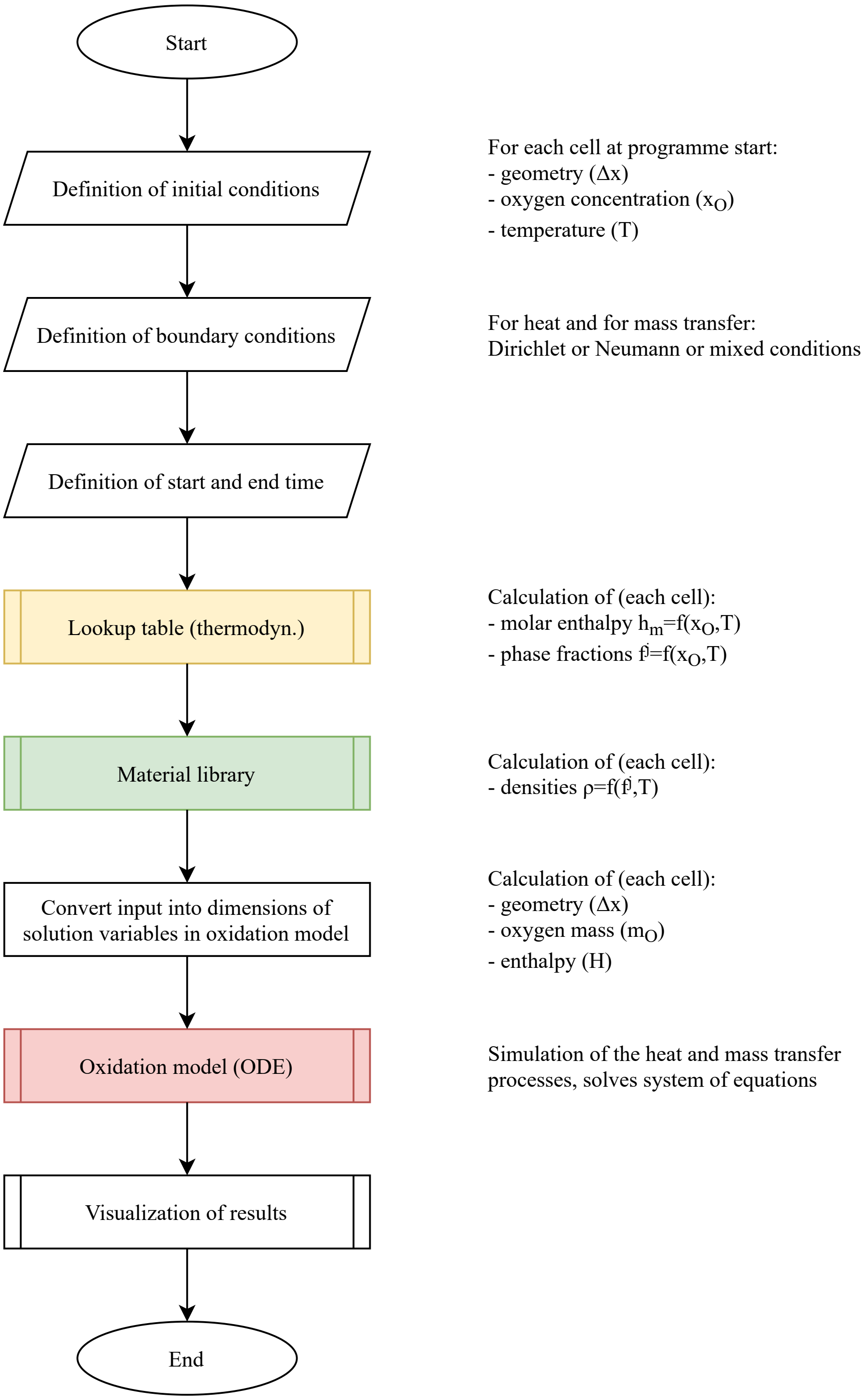
Start
Definition of initial conditions
For each cell at programme start:
- geometry (Δx)
- oxygen concentration (x_O)
- temperature (T)
Definition of boundary conditions
For heat and for mass transfer:
Dirichlet or Neumann or mixed conditions
Definition of start and end time
Lookup table (thermodyn.)
Calculation of (each cell):
- molar enthalpy h_m=f(x_O,T)
- phase fractions f^j=f(x_O,T)
Material library
Calculation of (each cell):
- densities ρ=f(f^j,T)
Convert input into dimensions of solution variables in oxidation model
Calculation of (each cell):
- geometry (Δx)
- oxygen mass (m_O)
- enthalpy (H)
Oxidation model (ODE)
Simulation of the heat and mass transfer processes, solves system of equations
Visualization of results
End

Figure D.3.: Programming flowchart of the script for the initialization of the spatially discretized model.

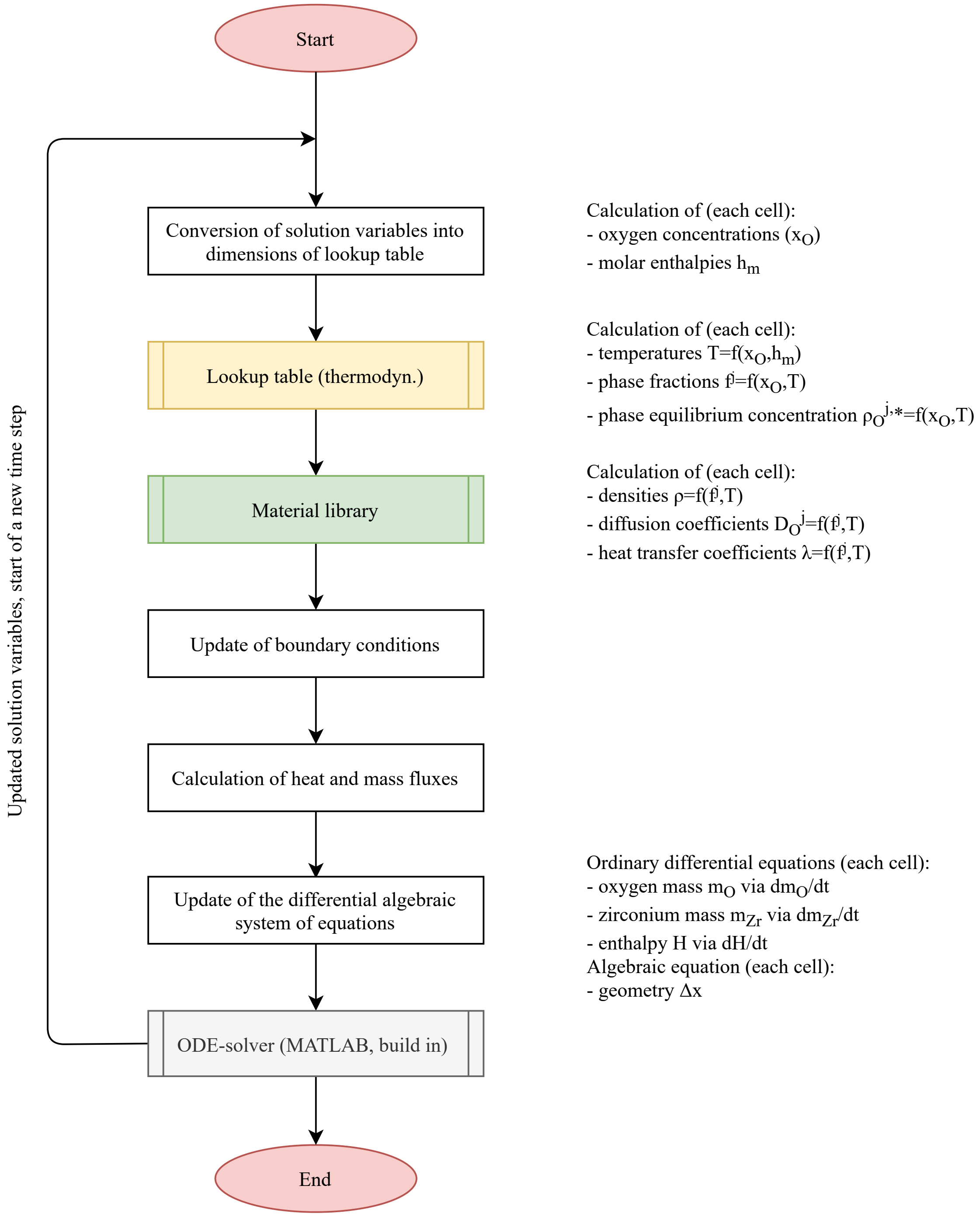
Start
Conversion of solution variables into dimensions of lookup table
Lookup table (thermodyn.)
Material library
Update of boundary conditions
Calculation of heat and mass fluxes
Update of the differential algebraic system of equations
ODE-solver (MATLAB, build in)
End
Updated solution variables, start of a new time step
Calculation of (each cell):
- oxygen concentrations (x_O)
- molar enthalpies h_m
Calculation of (each cell):
- temperatures $T=f(x_O,h_m)$
- phase fractions $f^j=f(x_O,T)$
- phase equilibrium concentration $\rho_O^{j,*}=f(x_O,T)$
Calculation of (each cell):
- densities $\rho=f(f^j,T)$
- diffusion coefficients $D_O^j=f(f^j,T)$
- heat transfer coefficients $\lambda=f(f^j,T)$
Ordinary differential equations (each cell):
- oxygen mass m_O via dm_O/dt
- zirconium mass m_{Zr} via dm_{Zr}/dt
- enthalpy H via dH/dt
Algebraic equation (each cell):
- geometry Δx

Figure D.4.: Programming flowchart of the oxidation model of the spatially discretized model.

E. Supplementary figures

Transient $+10\,K/s$

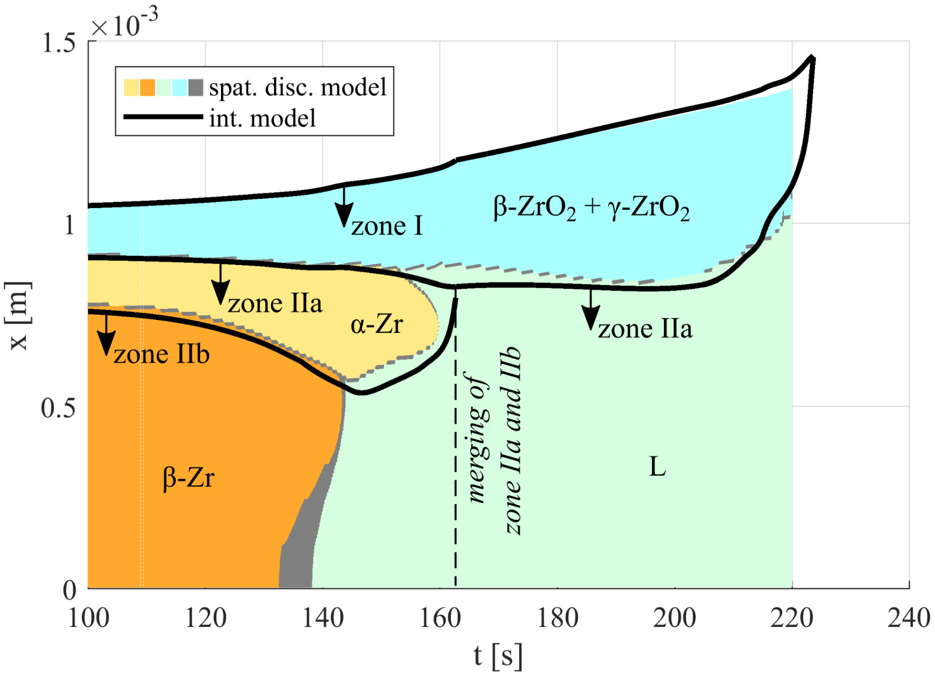

Figure E.1.: Temporal evolution of the expansion of phases with an imprinted transient of $+10\,K/s$.

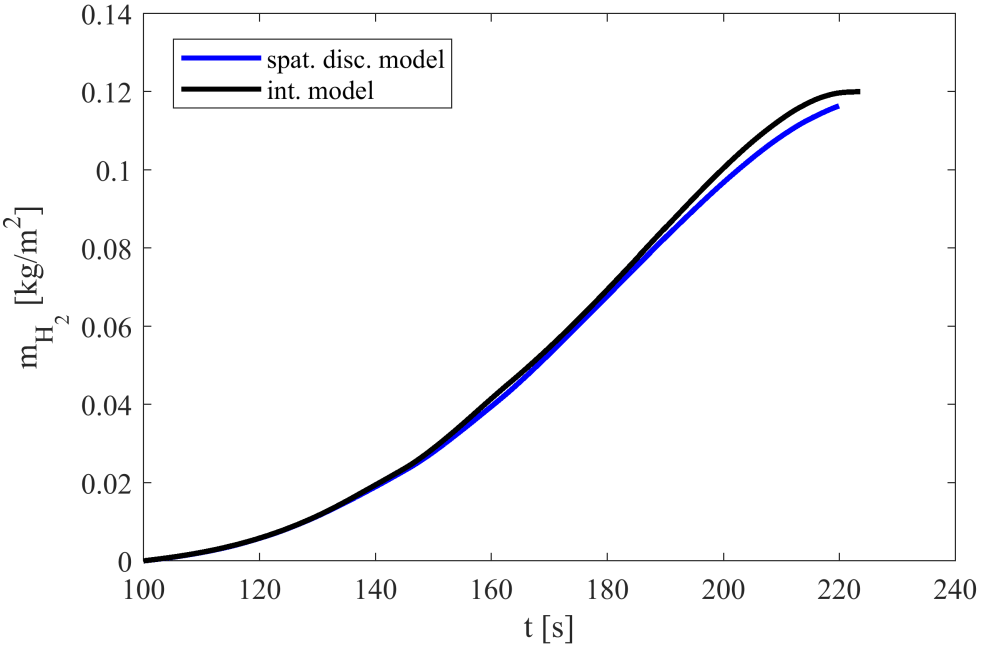

Figure E.2.: Integral of hydrogen generation for the model case with an imprinted transient of $+10\,K/s$.

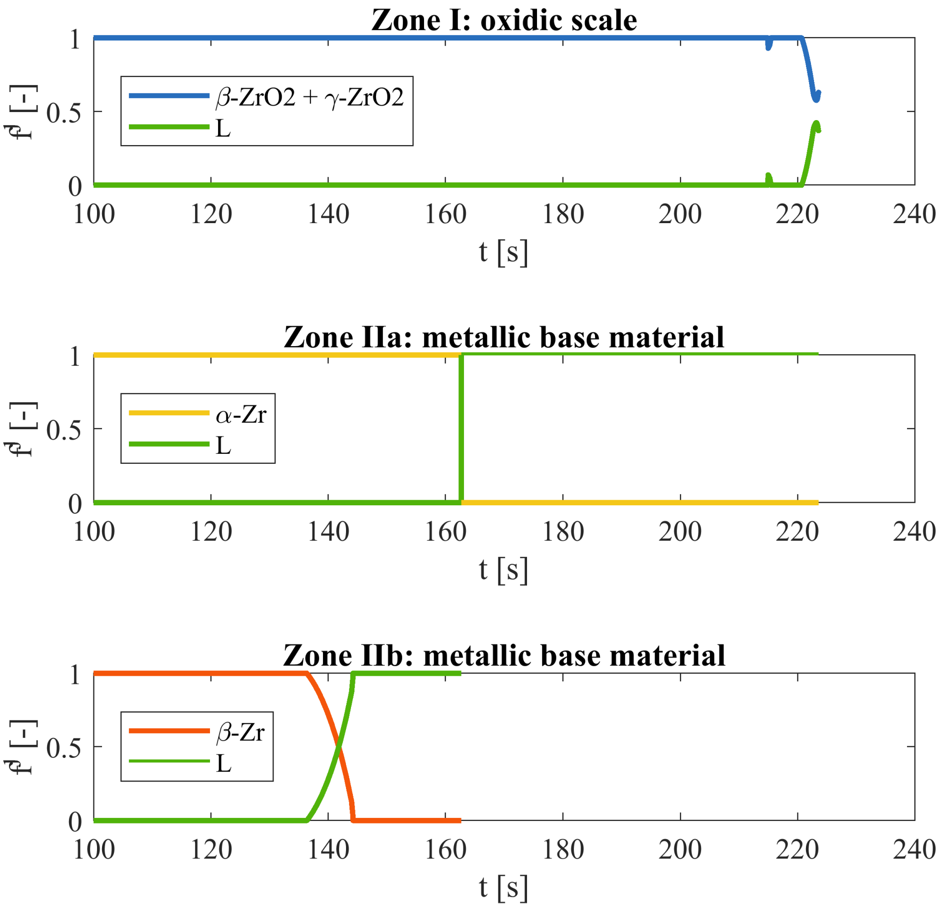

Figure E.3.: Phase fractions of the initially three distinct zones in the integral model. At 163 s zone IIa melts and merges with zone IIb (case: $+10\,K/s$).

Transient $+60\,K/s$

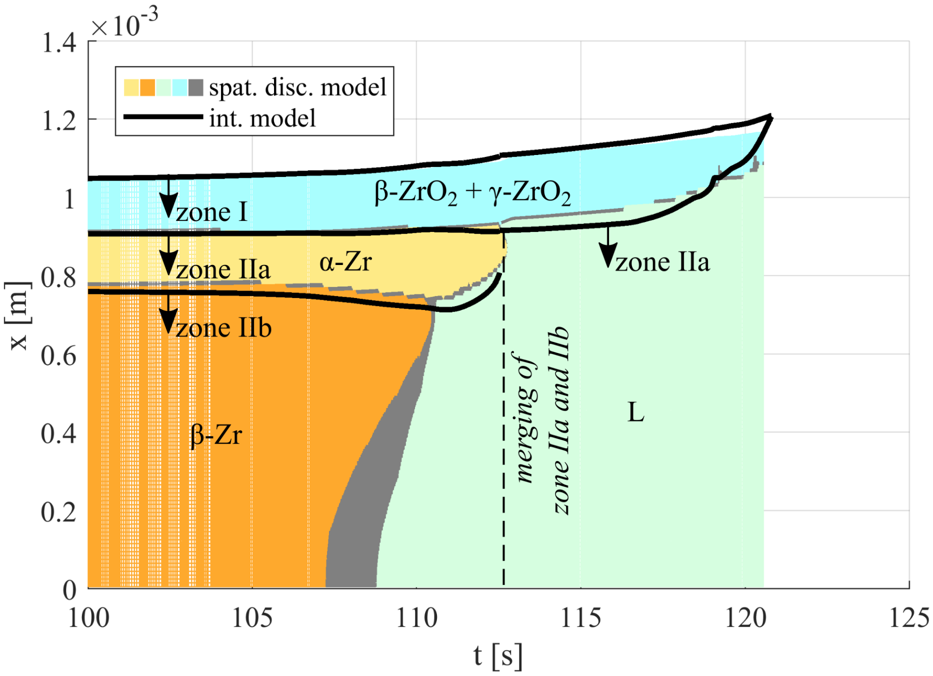

Figure E.4.: Temporal evolution of the expansion of phases with an imprinted transient of $+60\,K/s$.

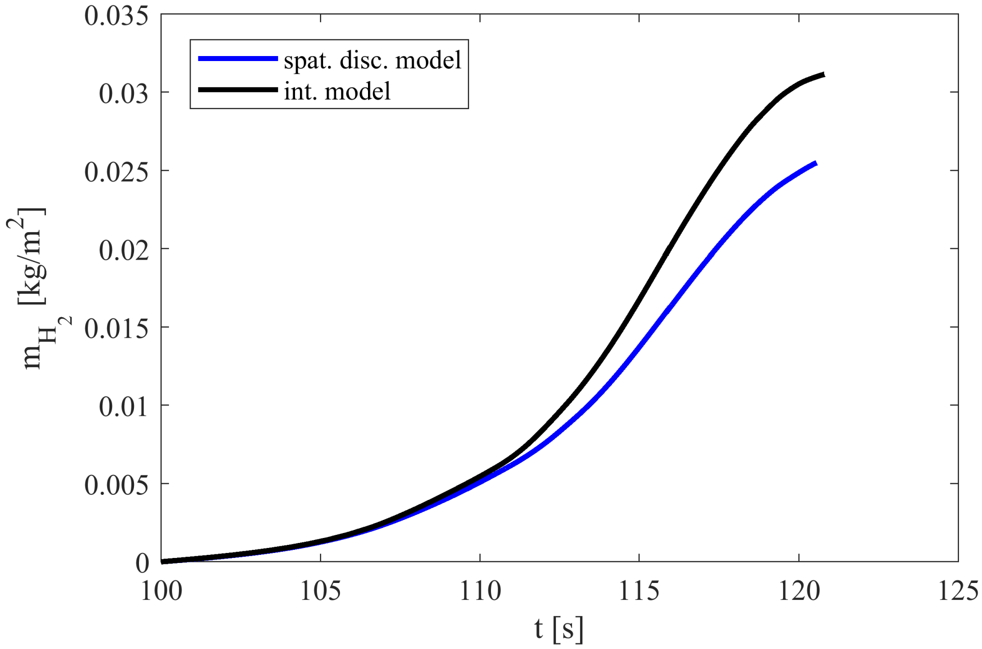

Figure E.5.: Integral of hydrogen generation for the model case with an imprinted transient of $+60\,K/s$.

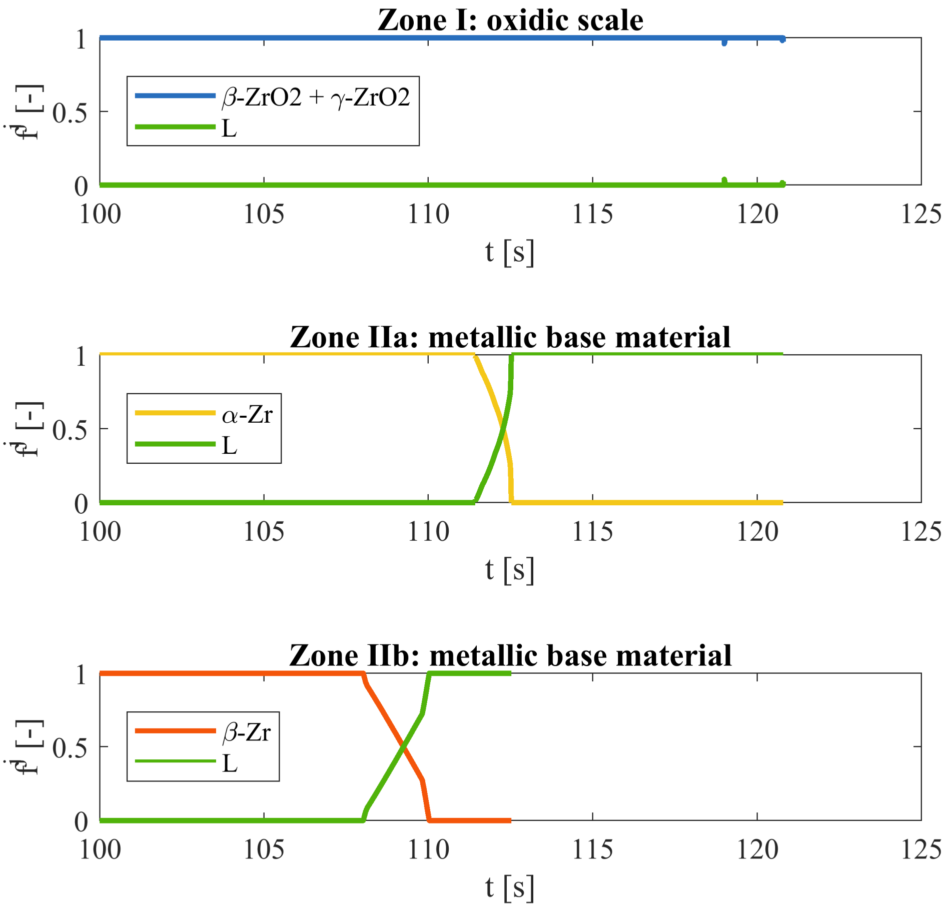

Figure E.6.: Phase fractions of the initially three distinct zones in the integral model. At 112 s zone IIa melts and merges with zone IIb (case: $+60\,K/s$).

Transient $-10\,K/s$

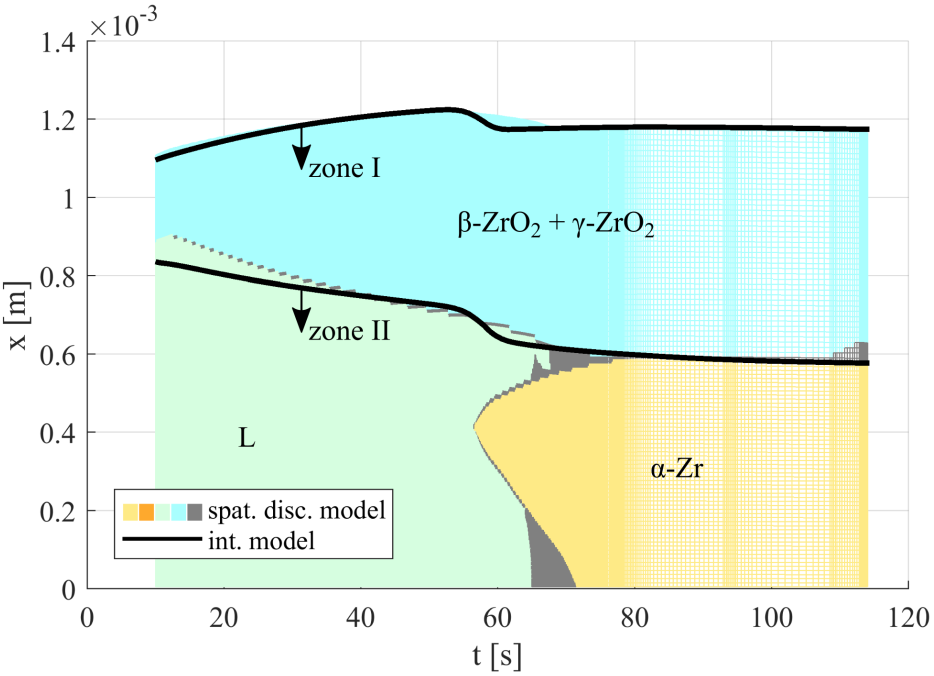

Figure E.7.: Temporal evolution of the expansion of phases with an imprinted transient of $-10\,K/s$.

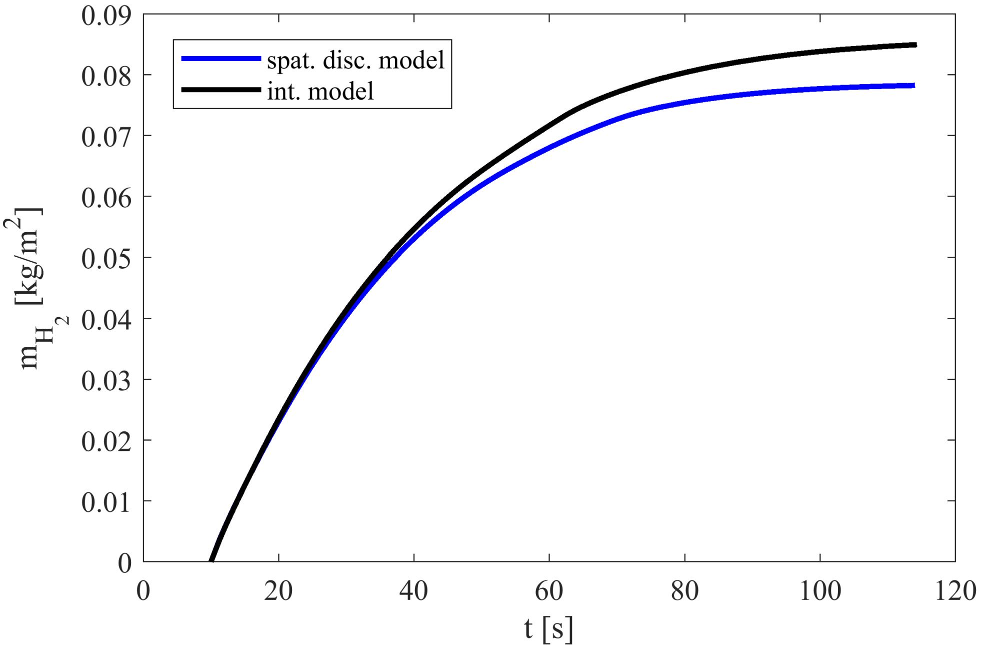

Figure E.8.: Integral of hydrogen generation for the model case with an imprinted transient of $-10\,K/s$.

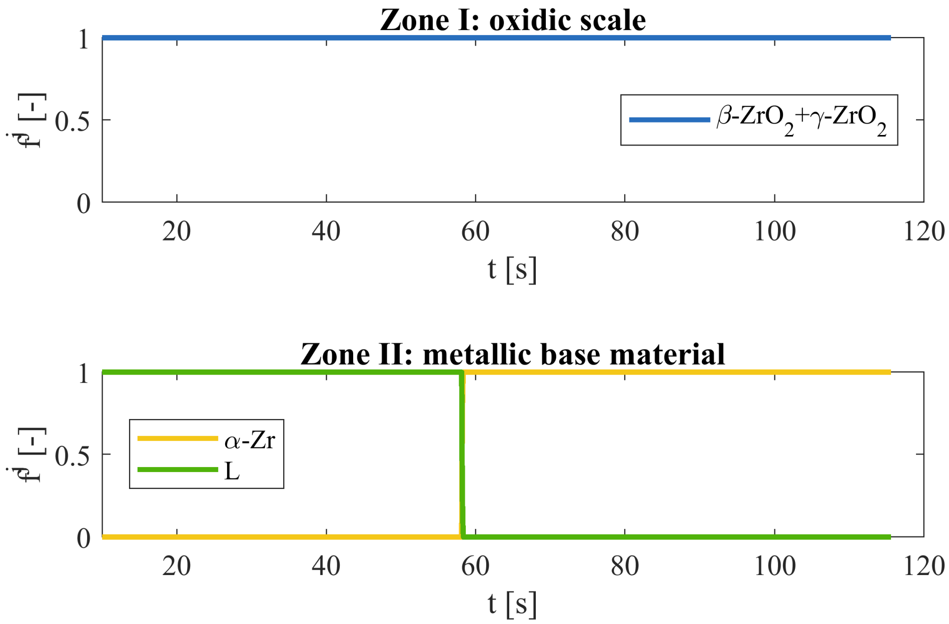

Figure E.9.: Phase fractions of the two distinct zones in the integral model (case: $-10\,K/s$).